DSPACE

https://dspace.org/

Microwave assisted techniques for the synthesis of NiSx and GaN semiconductor nanostructures for applications in sensors

Linganiso, Ella Cebisa

2015-02-04
http://hdl.handle.net/10539/16871

Downloaded from a DSpace repository. https://dspace.org/

Microwave Assisted Techniques for the Synthesis of NiS_x and GaN Semiconductor Nanostructures for Applications in Sensors

By

Ella Cebisa Linganiso (MSc)

A thesis submitted in fulfillment of the requirements for the degree of
Doctor of Philosophy in the Faculty of Science
School of Chemistry
University of the Witwatersrand
Private Bag X03
WITS
2050

Supervisors: **Dr BW Mwakikunga**
Prof. SD Mhlanga
Prof. NJ Coville

Declaration

I declare that “Microwave Assisted Techniques for the Synthesis of NiS_x and GaN Semiconductor Nanostructures for Applications in Sensors” is my own, unaided work submitted for the degree of Doctor of Philosophy at the University of Witwatersrand, Johannesburg. It has not been submitted for any degree or examination in any other University, and all sources I have used or quoted have been indicated and acknowledged by means of complete references.

Name: Ella Cebisa Linganiso (Ms.) Date……..2014

Signature:.....

Abstract

The synthesis of good crystalline nanomaterials by green methods is one of the means to preventing global warming. Application of microwave thermal methods and the use of green solvents to synthesize nanomaterials contribute to this goal. Further, the low cost synthesis of nanomaterials contributes to their ease of availability in the market at affordable costs.

In this study, different NiS_x phases and GaN nanomaterials were obtained by microwave-assisted solution phase synthesis. NiS_2, GaN, α-NiS, (α & β) NiS and Ni_3S_2 phases were obtained by using different reagents and applying different reaction parameters. These materials were characterized by X-ray diffraction, transmission electron microscopy, scanning electron microscopy and photoluminescence, to evaluate their crystalline phases, morphologies, particle size distribution and optical properties respectively.

Hierarchical structures of cubic phase NiS_2 and spherical HDA capped nanostructures were synthesized by a MW-assisted hydrothermal technique. The product phase purity was optimized and the effect of precursor concentration and capping agents were discussed. Further, optical properties of bare and HDA capped NiS_2 materials are reported. Detailed analysis of the PL properties shown by these materials in the UV-vis range has been given by considering their calculated DOE energy band diagrams.

Single phase α-NiS nanostructures with uniformly distributed hierarchical networks were synthesized for the first time in this study. The materials were evaluated for thermal stability under an oxidative environment and at temperatures between 150 ^oC and 600 ^oC. NiS materials showed stability at 300 ^oC and NiO formation was observed from 350 ^oC to 600 ^oC. The annealing effect on the crystalline size and IR absorption of the annealed samples is reported by XRD and FTIR studied. The EPR properties of the annealed materials were studied and compared to the oxidized materials. The transition temperature of the α-NiS was further confirmed by performing

electrical measurements on the as-synthesized material. Further, hydrostatic pressure sensing properties, ethanol and tomato VOCs sensing properties of the α-NiS/PVA composite based devices were carried out and the results are reported. The ethanol gas sensing properties of the devices prepared showed the highest response when compared to hydrostatic pressure sensing and tomato VOCs gas sensing.

UV-blue emitting GaN nanostructures were obtained for the first time by a one-step MW-assisted solvothermal technique. Sensor devices based on the hexagonal wurtzite structures obtained and their PVA composites (GaN/PVA) were prepared with different GaN NPs concentrations. A very high response to hydrostatic pressure was achieved for the devices prepared. The sensitivity of a GaN/PVA composite based device was analyzed for tomato VOCs detection and the results are presented.

Binary phase (α & β) synthesis of NiS materials is commonly reported for the synthesis of Ni:S ratio of 1:1 stoichiometry. This is due to the formation of both phases at temperatures lower than 200 ^{o}C. Here, the effect of NaOH and the S source was investigated as reaction parameters. It was found that the concentration of OH^- ions in solution plays a huge role in the formation of binary phase NiS as well as its morphology distribution in the nanostructures. Hexagonal nanoplatelets, nanorods and nanorod-based flower-like structures were obtained when different reaction parameters were varied in the presence of NaOH. Further, the solubility of different S precursors in the solvent used was studied and found to affect both the morphology and crystalline phase distribution of the products.

Preliminary work on the synthesis of Ni_3S_2 and Se and Te doped Ni_3S_2 is presented in the last chapter. The crystallite sizes of the materials were determined by use of the Scherrer equation and the elemental composition was confirmed by EDS analysis. The relative humidity gas sensing of the samples materials was determined and sensitivity response of the material to humidity was obtained for the first time.

Dedication

This thesis is dedicated to The Beginning…… and…….The End

Acknowledgements

A special gratitude goes to *The Lord God Almighty*, for His unchanging care, love and support as from the beginning of my life till now.

I would like to give my gratitude to my supervisors: Dr Mwakikunga, Prof. Mhlanga and Prof. Coville, for their invaluable advice and supervision throughout the period of this research. I appreciate you for the guidance and the opportunities you created for me to advance this research.

I would like to give special thanks to the Council for Scientific and Industrial Research (CSIR), and National Centre for Nano-Structured Materials (NCNSM) for funding and hosting this research. It would not have been possible to get this far without your facility. I would also like to thank you for giving me allowance to visit laboratories in the Western Cape Ithemba labs SA, Brazil and Germany in the year 2012-2013. The NCNSM Sensors and Devices group members are given special thanks for their invaluable help throughout the research period: Dr G Malgas, Dr D Motaung, Dr G Mhlongo, Mr M Govender, Mr B Thabethe, Mr S Thabethe, Mr A Akande, Mr M Mokwena and Ms V Saasa. I thank all the NCNSM staff members for providing a wonderful working environment and their assistance in carrying out the characterization of my samples. The NCNSM manager; Prof. S Sinha Ray, is acknowledged for being such an inspiration to the researchers at NCNSM and leading by example in the science field. Lastly, I would like to extend a special gratitude to the administrative staff of the NCNSM; Ms M Waard and Ms S Mcineka. You make our lives much easier.

I would also like to extend my gratitude to the Molecular Sciences Institute, School of Chemistry at the University of the Witwatersrand for registering me for this degree.

I would further like to extend my gratitude to the professors who have hosted me in their laboratories during the period of my research. I thank Prof. M Maaza of the Ithemba labs in the Western Cape, for giving me the opportunity to work with their homemade gas sensing system. I thank also Mr B Sone for his help with the experiments as well as facilitating my stay when I was in the Western Cape. I thank Prof. I Hummelgen from the Physics department in the Federal University of Parana, for hosting me in his labs for a period of one month. I had a wonderful experience in his labs with the help of Mr R Rodrigues and Dr M Greenshields. Lastly I thank Prof. S Mathur of the Institute of Inorganic Chemistry in University of Cologne, for allowing me and my colleague Mr M Govender to work in his labs for two months and a half. We had a treasured exposure during our visit to his laboratories. A special gratitude goes also to Dr T Singh and the rest of the group for making our stay comfortable.

A special appreciation goes to my sister and my mentor Dr LZ Linganiso. You are a very important person in my life. May the Lord bless you abundantly.

To all: *May The Lord make His face shine upon you, and be gracious unto you: May He lift up His countenance on you, and give you peace.*

Numbers 6:25-26

List of publications

Current work

- Linganiso, E.C. Mhlanga, S.D., Coville, N.J., Mwakikunga B.W., Synthesis and intra-band photoluminescence of NiS_2 nano-alloys synthesized by microwave-assisted hydrothermal technique, *J. Alloys Cpds.* **552** (2013) 345.
- Linganiso, E.C., Rodrigues, Mhlanga, S.D., Mwakikunga, B.W., Coville, N.J., Hummelgen, I.A., GaN nanostructures-poly(vinyl alcohol) composite based hydrostatic pressure sensor device, *Mater. Chem. Phys*. **143** (2013) 367.
- Linganiso, E.C. Mhlanga, S.D., Coville, N.J., Mwakikunga B.W., Au-controlled enhancement of photoluminescence of NiS nanostructures synthesized via a microwave-assisted hydrothermal technique, *J. Luminescence* **155** (2014) 305.
- Linganiso E.C., Mhlanga, S.D., Coville, N.J., Mwakikunga, B.W., Nkosi, S.S., Motaung, D, EPR studies on α-NiS to NiO transformation by annealing: structural, thermal and optical properties, ***to be submitted***.

Conference proceedings

- Linganiso, E.C., Mwakikunga, B.W., Mhlanga, S.D., Coville, N.J., Sone, B.T., Maaza, M., Synthesis and Hydrogen Gas Sensing Properties of Pure NiS and Au-Coated NiS, IEEE Sensors proceedings, Tapei Taiwan (October 2012).

- Linganiso, E.C., Mwakikunga, B.W., Mhlanga, S.D., Coville, N.J., Singh, T., Fischer, T., Mathur, S., Novel Ni_3S_2 based room temperature humidity sensor and potential breath analyzer, IEEE Sensors proceedings, Valencia, Spain (November 2014) **Accepted**.

Other publications

- Chimowa, G., Linganiso, E.C., Churochkin, D., Coville, N.J., Bhattacharyya, S., Origin of conductivity crossover in entangled multiwalled carbon nanotube networks filled by iron, *Phys. Rev. B* **84** (2011) 205429.
- Linganiso, E.C., Chimowa, G., Franklin, P.J., Bhattacharyya, S., Coville, N.J., The effect of tube filling on the electronic properties of Fe filled carbon nanotubes, *Mater. Chem. Phys.* **132** (2012) 300.
- Thabethe, S., Linganiso, E., Motaung, D., Mashapa, M.G., Nkosi, S., Arendse, C.J., Mwakikunga, B.W., Visible and IR photoluminescence of c-FeSi@a-Si core-shell nano-fibres produces by vapor transport, *J. Luminescence* **143** (2013) 113.

Presentations

- South African Institute of Physics (SAIP) “NiS Nanostructures for Application in Room Temperature Gas Sensors” University of Pretoria, July 2012. Oral presentation.
- Nanotechnology Young Researchers Symposium (NYRS) “Synthesis of NiS Nanostructures for Application in Semiconductor Gas Sensors” University of Witwatersrand, September 2012. Oral presentation. Awarded best oral presentation 1st prize.

- Microscopy Society of Southern Africa (MSSA) “Synthesis of NiS nanostructures using a microwave-assisted hydrothermal technique” University of Cape Town, December 2012. Oral presentation.
- SAIP “Synthesis of NiS nanostructures by microwave-assisted hydrothermal technique: effect of reaction parameters” University of Zululand, July 2013. Oral presentation.
- NanoAfrica “Microwave-Assisted Synthesis of NiS_2 Nanostructures” University of the Free State, November 2011. Poster presentation.
- Emerging Researchers Symposium 2013 Synthesis and Hydrogen Gas Sensing Properties of Bare and Au-Coated NiS October 2013. Poster presentation.
- MSSA “Synthesis and Hydrogen Gas Sensing Properties of Bare and Au-Coated NiS” October 2013. Poster presentation.
- India-Brazil-South Africa (IBSA) workshop “Synthesis of NiS and GaN for gas sensing applications” Kempton Park, March 2013. Oral presentation.
- IBSA workshop “Hydrostatic pressure sensing and tomato volatile detection using GaN/PVP and NiS/PVP composites based devices” Kempton Park. May 2013. Oral presentation.
- NanoAfrica “Synthesis of binary phase (α-, β-) NiS by microwave-assisted hydrothermal technique” Vaal University of Technology, April 2014. Poster presentation.
- SAIP “Synthesis of binary phase (α-, β-) NiS by microwave-assisted hydrothermal technique” University of Johannesburg, July 2014. Poster presentation.

Research visits

- Visiting student at iThemba labs, Western Cape, South Africa, in Prof. M. Maaza's labs. April 2012.
- Visiting student at Federal University of Parana, Curitiba, Brazil in Prof. IA Hummelgen's laboratories. April-May 2013.
- Visiting Student at University of Cologne, Cologne, Germany in Prof. S Mathur's laboratories. September-November 2013.

Contents

Declaration ii

Abstract iii

Dedication v

Acknowledgements vi

List of publications viii

List of Figures xvi

List of Tables xxii

List of Schemes xxii

Abbreviations xxiii

Chapter 1: Introduction 1

1.0 Preamble 1

1.1 Introduction and rationale 1

1.2 Aims and objectives 3

1.3 Thesis outline 4

1.5 References 6

Chapter 2: Literature review 7

2.0 Preamble 7

2.1 Nano-structures and nano-materials 7

2.2 Properties of semiconducting nanomaterials 9

2.3 Applications 10

2.3.1 Energy conversion and storage 10

2.3.2 Electronic applications 11

2.4 Solution phase chemical synthesis of nanomaterials 16

2.4.1 Nucleation and growth of nanoparticles in solution 17

2.4.2 Growth Methods 20

2.5 Gallium Nitride nano-materials 24

2.6 Nickel Sulphide nano-materials 27

2.7 References 34

Chapter 3: MW-assisted synthesis of NiS_2 nanostructures and their PL properties 41

3.0 Preamble 41

3.1 Introduction 41

3.2 Experimental 42

3.2.1 Reagents and sample preparation 42

3.2.2 Characterization 42

3.3 Results and discussion 43

3.3.1 Phase analysis 43

3.3.2 Microscopy analysis 47

3.3.3 Photoluminescence 52

3.4 Conclusions 58

3.5 References 59

Chapter 4: Synthesis of hexagonal gallium nitride and hexagonal nickel sulphide nanostructures and sensing properties of their polymer composite based devices 60

4.0 Preamble 60

4.1 Introduction 60

4.2 Experimental 62

4.2.1 Reagents and sample preparation 62

4.2.2 Device preparation 62

4.3 Results and discussion 63

4.4 Conclusions 75

4.5 References 76

Chapter 5: Effect of NaOH and precursor on the nickel monosulphide phase..... 79

5.0 Preamble 79

5.1 Introduction 79

5.2 Experimental 80

5.2.1 Reagents and sample preparation 80

5.2.2 Characterization 81

5.3 Results and discussion 82

5.3.1 Reaction holding time effect: phase and morphology analysis 82

5.3.2 NaOH concentration effect: phase and morphology analysis 86

5.3.3 Precursor effect: phase and morphology analysis 90

5.3.4 Precursor concentration effect: phase and morphology analysis 94

5.4 Conclusions 97

5.5 References 98

Chapter 6: Structural characterization, optical and magnetic properties of hexagonal NiS: Effect of annealing temperature 100

6.0 Preamble 100

6.1 Introduction 100

6.2 Experimental 101

6.2.1 Reagents and sample preparation 101

6.2.2 Annealing 101

6.2.3 Characterization 102

6.3 Results 102

6.3.1 Phase analysis 102

6.3.2. IR absorption properties 107

6.3.3. Thermal analysis 108

6.3.4 Microscopy analysis 110
6.3.5 Magnetic properties 114
6.3.6 Electronic measurements 118
6.4 Conclusions 119
6.5 References 120
Chapter 7: Preliminary studies on synthesis and relative humidity sensing of Ni_3S_2 layer-based flower-like structures and impurity Se and Te doped Ni_3S_2 122
7.0 Preamble 122
7.1 Introduction 122
7.2 Experimental 123
7.2.1 Reagents and sample preparation 123
7.2.2 Characterization 124
7.3 Results and discussion 124
7.3.1 Phase analysis 124
7.3.2 Microscopy analysis 126
7.3.3 EDS analysis 126
7.3.4 Photoluminescence 130
7.4 Conclusions 134
7.5 Future plans 134
7.6 References 135
Chapter 8: Conclusions and recommendations 136
8.0 Preamble 136
8.1 General conclusion 136
8.2 Future work and recommendations 138

List of Figures

Fig.		Page
2.1	Classification of nanomaterials.	**8**
2.2	A schematic diagram of a typical gas sensing set-up used to measure gas sensing.	**13**
2.3	Gas sensing mechanism of n-type (a) and p-type (b) semiconductor nanomaterials for oxidizing and reducing gases respectively. (c) shows the gas sensing mechanism for metal sulphide n-type semiconductor. Drawing adapted from reference.	**15**
2.4	Top-down (left) and bottom-up (right) - approaches to growth of nanomaterials.	**17**
2.5	Illustration of the overall energy ΔG as a function of the growth particle size *r.*	**18**
2.6	Inverted temperature gradients in microwave versus the conventional oil-bath heating: Difference in temperature profiles after 1 min of microwave irradiation (left) and treatment in an oil-bath (right).	**22**
2.7	Various ternary and quaternary materials used for light emitting diodes with the wavelength ranges between 400 and 900 nm.	**24**
2.8	Independent variation of the band gap and lattice constants for the nitride based quaternaries.	**24**
2.9	A stick-and-ball stacking model of crystals with 2H wurtzitic polytypes. The bonds in an A-plane are indicated with heavier lines to highlight the stacking sequence. The left figure shows a 3-D view while the right figure shows the (0001) plane projection for the wurtzite phase.	**26**

2.10	A schematic phase diagram of $Ni_{1-\delta}S$ in terms of temperature (T), Ni vacancy concentration (δ), and external hydrostatic pressure (P). Image copied from reference.	**28**
3.1	XRD pattern of cubic NiS_2 microstructures synthesized at various microwave power levels.	**44**
3.2	XRD pattern of cubic NiS_2 microstructures synthesized using different precursor concentrations while keeping other parameters constant.	**45**
3.3	XRD profile for the NiS_2 material synthesized in the presence of 5 g HDA which acts as a capping agent.	**46**
3.4	SEM images of the samples synthesized at 600 W (a), 700 W (c), 800 W (e), and their corresponding particle size distribution in (b), (d) and (f) respectively.	**48**
3.5	SEM images of the samples synthesized using Ni(Ac) concentrations 0.08 M, 0.16 M, 0.4 M and their corresponding particle size distribution from top to bottom respectively.	**50**
3.6	SEM (a) and HR-TEM (b) images of NiS_2 nanostructures synthesized at 600 W in the presence of 5 g HDA capping agent. The crystallite size distribution measured from the HR-TEM images is shown in (c).	**51**
3.7	Photoluminescence spectra of the as-synthesized hierarchal and the HDA-capped NiS_2 nanostructures excited at λ = 300 nm.	**54**
3.8	(a) The band energy structure of NiS_2 and (b) the electron states of Ni(3*d*), Ni-S hybridization and S (3*s* and 3*p*) partial density of states.	**55**
3.9	Band structure around the gamma point G of the Brillouin zone of the NiS_2 system. Both the 751 nm and 784 nm feature in the PL spectra are identified on this energy diagram as de-excitations either from Ni (3d) or S(3*s*,3*p*) to Ni-S hybridization energy states whereas the luminescence features from 400-464 nm are attributed to S(3p) to	**57**

	Ni(3d) electron relaxations.	
4.1	XRD patterns of the as-synthesized GaN sample corresponding to hexagonal wurtzite GaN (a) and photoluminescence spectrum of the as-synthesized GaN nanostructures excited at 300 nm (b). Symbol (*) in (a) corresponds to β-Ga2O3 impurity.	**65**
4.2	XRD data corresponding to hexagonal phase NiS (presented in more detail in chapter 5).	**66**
4.3	Change in conductance and capacitance of GaN(2 mg/ml)-PVA(5 mg/ml) based device as a function of applied pressure.	**67**
4.4	Change in conductance and capacitance of GaN(5 mg/ml)-PVA(5 mg/ml) based device as a function of applied pressure.	**68**
4.5	Change in conductance and capacitance of GaN(10 mg/ml)-PVA(5 mg/ml) based device as a function of applied pressure.	**68**
4.6	Sensitivity comparisons between the GaN/PVA composite based devices to different pressures and varying GaN concentrations.	**69**
4.7	Change in conductance of α-NiS/PVA composite based devices as a function of applied pressure and NiS concentration for 5 mg/ml and 10 mg/ml concentrations in 20 mg PVA for left and right respectively. The bottom centred graph shows the difference in the sensitivities of the two samples to pressure.	**70**
4.8	Change in conductance of the α-NiS-PVA composite based device in the presence and absence of ethanol vapor with different concentrations.	**71**
4.9	Change in conductance and capacitance of (300 ^{o}C annealed) α-NiS (5 mg/ml)-PVA(20 mg/ml) based device in the presence of tomato fruit volatiles (a). Change in conductance and capacitance of α-NiS	**74**

	(10 mg/ml)-PVA (20 mg/ml) based device in the presence of tomato fruit volatiles (b). Change in conductance and capacitance of GaN (10 mg/ml)-PVA (5 mg/ml) based device in the presence of tomato fruit volatiles (c).	
5.1	XRD patterns showing NiS samples synthesized at different times. The symbol ($^{\#}$) represent the α-NiS phase and the symbol (*) represents the β-NiS phase.	**83**
5.2	TEM images of NiS samples synthesized at different (a) 15 min, (b) 25 min, (c) 35 min.	**85**
5.3	XRD patterns showing NiS products synthesized at different NaOH concentrations. Symbol (*) represent β-NiS while symbol ($^{\#}$) represents α-NiS phase.	**87**
5.4	SEM (left) and TEM (right) images of NiS synthesized with different NaOH concentrations 3M, 5M and 7M from top to bottom respectively. The two insets on the 7M SEM image (bottom) show hexagonal platelets at the centre of the flowers.	**89**
5.5	Proposed growth mechanism for the binary phase NiS, from particles and rods to flower-like structures.	**90**
5.6	XRD patterns of the samples prepared using the same S source ($Na_2S.9H_2O$) but different solvents (water and NaOH) and samples prepared using different S sources; $Na_2S.9H_2O$, S powder, $CS(NH_2)_2$, while keeping everything else the same. The symbol ($^{\#}$) represent the α-NiS phase and the symbol (*) represents the β-NiS phase.	**91**
5.7	TEM images of the samples prepared using the same precursor and water (a-c) and NaOH (d & e) solvents. The samples prepared using different S sources; $Na_2S.9H_2O$ (d &e), S powder (f-i), $CS(NH_2)_2$ (j & k), while keeping everything else the same. Image (i) shows the	**93**

	power spectrum the image (h).	
5.8	XRD profile showing α-NiS phase samples obtained at varied precursor concentrations. The symbol (*) indicates the $Ni(OH)_2$ peak.	**94**
5.9	Peak width variation of the α-NiS samples as a function of concentration and peak position (left) and the variation of the peak width centered at about 45^o as a function of precursor concentration.	**95**
5.10	TEM images of the products from precursor concentrations 0.03 M, 0.04 M, 0.06 M, 0.07 M and 0.08 M from top to bottom respectively.	**96**
6.1	XRD pattern of NiS annealed at different temperatures (90 to 600 ^oC). Symbols ($^{\#}$) and (*) correspond to the indexed peaks for α-NiS and c-NiO respectively.	**103**
6.2	Crystallite size variation with annealing temperature, estimated by application of the Scherrer equation.	**104**
6.3	Peak shift vs estimated crystallite size as a function of temperature for the 101 peak of NiS (left) and the 200 peak of NiO (right) respectively.	**105**
6.4	XRD pattern showing the peaks in the range; 25^o to 65^o for the α- NiS samples as a function of annealing T.	**106**
6.5	FTIR spectra of the NiS samples annealed at different temperatures (90 to 600 ^oC).	**108**
6.6	DCS plots for the raw and annealed NiS samples (a) from raw to 300 ^oC and (b) from 350 to 600 ^oC (b).	**109**
6.7	TEM images of NiS samples annealed at different temperatures (90 to 600 ^oC) and corresponding to images (a) – (j) respectively.	**111**
6.8	(a) High resolution TEM image of the as-synthesized NiS nanostructures and (b) diameter distribution of the annealed samples.	**112**

	The inset to (a) shows the power spectrum of the rectangle selected area confirming a single crystalline phase.	
6.9	SEM images of the NiS samples annealed at different temperatures (90 to 600 ^{o}C) and corresponding to images (a) – (j) respectively.	**113**
6.10	ESR results of the raw and annealed NiS samples up to 300 ^{o}C (a) and samples annealed at 400 to 600 ^{o}C (b).	**115**
6.11	A plot of number of spins in each sample as a function of annealing temperature.	**117**
6.12	Low temperature electronic measurement of the raw sample powder. The inset is a sigmoidal curve shows the time and temperature relationship, which was used to plot resistance change as a function of temperature.	**118**
7.1	(a) XRD patterns of the samples prepared without doping and with 2.5 % Se and Te doping. (b) Zoomed image of the 110 crystalline orientations showing a shift in peak positions as a function of doping.	**125**
7.2	TEM and SEM images of the flower-like Ni_3S_2 materials. (a & b) pure Ni_3S_2, (b) $Ni_3S_{1.95}Se_{0.05}$, and (c) $Ni_3S_{1.95}Te_{0.05}$.	**126**
7.3	EDS spectra of the prepared samples (a) pure, (b) Se doped and (c) Te doped.	**128**
7.4	EDS mapped images of the Se doped (top) and Te doped samples showing elemental distribution of the elements Ni, S, Se and Te.	**129**
7.5	Shows photoluminescence spectra of the prepared samples excited at λ = 300 nm.	**130**
7.6	(a) RH sensing of the Ni_3S_2-based sensor device and (b) the sensitivity versus RH % plot for the pure, Se doped and Te dopes Ni_3S_2 based sensor devices.	**133**

List of Tables

Table		Page
2.1	Summary of previous work done on solution chemical synthesis of NiS nanostructures.	**30**
3.1	Average crystallite size of the NiS_2 nanostructures synthesized using different precursor concentrations.	**45**
3.2	Average crystallite size of the NiS_2 nanostructures estimated using the Scherrer equation.	**46**
5.1	The different parameters used for each reaction carried out.	**82**
5.2	Peak shift and estimated crystallite size for 131 orientations for β-NiS phase.	**84**
5.3	Variation of the estimated crystallite size of the samples synthesized using different NaOH concentrations.	**87**
6.1	Summary of the shift in the XRD peak positions and crystallite sizes of NiS/NiO samples with annealing temperature.	**105**
6.2	Number of spins calculated using the Trapezium method for each annealing temperature.	**116**
7.1	Crystallite sizes in nm of the prepared samples estimated by the Scherrer equation.	**125**

List of Schemes

Scheme 3.1 Proposed growth mechanisms of bare NiS_2 nano-clusters (a) and HDA capped NiS_2 nano-particles (b) ……. 52

Abbreviations

LDOS: Local density of states

0D: Zero dimensional

1D: One dimensional

2D: Two dimensional

3D: Three dimensional

EG: Ethylene glycol

TAA: Thioacetamide

en: Ethylenediamine

PVP: Polyvinylpyrrolidone

NPs: Nanoparticles

NiS: Nickel sulphide

GaN: Gallium nitride

NiS_2: Nickel disulphide

S: Sulphur

$(Ni(acac)_2)$: Nickel acetylacetone

PEG: Polyethylene glycol

TOPO: Trioctylphosphine oxide

HDA : Hexadecylamine

NiAc: Nickel acetate

XRD: X-ray diffraction

TEM: Transmission electron microscopy

HRTEM: High resolution electron microscopy

SEM: Scanning electron microscopy

EDS: Energy dispersive X-ray spectroscopy

PL: Photoluminescence spectroscopy

ESR: Electron spin resonance spectroscopy

IR: Infrared

NIR: Near infrared

FTIR: Fourier transformed infrared spectroscopy

T: Temperature

MIT: Metal-to-insulator transition

t: Time

MW: microwave

VOCs: Volatile organic compounds

Chapter 1: Introduction

1.0 Preamble

This chapter contains a brief introduction to nanotechnology. It then introduces the motivation for the nanomaterial synthesis method used, semiconductor gas sensors based on nanostructures. The aims and objectives of this study are given followed by the outline of the whole thesis and references to all material cited in the text.

1.1 Introduction and rationale

The worldwide research being carried out in nanotechnology today was in major part inspired from a famous talk that was given by Richard Feynman in 1959, entitled "*There's Plenty of Room at the Bottom*". This talk was focused on the idea of manipulating atoms at the atomic level by the use of small equipment [1]. Nanotechnology, which is the application of nanomaterials in useable devices or forms, has, for more than two decades, received much focus. The focus includes the fabrication of different types of nanostructure architectures, control of both size and characteristic properties of the nanostructures as well as the development of new technologies or methodologies for the fabrication of novel nanomaterials [2, 3]. In the past decade focus has changed to more applicative developments for the nanostructures. Nanostructures are now available in the market, in various forms for various purposes such as; imaging and diagnostics, bio-magnetic separations, MRI contrast agents, sunscreens, power transformers, magnetic recording, transparent conductive coatings, magnetic fluid sealing, chemical and mechanical polishing [1, 4 & 5]. There are many more applications that nanomaterials can be used in, such as; energy storage, energy conversion, drug delivery, catalysis and sensors [6-9]. These are related to some of their amazing properties that are found for these materials such as their good mechanical, thermal, catalytic, electronic and chemical properties.

Although some nanomaterials are found in the market today, there is still a broad range of nanotechnologies that could assist in solving some world problems such as global warming. One of the ways to address global warming is the use of green approaches to carry out chemical reactions in order to minimize the release of unwanted by products. Good and affordable environmental monitoring devices are essential in order to provide safety in the environment and for the humans.

The application of a microwave heating coupled with the use of clean solvents to synthesize nanomaterials is one of the green approaches to nanomaterial synthesis and contributes to the goal of preventing global warming. The convenience of microwave application due to short reaction times and minimum energy used make its application even more favourable when compared to conventional thermal methods of material synthesis.

Fabrication of semiconductor nanomaterial based gas sensors for environmental monitoring is one of the research areas for nanotechnology study and application. The possibility of incorporating nanomaterials in small devices and use in monitoring different environments ranging from low to high risk environments poses an alternative solution to the currently used types of sensors. An advantage is the low cost that is associated in both manufacturing nanomaterials and the device; portable devices will allow high quality monitoring of the environments when compared to the local area installed types of sensors used currently.

The use of nanomaterials in gas sensors dates back to 1962, when Seiyama reported on the way in which the electrical conductivity of zinc oxide (ZnO) could be changed by the presence of reactive gases in the air. This report prompted a huge research effort on the application of metal oxides (MO_x) in gas sensors [10]. The high surface area observed for nanomaterials contributes to their fast response to different types of gases. Different types of inorganic nanomaterials have been fabricated and tested for this application. Most of these materials are groups II-VI and III-V based materials.

GaN is one of the widely researched group (III-V) materials in the area of gas sensing although it has mostly been obtained by use of relatively expensive techniques

which makes it expensive to obtain in high quality. It has been shown to be selective to a number of gases and can be selective to either oxidising or reducing gases especially upon surface modification [11].

NiS (group II-VI) is novel in this kind of application. Its small band gap and the reported catalyst activity are expected to improve the selectivity towards the different analyte gases.

Current challenges in application of nanomaterials in gas sensing technologies include their lack of flexibility, poor response times and stability over limited temperatures [12, 13]. There is therefore a need for much control of the nanostructures and improvement of their properties to account for the remaining parts that limit application of these materials.

1.2 Aims and objectives

This thesis covers work determined by the following aims and objectives:

- To synthesize novel nano-sized NiS_x nanomaterials by microwave assisted hydrothermal technique.
- To synthesize Se and Te doped NiS_x materials.
- To synthesize novel GaN semiconductor nanomaterials by microwave assisted solvorthermal technique.
- To characterize the as-synthesized nanostructures by various techniques. The techniques used include high resolution electron microscopy (HRTEM), scanning electron microscopy (SEM), X-ray diffraction (XRD), photoluminescence spectroscopy (PL) and differential scanning calorimetry (DSC).
- To study gas sensing and pressure sensing properties of the as-synthesized materials.

1.3 Thesis outline

This thesis contains eight chapters.

Chapter 1: Introduction

This chapter contains a brief introduction to nanotechnology. It then introduces the motivation for the nanomaterial synthesis method used, semiconductor gas sensors based on nanostructures. The aims and objectives of this study are given followed by the outline of the whole thesis and references to all material cited in the text.

Chapter 2: Literature review

This chapter contains the background information relating to the thesis topic. This includes general review on the semiconductor nanostructures, review on the materials studied (GaN and NiS_x), general properties and applications of the semiconductor nanostructured materials, review on previous synthesis methods used, review on microwave-assisted growth method and references cited in the text are listed.

Chapter 3: MW-assisted synthesis of NiS_2 nanostructures and their photoluminescence properties

This chapter deals with just one of the many phases of nickel sulphide, NiS_2. Some of the contents of this chapter were published recently and the reference of the paper is given in the preliminary pages. The reported work includes the optimisation and morphological analysis of NiS_2, phase analysis and photoluminescence (PL) properties.

Chapter 4: Synthesis of hexagonal gallium nitride and hexagonal nickel sulphide nanostructures and sensing properties of their polymer composite based devices.

This chapter contains work that was performed at the Federal University of Parana, Brazil. The trip was funded by IBSA trilateral agreement. The microwave synthesis of GaN and NiS nanostructures and their sensing properties are reported.

Chapter 5: Effect of NaOH and precursor on the nickel monosulphide phase.

This chapter reports on the synthesis of binary phase nickel monosulphide. Water and NaOH were applied as solvents for the microwave-assisted hydrothermal synthesis of NiS. Effect of NaOH concentration, precursor concentration and reaction time are reported for different reagents.

Chapter 6: Structural characterization, and the optical and magnetic properties of annealed hexagonal nickel sulphide (NiS): Effect of annealing temperature.

This chapter describes the MW-assisted synthesis of single phase NiS using H_2O solvent. The effect of annealing temperature on the stability of NiS is studied by XRD analysis. PL and ESR properties of the annealed samples are also reported.

Chapter 7: Preliminary studies on synthesis and relative humidity sensing of Ni_3S_2 layer-based flower-like structures and impurity Se and Te doped Ni_3S_2.

This chapter shows the synthesis of another phase of nickel sulphide (Ni_3S_2). The microwave heating method was used to synthesize this material and doping with small amounts of Se and Te metal impurities was performed. The relative humidity gas sensing was studied of the pure phase of the material. The relative humidity measurements were taken in a sensing station based in the University of Cologne, Germany, via the Eur-FP7 collaboration program.

Chapter 8: Conclusions and recommendations.

This chapter contains some concluding remarks in view of the work covered on the thesis. Recommendations for future studies are also made.

1.5 References

[1] Buzea, C., Blandino, I.I.P., Robbie, K., *Biointerphases* **2** (2007)17.

[2] Alemi, A., Hanifehpour, Y., Joo, S.W., Khandar, A., Morsali, A., Min, B.-K., *Physica B* **406** (2011) 2801.

[3] Love, A.J., Makarov, V., Yaminsky, I., Kalinina, N.O., Taliansky, M.E., *Virology* **449** (2014) 133.

[4] Ahmed, M.A., Khafagy, R.M., El-sayed, O., *J. Molecular Structure* **1062** (2014) 133.

[5] Abraham, T., *iRAP, Inc.* (http://www.aibn.uq.edu.au/).

[6] Kaur, G., Singh, T., Kumar, A., *IJEAR* **2** (1012) 50.

[7] Abdin, Z., Alim, M.A., Saidur, R., Islam, M.R., Rashmi, W., Mekhilef, S., Wadi, A., *Renewable and Sustainable Energy Reviews* **26** (2013) 837.

[8] Wang, Z.L., Zhu, G., Yang, Y., Wang, S., Pan, C., materialstoday **15** (2012) 532. Muqbil, I., Masood, A., Sarkar, F.H., Mohammad, R.M., Azmi, A.S., *Cancers* **3** (2011) 428.

[9] Safari, J., Zarnegar, Z., *J. Saudi Chem. Soc.* **18** (2014) 85.

[10] Seiyama, T., Kato, A., Fujiishi, K., Nagatani, M.A., *Anal. Chem.* **34** (1962) 1502.

[11] Schalwig J., Muller, G., Ambacher, O., Stutzmann, M., *Phys. Stat. Sol.* **185** (2001) 39.

[12] Han, W., Redlich, P., Ernst, F., Ruehle, M., *Appl. Phys. Lett.* **122** (2000) 652.

[13] Rahman, M.M., Ahmmad, A.J.S., Jin, J.H., Ahn, S.J., Lee, J.J., Sensors **10** (2010) 4855.

Chapter 2: Literature review

2.0 Preamble

This chapter contains the background information relating to the thesis topic. This includes general review on the semiconductor nanostructures, review on the materials studies (GaN and NiS_x), general properties and applications of the semiconductor nanostructured materials, review on previous synthesis methods used, and review on microwave-assisted chemical synthesis as well as references cited on the text

2.1 Nano-structures and nano-materials

The terms “nanomaterials and nanostructures” are routinely employed in the field of nanoscience and nanotechnology today. These are the type of materials characterized by a size that falls in at least one dimension less than 100 nm [1]. They are distinctive in terms of properties when compared to their bulk counterparts or single atom or molecules [1]. The interest in studying these materials has grown over the past two decades. This growth has been promoted by the different properties nanomaterials exhibit, and their proposed applications, which open up a new world of possibilities. This has great implications for industry as well as in the academic world. This is evidenced by the enormous amount of literature available online on this topic, which increases on a daily basis as researchers world-wide try to obtain favourable conditions for making as well as applying different types of nanomaterials. Nanomaterial based research contributes to many academic fields and has managed to bring together fields such as materials science, physics, chemistry, engineering and medicine biology [1-5]. In these fields, researchers are focused on improving the lives of people via nanoscience and nanotechnology applications. This includes education, the design of new and reliable materials, new composites, and the improvement of systems,

environmental monitoring and conservation [6]. Nanomaterials can be classified according to their size and shape which affect their properties and these vary from zero dimensional (0-D) to three dimensional (3-D) structures [7]. Fig. 2.1 shows the various dimensions that nanostructures materials can have. Zero dimensional nanostructures include nanoparticles, nanoclusters and nanocrystals. These include quantum dot (1-10 nm) that show a quantum confinement effect. Interestingly the confinement of these nanomaterials at certain dimensions, by tuning their sizes renders them usable at different energy levels [8, 9]. This has been demonstrated for nanomaterials such as cadmium selenide (CdSe), zinc oxide (ZnO) and indium phosphide (InP), to name a few. These materials show shifts in their optical band gaps to higher energy as their size is decreased [8, 9]. One dimensional (1-D) nanostructures include nanorods, nanowires and nanotubes. Two dimensional (2-D) nanostructures include thin films and nanoplatelets, while three dimensional nanostructures covers structures such as nanocubes.

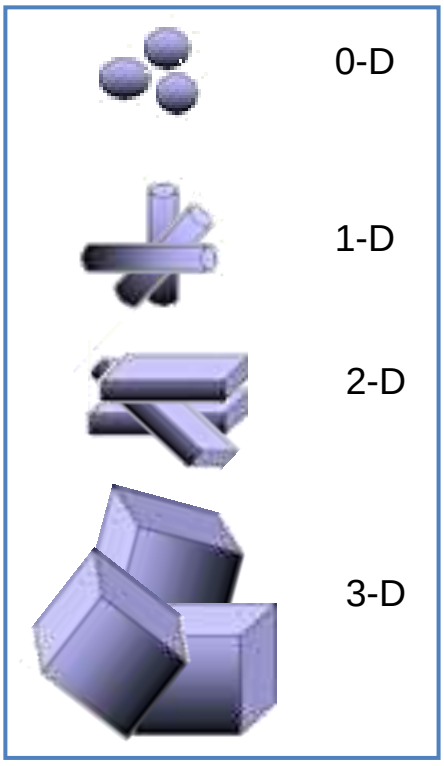


Figure 2.1: Classification of nanomaterials [7].

2.2 Properties of semiconducting nanomaterials

Semiconductors in general can be described as materials with a much higher conductivity than insulators, and when measured at room temperature they have a much lower conductivity than metals [10]. Semiconductors themselves have a distinct characteristic of behaving differently as the temperature is changed, which is not observed with other materials. As such, most semiconductors behave as insulators at room temperature.

Semiconductors can be elementary (an element on its own acts as a semiconductor) e.g. Si, Ge and α-Sn [10]. They can also be compounds (two or more elements covalently bonded to each other) e.g. GaAs, BN, AlN, GaN, AlInGaN, AlGaN, InN, etc. [10, 11]. Semiconductor nanostructures can show interesting properties. When the size decreases below the Bohr exciton radius (natural electron-hole pair separation distance) of the material, the band gap of the material tends to vary [12].

Various mechanisms have been applied to explain the different electronic transport mechanisms that occur in nanostructured materials due to structural defects and dislocations as well as reduced impurities which differentiate their properties from their respective bulk counterparts [13]. Conduction mechanisms such as surface scattering, quantized conduction, Coulomb charging and tunnelling, widening and discreteness of a band gap and a change of microstructure have been reported by Cao [13]. These are promoted by the ability to tune both size and shape of the nanomaterials, such that, different transport mechanisms apply for different nanostructured morphologies [13].

The band gap of a semiconductor is located between the highest occupied energy band, called the valence band (VB), and the lowest occupied energy band, called the conduction band (CB). There is an existence of sub-bands in the band gap of semiconductors, which are associated with surface defects and surface states. These are observed when studying the photoluminescence optical properties of the nanomaterials. The photoemission spectra of nanomaterials have been found to be particle size

dependent, a property which is not observed in bulk materials. Absorption of a photon by nanosized a semiconductor material excites electrons from the valence band into the conduction band, creating an electron-hole pair [14]. The excited electrons instantaneously come back to the VB to recombine with the holes owing to the fact that the electrons are not stable in excited states. During the recombination process, a certain amount of energy is released. The released energy can be dissipated as radiation, which results in a luminescence emission. Due to the presence of a number of possible sub-bands, the excited electrons travel through different paths during the recombination process, which results in different energy emissions. Different types of nanomaterials show different luminescence, and they have been employed in many different ways ranging from fluorescent lamps, X-ray detectors, light emitting diodes, and charge displays [15].

2.3 Applications

Since nanomaterials exhibit unique; chemical, physical, electrical/electronic, magnetic, optical and mechanical properties, they can be used for a wide variety of applications. Some of the applications for nanomaterials are related to energy, electronics, textiles, environment, food, agriculture, health care, etc. Some of these applications are summarized in the discussion below.

2.3.1 Energy conversion and storage

Nanomaterials have been widely studied for energy related applications such as in solar cells, lithium ion batteries, catalysis, and supercapacitors. These applications are related to the different properties nanomaterials offer, such as high surface to volume ratio, a quantum confinement effect, good electron transport properties, to mention a few [16, 17]. Due to the increasing global consumption of energy, insufficient energy generation and storage, there is much need to design materials that can efficiently capture energy from the sun, convert energy from clean sources such as H_2 production from H_2O splitting and store energy using light portable and efficient batteries [18, 19]. A

lot of research has focused on the application of nanomaterials in the fabrication of third generation solar cells [17]. Third generation solar cells are low-cost and highly efficient solar cells that apply novel methods in order to achieve high efficiency. This is how they differ from the Si based high-cost and efficient first generation solar cells, and thin film based low-cost and low-efficient second generation solar cells. The goal is to fabricate solar cells that can efficiently convert solar light to electricity well beyond the single-junction Schokley-Queisser limit of 32% by use of multi-layers of graded series of light absorbers (multi-junctions) [17]. Dye sensitized solar cells are devices fabricated for light-electricity conversion. The mechanism involves light induced electron transfer from the dye molecules to the semiconductor oxide substrate and the injected charge carries are collected at the collector electrode [17]. Conversion efficiencies of above 10% are obtained when using dye-sensitized solar cells [20]. Due to the quantum confinement effect observed for materials with very small particle sizes in the nanometer range, quantum dots have been studied for application in solar cells [17]. They are being used as sensitizers instead of the dye, due to their high surface area-to-volume ratios and outstanding optical properties [21, 22].There is currently a lot of research performed based on application of nanomaterials as a cathode material in lithium ion batteries. The goal is to obtain materials with a good storage capacity [17]. Lithium ions are generally inserted into a host material such that the potential of the host changes [17].

2.3.2 Electronic applications

There are numerous applications for nanomaterials in the field of electronics. Applications include their use in efficient and affordable digital displays, high-density data storage, high power magnets, single electron transistors and highly sensitive sensors [23-26]. Much has been documented in literature on these different applications, but in this report attention has been given to the gas sensing applications of nanomaterials. Typical applications for sensors made out of nanocrystalline materials are the smoke detectors, gas detectors in chemical laboratories and in the mines, automobile engine performance

sensors and for evaluation of toxicity levels of some diseases in infected patients in the medical sector.

A high demand for the fabrication of highly sensitive sensors today for environmental monitoring in chemistry, physics, manufacturing, as well as for medical, food and agriculture areas is increasing [27]. Sensor devices show changes in characteristics due to the change of their environment. The chemical, physical or mechanical change introduced in a sensor environment is used to study the characteristics of the sensor. The area of semiconductor based gas sensors (chemoresistive sensors) is of particular interest. When compared to other types of gas sensing methods used e.g. optical gas sensors and gas chromatography gas sensors [28], semiconductor gas sensors prove to be quite easy to analyse and few logistics are required when preparing the electronic devices. The other gas sensing methods mentioned show a good stability and gas selectivity, which is still a challenge for semiconductor gas sensors. Semiconducting nanomaterials are normally mounted on top of an insulating substrate, with metal contact electrodes also mounted on the insulating material, which allows contact with the sensing material from the sides. Alternatively, nanomaterials can be mounted on top of Au interdigital electrodes which are deposited on an insulating substrate. Pt heaters are also mounted on the backside of a substrate to provide high operating temperature requirements. A sketch showing an example of today's type of gas sensing set-up with the sensing device mounted inside a sensing chamber is shown in Fig. 2.2.

Nanomaterials have a high surface-to-volume ratio and gas sensing using surface reactions has been intensively explored. Advantages such as increased sensitivity, low detection limits, fast response, and the synthesis of light and portable devices have been achieved with these types of sensors. Parameters such as long life time and high carrier mobility are some of the important parameters to look associated with the fabrication of reliable gas sensors [29]. The report by Seiyama in 1962 on how the electrical conductivity of ZnO could be changed due to the presence of reactive gases in the air prompted a huge interest on the application of MO_x in gas sensors [29]. Albeit

these materials have been reported to be sensitive and sometimes even selective, challenges like lack of flexibility, poor response times and stability over limited temperature ranges have been encountered [30, 31]. Most of the currently applied semiconductor gas sensors are operated at temperatures above 150 ^{o}C. These temperatures bring a challenge in terms of energy consumption and may also reduce the life time of the sensor. UV light is sometimes applied to assist the semiconductor surface to actively adsorb or desorb gas molecules [32, 33]. There is currently a need for more reliable materials for use in sensor device fabrication.

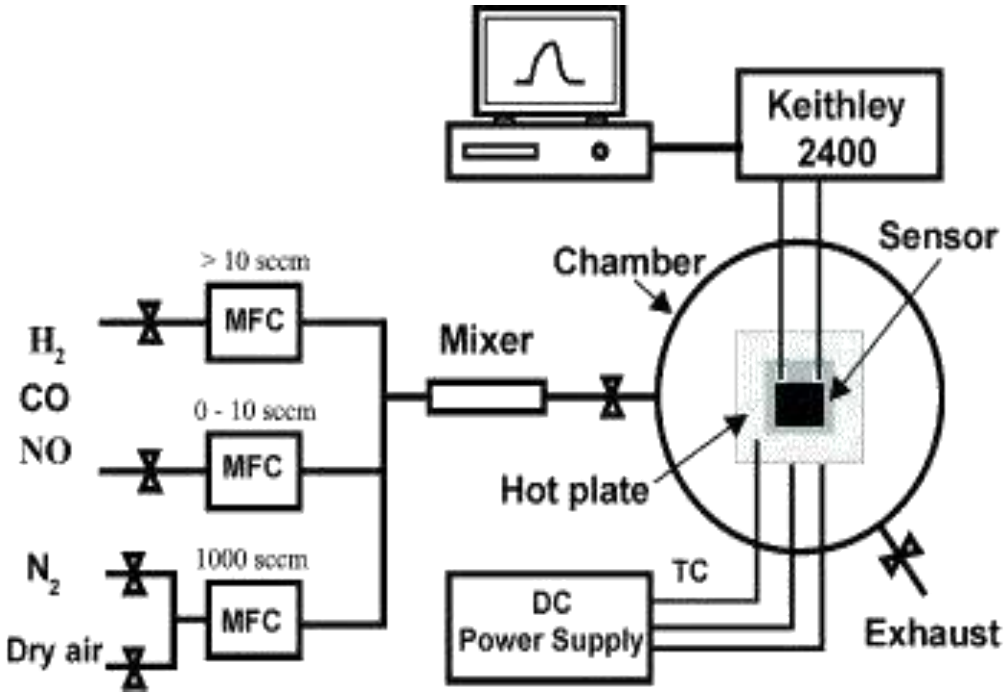


Figure 2.2: A schematic diagram of a typical gas sensing set-up used to measure gas sensing [34].

2.3.2.1 Mechanism of semiconductor based gas sensors

As with any other nanomaterial based application, the microstructure of the material employed in the sensor device plays a huge role in sensor performance. Many sensors show a change in conductance when exposed to different gas environments. Fig. 2.3 (a) shows the widely accepted semiconductor sensing mechanism used to explain the interaction of oxidising and reducing gases for the n-type and the p-type MO_x based semiconductors.

A similar mechanism is also realized for metal nitride semiconductors [35] as well as metal sulphide (MS_x) semiconductors [36] except at elevated temperatures where MS_x materials become oxidised to MO_x material [37]. The mechanism is based on semiconductor-gas interactions at the grain boundaries of the sensor material. An oxidation (or reduction) process takes place on the semiconductor sensor surface during sensing or alternatively gas diffuses on the sensor surface by reaction with surface states associated with pre-adsorbed ambient oxygen. Electron transfer of delocalized conduction band electrons to localized surface starts [35, 38 & 39]. If we consider an n-type semiconductor, where majority carriers are electrons, the MO_x surface will adsorb oxygen species (O_2^-, O^{2-}, O^- [39]) from an air atmosphere by trapping conductive electrons, thus making the MO_x less conductive [35]. Further, for a 1D MO_x nanostructure, the high surface-to-volume ratio provides a large number of surface atoms which have a potential for causing insufficiency in surface atomic coordination and high surface energy. This results in a highly active surface which promotes further adsorption of oxygen from the atmosphere [39]. When the reducing H_2 gas is introduced to this oxygen saturated MO_x (or any semiconducting material), the concentration of adsorbed oxygen species decreases, resulting in increased conductivity of the material. The active H_2 species react with the surface adsorbed oxygen species, generating gaseous H_2O [35]. This way, the pre-trapped electrons are released back to the conduction band, resulting in increased overall conductance of the material. When ambient air is introduced to the material and H_2 gas is switched off, the conductivity of the material recovers its initial condition. ZnS has been used as a gas sensor by Fang et al. [37]. Unlike with metal oxides or nitrides, the gas adsorption/desorption processes are more likely to be irreversible due to the replacement/removal of S^{2-} ions on the NiS surface. When a NiS surface is exposed to H_2 gas, two reactions take place between H_2 and O^{2-} and between H_2 and S^{2-} to form H_2O and H_2S respectively. Sulphur deficient MS_x is obtained after the desorption process. This occurs at elevated temperatures and has been overcome by use of UV illumination which causes enhancement of the modulation of conductance by

adsorbed oxygen [40]. If O_2 was used as the carrier gas, NiS would change to nickel oxide [37].

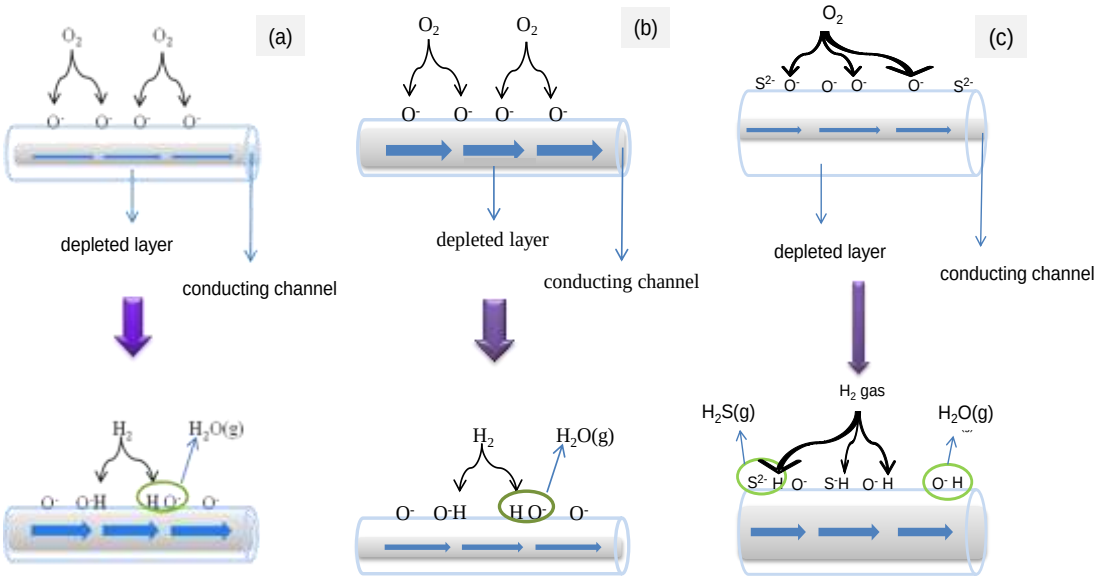


Figure 2.3: Gas sensing mechanism of n-type (a) and p-type (b) semiconductor nanomaterials for oxidising and reducing gases respectively. (c) shows the gas sensing mechanism for metal sulphide n-type semiconductor. Drawing adapted from reference [35].

For a p-type semiconductor, where majority carriers are holes, an opposite behaviour is observed. Under an oxygen ambient atmosphere, the oxygen gets adsorbed on the surface of the material, trapping electrons that are excited from the valence band [41]. This results in an increase in the number of holes which subsequently increases the conductance of the material. When a reducing gas such as H_2 is introduced to the sensor environment, electrons are injected into the valence band where they recombine with the holes and results in a reduced number of holes and less conductance. The sensing mechanism for a p-type semiconductor is shown in Fig. 2.3 (b). The sensitivity response is determined by recording the resistance before the gas is introduced (R_0) and the maximum resistance of an analyte gas (R_g). The sensitivity is then defined as $S = R_{max}/R_{min}$, where R_{max}/R_{min} is calculated as R_0/R_g for reducing gases and R_g/R_0 for oxidising gases when using n-type semiconductor and the reverse is applicable for p-type semiconductors [42]. Equations 1-4 show the changing states of oxygen species adsorbed on the

surface of MO_x semiconductor as the temperature is increased [43, 44]. Equation 5 shows the hydrogen reducing mechanism that can take place on an oxygenated semiconductor sensor surface at room temperature [45].

$$O_{2(gas)} \leftrightarrow O_{2(ads)} \quad (1)$$

$$O_{2(ads)} + e^- \leftrightarrow O^-_{2(ads)} \quad (2)$$

$$O^-_{2(ads)} + e^- \leftrightarrow 2O^-_{(ads)} \quad (3)$$

$$O^-_{(ads)} + e^- \leftrightarrow O^{2-}_{(ads)} \quad (4)$$

$$2H_2 + O^-_{2(ads)} \rightarrow 2H_2O + e^- \quad (5)$$

Important parameters to be achieved for gas sensors include a high sensitivity, good selectivity, fast response time, fast recovery time, reproducibility, stability, low cost and good maintenance [46]. These are important for the commercial application of nanostructure based gas sensors. One of the challenges faced with wide band gap semiconductors is their poor selectivity towards different gases [38]. Research attention is now directed on trying to improve the selectivity of the sensors and to achieve room temperature operation of the sensors in order to minimize running costs and to commercialise them for the analysis of individual analytes. The work currently done by various research groups has focused on the improvement of the nanocrystalline structures, doping nanomaterials with impurities, applying selective catalysts on the surface of the semiconductors, and fabricating different heterostructures (including use of p-n junctions for light assisted gas sensors) which influence carrier charge transport [22, 33, 47 &48].

2.4 Solution phase chemical synthesis of nanomaterials

Nanomaterials can be fabricated via two general approaches viz, a top-down approach and a bottom up approach. The top-down approach involves breaking down a bulk material until the desired nanomaterials are obtained [Fig. 2.4]. This method is not widely used to fabricate nanomaterials due to the

number of imperfections it introduces to a material surface [12]. The bottom-up approach involves growing of nanomaterials from single atoms or molecules until cluster of nanomaterials form [Fig. 2.4]. This is the popular technique used in the fabrication of nanomaterials. This method generates less defects and better homogeneity of a fabricated nanostructure is achieved, when compared to the top-down approach. Solution phase chemical synthesis is one of the methods that are used in the bottom-up approach.

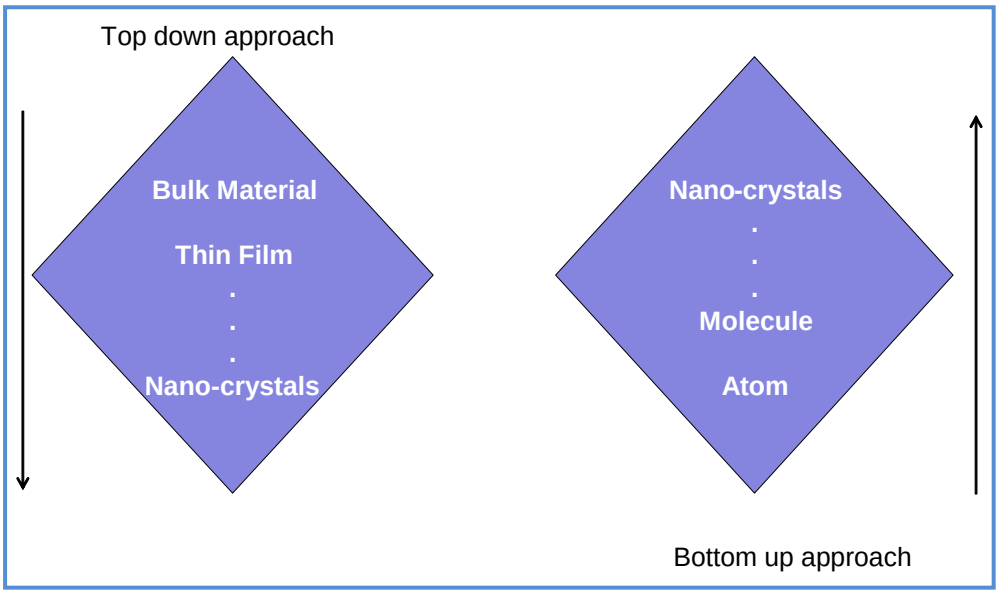


Figure 2.4: Top-down (left) and bottom-up (right) - approaches to growth of nanomaterials.

2.4.1 Nucleation and growth of nanoparticles in solution

Nanomaterials are readily obtained from a solution by precipitation. The nanostructure forms by nucleation which occurs as a result of supersaturation after the solute concentration has exceeded the equilibrium solubility of the solution [12]. Due to a high Gibbs free energy of the solution, as a result of supersaturation, the overall energy of the system decreases in order to preserve an equilibrium concentration in the solution [12, 49]. This is a thermodynamically driven nucleation process which is referred to as

homogenous nucleation. The solute molecules combine to produce nuclei without a solid interface [49]. The overall free energy, ΔG (Equation 6) of the reaction, is the sum of the free energy due to the formation of a new volume and the free energy due to the new surface created [49].

$$\Delta G = -\frac{4}{V}\pi r^3 k_B T \ln(S) + 4\pi r^2 \gamma \qquad (6)$$

For spherical particles of the reaction where *V* is the molecular volume of the precipitated species, *r* is the radius of the nuclei, k_B is the Boltzmann constant, *S* is the saturation ratio, and γ is the surface free energy per unit surface area. When *S* >1, ΔG has a positive maximum value at a critical size, *r**, as shown in Fig. 2.5.

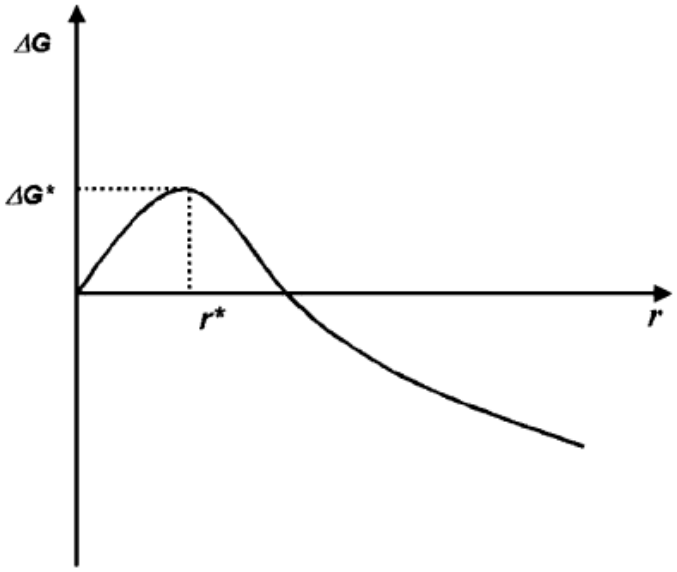


Figure 2.5: Illustration of the overall energy Δ*G* as a function of the growth particle size *r* [50].

When the nuclei size is bigger than the critical size, the growth free energy is decreased and the stable nuclei grow to form particles. When *r* = *r**, *d*Δ*G*/*dr* = 0 and the critical size r* is given in equation 7.

$$r* = \frac{2V\gamma}{3k_B T ln(S)} \qquad (7)$$

For a given value of *S*, all particles with $r > r^*$ will grow and all particles with $r < r^*$ will dissolve [49]. This is because the critical size r^* is the minimum particle size that can be achieved to begin nucleation. From the equation, it is clear that the critical nuclei size r* is inversely proportional to the saturation ratio *S*. After the formation of nuclei from the solution, a growth through molecular addition occurs, and this relives the supersaturated step. When the concentration drops below the critical level, nucleation stops and the particle growth continues by molecular addition until the equilibrium concentration of the precipitated species is reached [49].

Uniformity of the size distribution is achieved through a short nucleation period that generates the particles obtained at the end of the reaction followed by a self-sharpening growth process. At this stage, the smaller particles grow more rapidly than the larger ones because the free energy driving force is larger for smaller particles than for larger ones. At this stage, focusing in size occurs [49]. The nearly monodispersed size distribution can be obtained by either stopping the reaction (nucleation and growth) quickly or by supplying a reactant source to keep a saturated condition during the course of the reaction.

Alternatively, when the reactants are depleted due to particle growth, an Ostwald ripening, defocusing will occur, where the larger particles continue to grow, and the smaller ones get smaller and finally dissolve [50]. Because the saturation ratio (*S*) decreases and the corresponding critical nuclei size (r*) increases (according to equation 2) any particles smaller than this new critical size will dissolve [50]. If the reaction is quickly stopped at this stage, the particles will have a broad size distribution, which is shown by a distribution centering two size regimes, a bigger one and a smaller one. Their critical size at this saturation is in between the two values. In the latter case, the size of the particles become relatively large and their size can extend into the micrometer regime. During an actual experiment, when there is no continuous supply of reactants, the saturation ratio continues to decrease and the critical nuclei size continues to increase. To get a short burst of nucleation, a high saturation ratio (*S*) is required.

In addition to the growth by molecular addition, where soluble species deposit on the solid surface, particles can grow by aggregation with other particles, and this is called secondary growth. The rate of particle growth by aggregation is much larger than the growth by molecular addition. After the particles grow to a stable size, they will grow by combining with smaller unstable nuclei and not by collisions with other stable particles. Because nanopartices are small, and are not thermodynamically stable, a method is required to allow nanoparticles to settle during the reaction. This can be achieved either by adding surfactant protecting agents, such as organic ligands or inorganic capping materials [51, 52], or by placing them in an inert environment such as an inorganic matrix or polymer [49]. The stability of nanocrystal dispersion will then be promoted by a favourable interaction between the capping groups and the solvent, which will provide an energetic barrier to counteract the van der Waals and for magnetic materials/magnetic attractions, between nanoparticles [49]. To help arrest these nanoparticles, different solvents are also used to change the solubility or the reaction rate [49, 53].

Stabilising nanoparticles by use of a capping agent and various solvents has also been reported to have a great influence on the shape as well as the crystallite structural properties of the final product [53].

2.4.2 Growth Methods

While there are many physical and chemical ways to synthesize nanomaterials such as chemical vapour deposition [54, 55], high energy ball milling [56], pulsed laser ablation [57], physical vapour deposition [56], sputter deposition [59], colloidal route [60], sol-gel methods [61], solvothermal and hydrothermal chemical methods [62, 63]; the solution phase chemical methods provide an economical friendly, low energy and convenient way to obtain nanomaterials. Some solution based chemical methods that have been applied to synthesize nanomaterials include: the solvothermal method, hydrothermal method, sol-gel method, sonochemical method, and reflux method. The solvothermal method is a relatively low temperature technique

where an organic solvent is used as a reaction medium in a closed reaction vessel such as an autoclave. A pressure build up is realized during the reaction and contributes to the reaction. This method had been used extensively in the synthesis of different crystalline nanostructures such as ZnO, TiO_2, GaN, and Ag, to mention a few [64-67]. The hydrothermal method is similar to the solvothermal method, except water is used as a solvent instead of an organic solvent. The advantage of this method is the use of water in the reaction and it has been reported to produce good crystalline phase nanomaterials [68-70]. The sonochemical method is a method where nanomaterials are obtained through application of powerful ultrasound radiation [71]. This method is known to produce size selective particles in the synthesis [71]. The reflux method involves carrying out a reaction at the boiling point of the solvent which is kept from evaporating by the help of a condenser. Most reactions take place under an inert atmosphere to prevent oxidation of the intended product [72, 73] and a solvent is heated above its boiling temperature in order to produce enough energy to promote the desired reaction followed by later cooling to obtain the products.

2.4.2.1 Microwave-assisted synthesis of nanostructures

The microwave heating method has been used widely in the world of chemistry over the past decades especially for organic synthesis and for digestion of materials for analysis [74-78]. More recently microwave chemistry has been considered for material synthesis and in nanotechnology applications [75-82]. Most of the inorganic materials synthesized in the laboratory require very high temperatures and long reaction periods. The advantage of microwave irradiation heating in chemical synthesis of nanomaterials is the quick heating, higher reaction rates and the low energy consumption requirements of this method [83].

Microwave assisted inorganic material synthesis is a clean method of synthesis that is affordable and reactions are fast with materials produced with a reported high purity and a narrow size distribution of nanoparticles [84]. Although the new microwave ovens designed for chemical reactions can be

quite expensive, the ability to perform multiple reactions at the same time and over a short period of time coupled with other feature reduces the cost implications. The improved heating method is achieved in microwave reactors by localized heating unlike the type of heating realized when using conventional methods of heating. This is an important parameter that affects the formation of nanomaterials. Fig. 2.6 shows the different heating a sample experiences with many microwave heating and conventional heating. In conventional heating, reactants are slowly activated by a conventional external heat source. Heat passes through the walls of the vessel in order to reach the reaction contents [85]. In microwave heating, there is a direct coupling between the microwaves and the molecules in the reaction mixture, which results in a fast temperature rise. Early application of microwave synthesis involved the use of kitchen microwave ovens, which introduced various concerns such as safety due to absence of temperature and pressure controls [86]. This limited the amount of information that could be extracted until more chemical friendly microwave reactors were designed. These include the multimode microwave systems that have been commercially built specifically for chemical reactions. This system is pressure programmed with a limit of 60 bars and other controllable parameters include; temperature, time, stirrer speed and cooling [87].

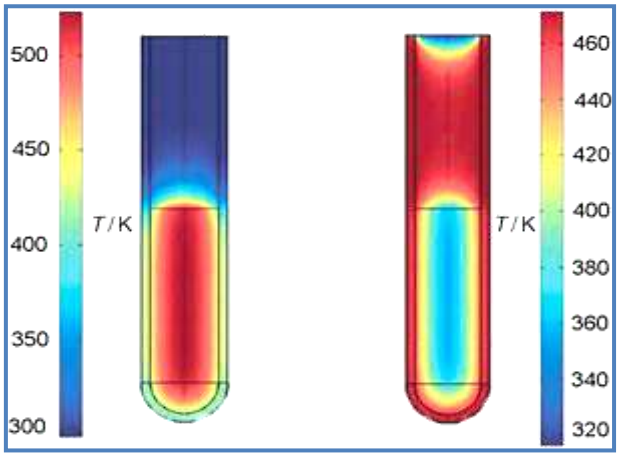


Figure 2.6: Inverted temperature gradients in microwave versus the conventional oil-bath heating: Difference in temperature profiles after 1 min of microwave irradiation (left) and treatment in an oil-bath (right) [88].

2.4.2.2 Basic principles of microwave chemistry

Microwaves are electromagnetic waves whose wavelength lies in the range 0.01 mm to 1 m (frequency range 0.3 to 300 GHz). A large part of the microwave spectrum is used in point to point communication, TV broadcasting via satellites and in RADAR systems. Microwaves are also used for heating in industrial, biomedical, chemical and in scientific research applications [89]. However, only a few frequencies are allowed for microwave application in industry, science and medicine, with the most common being the 2.45 GHz frequency. When microwaves irradiate a dielectric material, various phenomena occur which is dependent on the nature of the electromagnetic waves. Two main mechanisms account for their use in nanomaterial chemical synthesis viz; dipolar polarization and ionic conduction [90].

The dipolar polarization takes place when polar solvent molecules or reagents form part of the reaction. Since these molecules have an electrical dipole moment, they align themselves in the direction of the applied electric field. Meanwhile the magnetic field alternates, and the molecular dipoles try to align themselves with the filed [91]. In this process, energy is lost in the form of heat through molecular friction and dielectric loss [92].

The ionic conduction takes place when charged particles are involved in the reaction. The ions also oscillate due to introduction of electric field and in the process collide with neighbouring molecules or atoms [90]. The collisions cause agitation which results in heat formation.

Chen et al. have successfully synthesized inorganic nanomaterials using a microwave irradiation procedure [94]. One of the interesting observations from the study related to the shape change of the Ag nanomaterials as different power levels and different precursor concentrations were applied [94]. Other researchers have also reported a change in particle shape, size, and product distribution when the ramping temperature and heating times were varied. This is in addition to the effect of metal salt and surfactant concentration, reaction temperature, and the solvents that also affected the product shape [82].

2.5 Gallium Nitride nano-materials

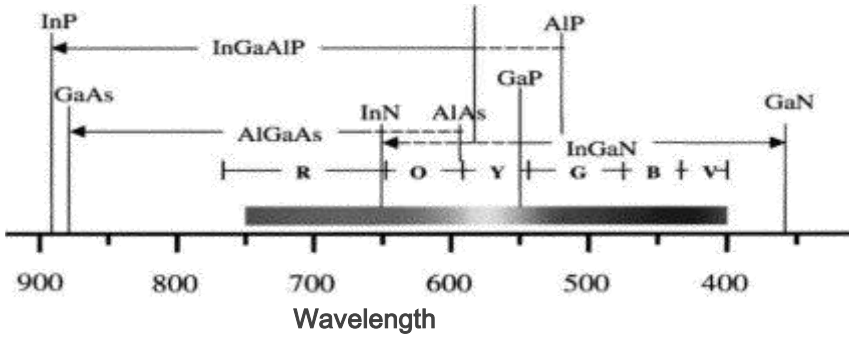


Figure 2.7: Various ternary and quaternary materials used for light emitting diodes with the wavelength ranges between 400 and 900 nm [10].

Fig. 2.7 shows the application of the group III-V semiconductor materials as light emitting diodes according to their specific wavelengths. GaAs has a band gap of 1.42 eV at room temperature and it is one of the compound semiconductors that have been widely used in electronic device fabrication [10, 95, & 96] i.e. in diodes, microcircuits, field effect transistors, and in solar cells [48]. GaAs has been used quite successfully in industry.

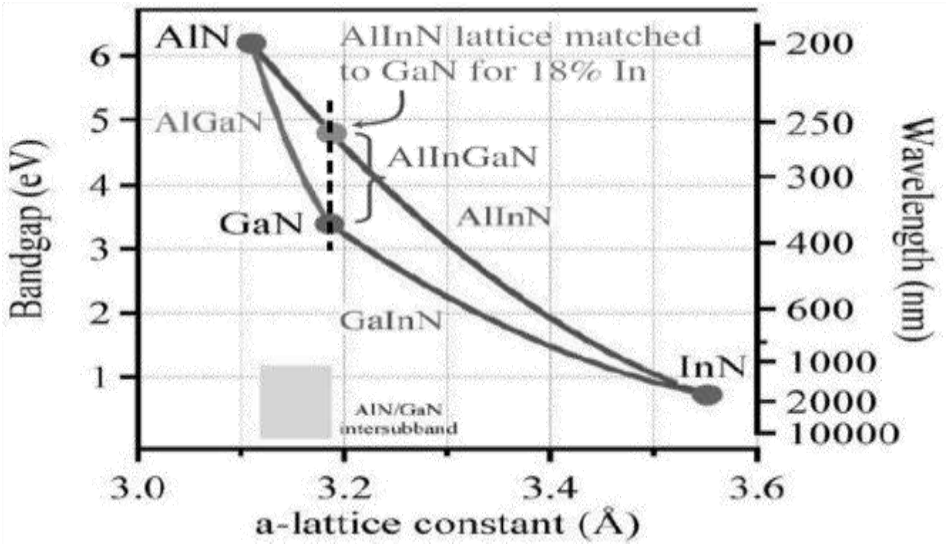


Figure 2.8: Independent variation of the band gap and lattice constants for the nitride based quaternaries [97].

Amongst the group III nitride based nanostructures AlGaN, AlN, GaN and InN nanomaterials have received much attention over the past years due to their interesting optoelectronic and electronic applications [98-100]. However, these materials have not been explored as much as GaAs. Their energy band gaps cover a wide spectrum and their variation with corresponding lattice constants is shown in Fig. 2.8. Different techniques that have been used to synthesize these materials include chemical vapour deposition [95], laser ablation [101], and arc discharge [102]. Chattopadhyay et al. published a review on the growth of 1-D group III nitrides which reported on various ways to synthesize these types of materials as well as their properties and their applications in nano-sensing and nano-optoelectronics environments [103].

GaN, like most nitride materials, normally crystallises in the wurtzite structure, under ambient conditions [104]. This structure has a hexagonal unit cell and lattice constants *a* and *c*. The space grouping when using the Hermann-Mauguin notation is $P6_3mc$ and the point group symmetry is *6mm*. This structure consists of two interpenetrating hexagonal close packed sub-lattices, each with one type of atom, offset along the *c*-axis by 5/8 of the cell height [105]. It also consists of alternating diatomic close-packed (0001) planes of Ga and N pairs; hence the stacking sequence of the (0001) plane is AaBbAa in the (0001) direction [105]. The stacking order of the GaN wurtzite structure along the (0001) *c*-direction (AaBa) is shown in Fig. 2.9

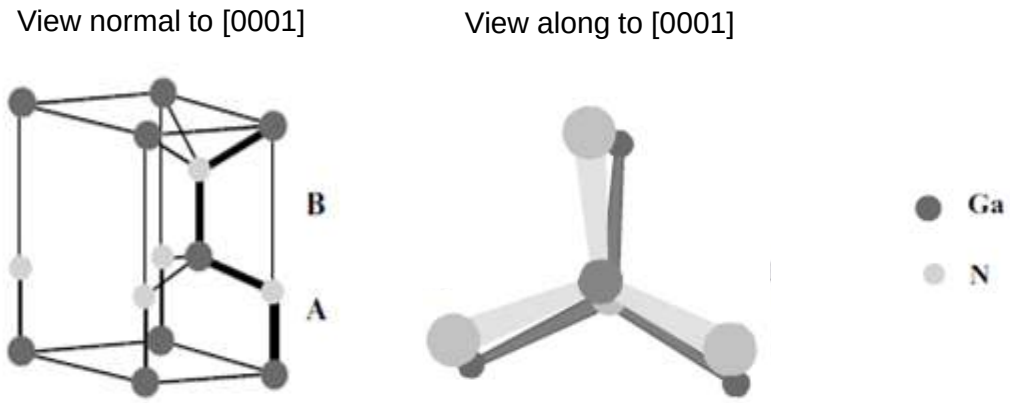


Figure 2.9: A stick-and-ball stacking model of crystals with 2H wurtzitic polytypes. The bonds in an A-plane are indicated with heavier lines to highlight the stacking sequence. The left figure shows a 3-D view while the right figure shows the (0001) plane projection for the wurtzite phase [106]

Chang and Wu have reported a temperature (T) controlled catalytic growth of 1-D GaN nanowires using a gallium organometallic precursor [107]. They used a dual temperature zone furnace with the first zone being a low T zone and the second being a high T zone. Their precursor was vaporised using a 100 sccm NH_3 flow and carried from the low T zone to the second T zone of a T range of 550-850 ^oC. In their samples they observed different GaN morphologies as a function of T. Several other reports show that the CVD synthesis of GaN nanowires by ammoniating Ga oxides e.g. Ga_2O_3 at temperatures between 850 and 1000 ^oC is feasible [35, 108].

Soluble GaN nanocrystals have been synthesized by Cheng et al. via a solution phase chemical synthesis [107]. Their reaction took place in a round bottom flask under inert conditions. They used a gallium source ($GaCl_3$), a nitrogen source (Li_3N), a capping agent (trioctylphosphine oxide; TOPO) and a solvent (dibenzofuran). They synthesized GaN nanocrystals at 290 ^oC under ambient pressure conditions. The TOPO and dibenzofuran ratio was varied in order to manipulate the GaN crystal size. From their studies they observed that dibenzofuran controlled the crystal size of the particles. Further, their XRD analysis showed that they had synthesised GaN nanocrystals [107]. There is not much work that has been done on the synthesis of GaN by solution methods. In some cases, soluble Ga metal salt

precursors are used to fabricate specific Ga-O/Ga-OH complexes which are later ammoniated at higher temperatures to produce GaN with tuned structures [109-111].

2.6 Nickel Sulphide nano-materials

Nickel and sulphur form various phases which include NiS, NiS_2, Ni_3S_4, Ni_9S_8, Ni_7S_8 and Ni_3S_2. NiS display hexagonal and rhomboherdal phases which have interesting electrical and catalytic properties. Hexagonal NiS shows a metal-insulator transition (MIT) at approximately 264 K. This transition occurs parallel to a paramagnetic-anti-ferromagnetic property change with an anti-ferromagnetic moment of $2\mu_B$ per Ni^+ ions [112]. This has attracted intensive research on this material with the goal of finding possible reasons for the transition and to identify mechanisms for the transition [113-115].

The interest in this material dates back to the early 1960's, when the existence of the transition was discovered by Sparks and Komto [116]. Fujimori et al, have done much research on the physical properties of materials that exhibit MIT [116, 117]. One of the notable things for NiS transitions, unlike many other materials, is its transition being associated with a change in lattice parameters and unit cell volume of the crystal structure but with no change in the crystal symmetry. Okamura et al carried out optical studies on the NiS transition and confirmed an energy gap of 0.2-0.3 eV at the transition [113]. They also showed that the energy gap was dependent on the temperature as well as on the Ni stoichiometry, where an increase in gap was observed with decreasing temperature, while a decrease in gap was observed with increasing Ni stoichiometry for $Ni_{1-\delta}S$ ($0.002 < \delta < 0.02$). Fig. 2.10 shows the phase diagram of α-NiS.

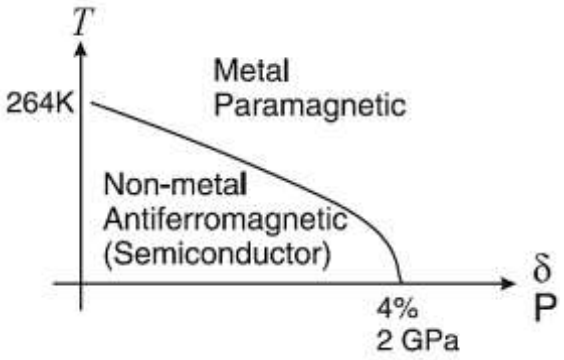


Figure 2.10: A schematic phase diagram of $Ni_{1-\delta}S$ in terms of temperature (T), Ni vacancy concentration (δ), and external hydrostatic pressure (P). Image copied from reference [113]

NiS nanostructured materials have in general been synthesized by unsophisticated methods. Soft chemical routes have been employed for the synthesis of inorganic nano-materials for a long time. Methods that have been used to make these materials include a slow precipitation method, a direct infiltration self-assembly route, a single source precursor route and a hydrothermal method [118, 119]. Some of the solution chemical methods that have been used to synthesize NiS are summarized in Table 2.1. The table only shows the solution phase chemical synthesis of NiS (both rhombohedral and hexagonal phases). However, other nickel sulphide polymorphs can be synthesized via the same method by changing parameters such as Ni:S ratio, solvent, precursor and temperature.

Pan et al. reported on the synthesis of flower and rod like NiS nanostructures using distilled water as a solvent [118]. In their experiment, they used nickel acetate as a Ni source and thiourea as a source of S. They heated a given ratio of the precursors, dissolved in distilled water at 200 ^{o}C, for 48 hours in a Teflon-lined autoclave. After drying the product in air, they obtained flower and rod like NiS with the phase confirmed by XRD.

Ni foil and S powder in deionized water have been reported by Zhang et al. to make oriented nanostructured films of NiS [119]. In a typical reaction, a known size of Ni foil and a known quantity of S powder were placed in a Teflon-lined autoclave and 15 ml deionized water was added. The reaction

was carried for a period of 12 hours under a constant 180 ^{o}C temperature followed by washing and drying of the product.

In some cases, a stabilising agent is added into the reaction mixture when using the soft chemical routes to synthesize different nanostructures [94, 111 & 120]. This is done to control the size and shape of the nanomaterial at a nanoscale during synthesis. Stabilizers that have been used include trioctyl phosphine oxide (TOPO), hexadecylamine (HDA), polyvinyl pyrrolidone (PVP), polyvinyl alcohol (PVA), polyethylene glycol (PEG), trioctylphosphine (TOP) and sodium dodecyl sulphate. A mixture of the stabilizers is sometimes used instead.

Table 2.1 Summary of previous work done on solution chemical synthesis of NiS nanostructures.

Growth method	**Materials**	**Solvent**	**T (^oC)**	**Time (h)**	**Morphology**	**Thickness**	**Phase**	**Reference**
Hydrothermal -autoclave	$Ni(CH_3COO)_2.4H_2O$ and $Na_2S_2O_3.5H_2O$	Distilled H_2O	200	12	Nanobelts	70-200 nm	α-	Wang et al. [121]
Hydrothermal -autoclave	$Ni(NO_3)_2.6H_2O$ and Thioglycolic acid	Distilled H_2O	180	12	Hierarchical	100-400 nm	β-	Salavati-Niasari [122]
Hydrothermal -autoclave	$Ni(CH_3COO)_2$ and $(NH_2)_2CS$	Distilled H_2O	200	4	Layers	-	α-	Sun [123]
Hydrothermal -autoclave	Na_2S and $Ni(OH)_2$	NaOH	180	48	Nanorod based microspheres	50-100 nm	α- & β-	Wang et al. [124]
Hydrothermal -autoclave	$NiCl_2.6H_2O$ and $(NH_2)_2CS$	$N_2H_4.H_2O$	100-120 140-180	24	Lamella-based seaurchin-like Rod-based seaurchin-like	3-6 μm 30-50 nm	α- β-	Liu [125]
Hydrothermal	$Ni(NO_3)_2.6H_2O$,	Distilled	220	24	Flowers	2-4 μm	β-	Zhou et al.

-autoclave	NaSCN and CTAB	H_2O						[126]
Hydrothermal -autoclave	Ni foil and S powder	Deionized H_2O	180	12	Dendrites		-	Zhang et al. [119]
Hydrothermal -autoclave	$NiCl_2.6H_2O$ and S powder	Deionized H_2O + NaOH	160	24	Hexagonal flakes	200 nm	α-	Ma et al. [127]
Hydrothermal -autoclave	$NiSO_4$ and $(NH_2)_2CS$	Deionized H_2O	170	10	Nanoflakes – based flowers	1 μm	α-	Tang, et al. [128]
Hydrothermal -microwave	$NiCl_2.6H_2O$, PEG and $Na_2S.9H_2O$	Distilled H_2O	170	1	Needle-based starfish-like	20-35 nm	α-	Bo et al. [129]
Hydrothermal -autoclave	$Ni(CH_3COO)_2.4H_2O$ and $(NH_2)_2CS$	Distilled H_2O	200	48	Rod-based flowers	30-80 nm	β-	Pan et al. [118]
Hydrothermal -autoclave	$Ni(NO_3)_2.6H_2O$, $(NH_2)_2CS$ and en	Distilled H_2O	160	24	Petal-like structures	5 μm	α-	Dong et al. [127]
Hydrothermal -autoclave	$NiSO_4.6H_2O$, cysteine and dodecanethiol	Distilled H_2O	180	12	Nanoflake-based hollow spheres	2-10 μm	β-	Zhao et al. [131]
Hydrothermal -autoclave	$Ni(OH)_2$ and $(NH_2)_2CS$	Distilled H_2O	150	10	Nanoplatelets	4.7 μm	α- & β-	Zhao et al. [132]

Solvothermal -autoclave	$NiCl_2.6H_2O$ and $Na_2S_2O_3.5H_2O$	en	225	120	Rods	1-4 μm	β-	Shuguang et al. [133]
Solvothermal -autoclave	$Ni(CH_3COO)_2.4H_2O$ and $C_{13}H_{12}N_4S$	en	220	5	Nanoneedle-based urchin-like	150 nm 30 μm	β-	Zhang et al. [134]
Polyol-glass flask	$NiCl_2.6H_2O$, $N_2H_4.H_2O$ and $(NH_2)_2CS$	EG	158	7	Chain-like tubes	280-320 nm	β-	Zhang et al. [135]
Solvothermal -autoclave	$NiCl_2.6H_2O$, $N_2H_4.H_2O$ and elemental S	Ethanol Pyridine	110	10-12	Nanoparticles Nanorods	10 nm 30 nm	α- & β-	Meng et al. [136]
Polyol-reflux condenser	$NiCl_2.H_2O$ and $(NH_2)_2CS$	EG	-	2	hierarchical	200-300 nm	α-	[137]
Colloidal chemical process	$Ni(acac)_2$ and elemental S	Oleylamine	140	1	Nanocrystals	-	α-	Zhang et al. [138]
Hydrothermal -autoclave	$NiCl_2.6H_2O$, $C_6H_5Na_3O_7 \cdot 2H_2O$ and $_L$- cysteine	Distilled H_2O and NH_3 (pH =	180	24	Thin flake-based nanoflowers	5-5 μm	α-	Jiang et al. [139]

		10)						
Hydrothermal -microwave	$Ni(CH_3COO)_2.4H_2O$, $(NH_2)_2CS$, $Na_3C_6H_5O_7.2H_2O$	Deionized H_2O, and NH_3 (pH = 12)	140 180	1/4	Prismatic particles Prismatic particles and needles	500-900 nm 2-3 μm 400-600 nm	α- α- & β-	Idris et al. [140]
Hydrothermal -autoclave	$NiSO_4$, NaOH and thioacetamide	Deionized H_2O	160	24	Monodisperse nanoparticles	20-50 nm	β-	Guo et al. [141]
Reflux	$Ni(acac)_2$ and 1-dodecanethiol	Oleylamine	280	5	Nanorods	20 nm	β-	Chi et al. [142]

2.7 References

[1] Rasmussen, J.W., Martinez, E., Louka, P., Wingett. D.G., *Expert, Opin. Drug Deliv.* **7** (2010) 1063.

[2] Saracino, G.A.A., Coqoqnini, D., Silva, D., Caprini, A., Gelain, F., *Chem. Soc. Rev.* **42** (2013) 225.

[3] Shi, H., Barnard, A.S., Snook, I.K., *J. Mater. Chem.* **22** (2012) 18119.

[4] Beberwyk, B.J., Surendranath, Y., Alivisatos, A.P., *J. Phys. Chem. C* **117** (2013) 19759.

[5] Raki, L., Beaudoin, J., Alizadeh, R., Makar, J., Sato, T., *Materials* **3** (2010) 918.

[6] Roco, M.C., Bainbridge, W.S., *J. Nanoparticle Res.* **7** (2005) 1.

[7] Pokropivny, V.V., Skorokhod, V.V., *Phisica E* **40** (2008) 2521.

[8] Lin, K.-F., Cheng, H.-M., Hsu, H.-C., Lin, L.-J., Hsieh, W.-F., *Chem. Phys. Lett.* **409** (2005) 208.

[9] Alivisatos, A.P., *Science* **271** (1996) 993.

[10] Grahn, H.T., *Singapore World Scientific Publishing Co. Pte, Ltd.* (1999).

[11] Pearton, S.J., Ren, F., Zhang, A.P., Lee, K.P., *Mater. Sci. Eng. R* **30** (2000) 55.

[12] Wang, Y., Herron, N., *J. Phys. Chem.* **95** (1991) 525.

[13] Cao, G., *Singapore World Scientific Publishing Co. Pte, Ltd.* (2004).

[14] Liqiang, J., Yichun, Q., Baiqi, W., Shudan, L., Baojiang, J., Libin, Y., Wei, F., Honggang, F., Jaizhong, S., *Solar Energy Materials & Solar Cells* **90** (2006) 1773.

[15] Feldmann, C., *Nanoscale* **3** (2011) 1947.

[16] Zhang, Q., Uchaker, E., Candelaria, S.L., Cao, G., *Chem. Soc. Rev.* **42** (2013) 3127.

[17] Kalyanasundaram, K., Gratzel, M., *J. Mater. Chem.* **22** (2012) 24190.

[18] Dai, L., Chang, D.W., Baek, J.-B., Lu, W., *Small* **8** (2012) 1130.

[19] Luo, Y., Li, L., Huang, S., Chen, T., Luo, H., *J. Nanomaterials* **2013** (2013) 1.

[20] Han, I., Islam, A., Chen, H., Malapaka, B., Chiranjeevi, B., Zhang, S., Yang, A., Yanagida, M., *Energy and Environmental. Sci.* **5** (2012) 6057.

[21] Lee, Y.-L., Lo, Y.-S., Adv. *Functional Materials* **19** (2009) 604.

[22] Ruhle, S., Shalom, Menny, Zaban, A., *Chem Phys. Chem.* **11** (2010) 2290.

[23] Kim, D.-K., Lu, N., Ghaffari, R., Rogers, J.A., *NPG Asia Mater.* **4** (2012) 1.

[24] Snow, E.S., Novak, J.P., Lay, M.D., Houser, E.H., Perkins, F.K., Campbell, P.M., *J. Vac. Sci. Technol. B* **22** (2004) 1990.

[25] Kumar, S., Cola, B.A., Jackson, R., Graham, S., *J. Electron. Packag.* **133** (2011) 1.

[26] Allen, A.C., Sunden, E., Cannon, A., Graham, S., King, W., *Appl. Phys. Lett.* **88** (2006) 1.

[27] Ding, B., Wang, M., Wang, X., Yu, J., Sun, G., *materialstoday* **13** (2010) 16.

[28] Liu, X., Cheng, S., Liu, H., Hu, S., Zhang, D., Ning, H., *Sensors* **12** (2012) 9635.

[29] Hu, B., Chen, W., Zhou, J., *Sensors and Actuators B* **176** (2013) 522.

[30] Han, W., Redlich, P., Ernst, F., Ruehle, M., *Appl. Phys. Lett.* **122** (2000) 652.

[31] Rahman, M.M., Ahmmad, A.J.S., Jin, J.H., Ahn, S.J., Lee, J.J., *Sensors* **10** (2010) 4855.

[32] Peng, L., Zhao, Q., Wang, D., Zhai, J., Wang, P., Pang, S., Xie, T., Sensors and Actuators B **136** (2009) 80.

[33] Zhai, J., Wang, D., Peng, L., Lin, Y., Li, X., Xie, T., *Sensors and Actuators* **147** (2010) 234.

[34] Hung, N.L., Kim, H., Hong, S.-K., Kim, D., *Adv. Nat. Sci. Nanosci. Nanotechnol.* **2** (2011) 015002

[35] Kim, S.S., Park, J.Y., Choi, S.-W., Kim, H.S., Na, H.G., Yang, J.C., Lee, C., Kim, H.W*., Int. J. Hydrogen Energy* **36** (2001) 2313.

[36] Park, S., An, S., Ko, H., Lee, S., Lee, C., *Sensors and Actuators B:* **188** (2013) 1270

[37] Fang, X., Zhai, T., Gautam, U.K., Li, L., Wu, L., Bando, Y., Golberg, D., *Progress in Mater. Sci.* **56** (2011) 175.

[38] Korotcenkov, G., *Mater. Sci. Eng. B* **139** (2007) 1.

[39] Das, S.N., Kar, J.P., Choi, J.-H., Lee, T.I., Moon, K.-J., Myoung, J.-M., *J. Phys. Chem. C* **114** (2010) 1689.

[40] Zhang, W., Feng, C., Yang, Z., *Sensors and Actuators B: Chemical* **165** (2012) 62.

[41] Li, Y., Wlodarski, W., Galatsis, K., Moslih, S.H., Cole, J., Russo, S., Rockelmann, N., *Sensors and Actuators B* **83** (2002) 160.

[42] Tomchenko, A.A., Harmer, G.P., Marquis, B.T., Allen, J.W., *Sensors and Actuators B* **93** (2003) 126.

[43] Zhai, T., Fang, X., Liao, M., Xu, X., Zeng, H., Yoshio, B., Golberg, D., *Sensors* **9** (2009) 6504.

[44] Wang, Y., Chen, J., Wu, X., *Materials Letters* **49** (2001) 361.

[45] Lupan, O., Chai, G., Chow, L., *Microelectronic Engineering* **85** (2008) 2220.

[46] Ramgir, N., Datta, N., Kaur, M., Kailasaganaoathi, S., Debnath, A.K., Aswal, D.K., Gupta, S.K., *Colloids and Surfaces A: Physicochem. Eng. Aspects* **439** (2013) 101.

[47] Liu, D., Liu, T., Zhang, H., Lv, C., Zeng, W., Zhang, *J., Mater. Sci. Semiconductor Processing* **15** (2012) 438.

[48] Gad, A.E., Hoffmann, M.W.G., Hernandez-Ramirez, F., Prades, J.D., Shen, H., Mathur, S., *Mater. Chem. Phys.* **135** (2012) 618.

[49] Burda, C., Chen, X., Narayanan, R., El-Sayed, M.A., *Chem. Rev.* **105** (2005) 1025.

[50] Zhang, Q., Liu, S.-J., Yu, S.-H., *J. Mater. Chem.* **19** (2009) 191.

[51] Akhtar, M.S., Khan, M.A., Jeon, M.S., Yang, O.-B., *Electrochimica Acta* **53** (2008) 7869.

[52] Cozzoli, P.D., Kornowski, A., Weller, H., *J. Am. Chem. Soc.* **125** (2003) 14539.

[53] Peng, Z.A., Peng, X., *J. Am. Chem. Soc.* **123** (2001) 183.

[54] Che, G., Lakshmi, B.B., Martin, C.R., Fisher, E.R., *Chem. Mater.* **10** (1998) 260.

[55] Kong, J., Cassel, A.M., Dai, H., Chem. Phys. Lett. **292** (1998) 567.

[56] Chen, Y., Li, C.P., Chen, H., Chen, Y., *Sci. Technol. Adv. Mater.* **2** (2006) 839.

[57] Gondal, M.A., Yamani, Z.H. Drmosh, Q.A., Rashid. A., *Int. J. Nanoparticles* **2** (2009) 119.

[58] Wang, L., Zhang, X., Zhao, S., Zhou, G., Zhou, Y., Qi, J., *Appl. Phys. Lett.* **86** (2005) 1.

[59] Asanithi, P., Chaiyakun, S., Limsuwan, P., *J. Nanomaterials* **2012** (2012) 1.

[60] Zheng, N., Fan, J., Stucky, G.D., *J. Am. Chem. Soc.* **128** (2006) 6550.

[61] Mackenzie, J.D., Bescher, E.P., *Acc. Chem. Res*. **40** (2007) 810.

[62] Han, S., Kong, M., Guo, Y., Wang, M., *Mater. Lett.* **63** (2009) 1192.

[63] Zhang, J., Gao, L., *Mater. Chem. Phys.* **87** (2004) 10.

[64] Xu, L., Hu, Y.-L., Pelligra, C., Chen, C.-H., Jin, L., Huang, H., Sithambaram, S., Aindow, M., Joesten, R., Suib, S.L., *Chem. Mater*. **21** (2009) 2875.

[65] Yang, H.G., Liu, G., Qiao, S.Z., Sun, C.H., Jin, Y.G., Smith, S.C., Zou, J., Cheng, H.M., Lu, G.Q., *J. Am. Chem. Soc.* **131** (2009) 4078.

[66] Grocholl, L., Wang, J., Gillan, G., *Chem. Mater.* **13** (2001) 4290.

[67] Yang, Y., Matsubara, S., Xiong, L., Huyakawa, T., Nogami, M., *J. Phys. Chem. C* **111** (2007) 9095.

[68] Nguyen, V.N., Nguyen, N.K.T., Nguyen, P.H., *Adv. Nat. Sci.: Nanosci. Nanotechnol.* **2** (2011) 1.

[69] Baruah, S., Dutta, J., *Sci. Technol. Adv. Mater.* **10** (2009) 1.

[70] Djurisic, A.B., Xi, Y.Y., Hsu, Y.F., Chan, W.K., *Recent Pat. Nanotechnol.* **2** (2007) 121.

[71] Rao, C.N.R., Muller, A., Cheetham, A.K., *WILEY-VCH Verlag GmnH & Co. KGaA* (2004).

[72] Gupta, S., Neeleshwar, S., Kumar, V., Chen, Y.Y., *Adv. Mat. Lett.* **3** (2012) 54.

[73] Xu, L., Sithambaram, S., Zhang, Y., Chen, C.-H., Jin, L., Joesten, R., Suib, S.L., *Chem. Mater.* **21** (2009) 1253.

[74] Gedye, R., Smith, F., Westaway, K., Ali, H., Baldisera, L., Laberge, L., Rousell, J., *Tetrahedron Lett.* **27** (1986) 279.

[75] Giguere, R.J., Bray, T.L., Duncan, S.M., Majetich, G., *Tetrahedron Lett.* **27** (1986) 4945.

[76] Lidstrom, P., Tierney, J., Wathey, B., Westman, J., *Tetrahedron* **57** (2001) 9225.

[77] Zlotorzynski, A., *Crit. Rev. Anal. Chem.* **25** (1995) 43.

[78] Lamble, K.J., Hill, S.J., *Analyst R* **123** (1998) 103.

[79] Barlow, S., Marder, S.R., *Adv. Funct. Mater.* **13** (2004) 517.

[80] Perelaer, J., de Gans, B.J., Schubert, U.S., *Adv. Mater.* **18** (2006) 2101.

[81] Zhu, Y.J., Wang, W.W., Qi, R.J., Hu, X.L., *Angew. Chem.* **116** (2004) 1434.

[82] Tsuji, M., Hashimoto, M., Nishizawa, Y., Kubokawa, M., Tsuji, T., *Chem. Eur. J.* **11** (2005) 440.

[83] Ji, Z., Sun, J., Shen, X., Zhu, G., *Cryst. Res. Technol.* (2013) 1.

[84] Soltani N., Saion, E., Hussein, M.Z., Erfani, M., Abedini, A., Bahmanrokh, G., Navasery, M., Vaziri, P., *Int. J. Mol. Sci.* **13** (2012) 12242.

[85] Surati, M.A., Jauhari, S., Desai, K.R., *Arch. Appl. Sci. Res.* **4** (2012) 465.

[86] Gaba, M., Dhingra, N., *Ind. J. Pharm. Edu. Res.* **45** (2011) 175.

[87] Harrison, K.L., Manthiram, A., *Inorg. Chem.* **50** (2011) 3613.

[88] Kappe, C.O., Angew. *Chem. Int. Ed.* **43** (2004) 6250.

[89] Saxana, V.K., Chandra, U., *InTech publishing* (2011).

[90] Atkins, T.M., Louie, A.Y., Kauzlarich, S.M., Nanotechnology **23** (2012) 1.

[91] Xu, R., Pang, W., Huo, Q., *Elsevier* (2011).

[92] Gabriel, C., Gabriel, S., Grant, E.H., Grant, E.H., Halstead, B.S.J., Mingos, D.M.P., *Chem. Soc. Rev.* **27** (1998), 213.

[93] Baghbanzadeh, M., Carbone, L., Cozzoli, P.D., Kappe, C.O., *Angew. Chem. Int. Ed.* **50** (2011) 11312.

[94] Chen, C., Zhu, G., Zhu, X., Qiao, X., Chen, J., *J. Mater. Sci*. **22** (2011) 1788.

[95] Robinson, A.L., *Science* **219** (1983) 275.

[96] Uryu, T., Yoshinanga, J., Yanagisawa, Y., *J. Industrial Ecology* **7** (2003) 103.

[97] http://www.ee.sc.edu/personal/faculty/simin/ELCT871/02%20GaN%20Properties.pdf.

[98] Pearton, S.J., Kang, B.S., Gila, B.P., Norton, D.P., Kryliouk, O., Ren, F., Heo, Y.W., Chang, C.Y., Chi, G.C., Wang, W.M., Chen, L.C., *J. Nanosci. Nanotechnol.* **8** (2008) 99.

[99] Chu, B.H., Kang, B.S., Hung, S.C., Chen, K.H., Ren, F., Sciullo, A., Gila, B.P., Pearton, S.J., J. Diabet. *Sci. Technol.* **4** (2010) 171.

[100] Nakamura, S., *J. Vac. Sci. Technol.* A **13** (1995) 705.

[101] Kim, H.M., Choo, Y.H., Lee, H., Kim, S.I., Ryu, S.R., Kim, D.Y., Kang, T.W., Chung, K.S., *Nano Lett.* **4** (2004) 1059.

[102] Goodwin, T.J., Leppert, V.J., Risbud, S.H., Kennedy, L.M., Lee, H.W.H., *Appl. Phys. Lett.* **70** (1997) 3122.

[103] Chattopadhyay, S., Ganguly, A., Chen, K.H., Chen, L.C., *Crit. Rev. Solid State Mater. Sci.* **34** (2009) 224.

[104] Cantarero, A., Cros, A., Garro, N., Gomez-Gomez, M.I., Garcia-Cristobal, A., de Lima Jr., M.M., Daudin, B., Rizzi, A., Denker, C., Malindretos, J., *Ann. Phys.* **523** (2011) 51.

[105] Morkoc, H., *Wiley-VCH Verlag GmbH & Co KGaA* (2013).

[106] Morkoc, H., *Wiley-VCH Verlag GmbH & Co KGaA* (2008).

[107] Chen, C.C., Liang, C.H*., J. Sci. Eng.* **5** (2002) 223.

[108] Yang, L., Xue, C., Wang, C., Li, H., *Nanotechnology* **14** (2003) 50.

[109] Qiu, H., Cao, C., Zhu, H., *Mater. Sci. Eng. B* **136** (2007) 33.

[110] Bao, K., Shi, L., Liu, X., Chen, C., Mao, W., Zhu, L., Cao, J., J. Nanomat. **2010** (2010)1.

[111] Chen, Y., Maniruzzaman, M., Kim, J., *Int. J. Precision Eng. Manufact.* **12** (2011) 573

[112] Sparks, J.T., Komto, T., *Phys. Lett.* **25** (1967) 398.

[113] Okamura, H., Naitoh, J., Nanba, T., Matoba, M., Nishioka, M., Anzai, S., Shimoyama, I., Fukui, K., Muira, H., Nakagawa, H., Nakagawa, K., Kinoshita, T., *Solid State Commun.* **112** (1999) 91.

[114] Fujimori, A., Namatame, H., Matoba, M., Anzani, S., *Phys. Rev. B* **42** (1990) 20.

[115] Lioutas, Ch.B., Manolikas, C., Van Tendeloo, G., Van Landuyt, J., *J. Cryst. Growth* **126** (1993) 457.

[116] Sparks, J.T., Komoto, T. *J. Appl. Phys.* **34** (1963) 1191.

[117] Nakamura, M., Sekiyama, A., Namatame, H., Kino, H., Fujimori, A., Misu, A., Ikorna, H., Matoba, M., Anzai, S., *Phys. Rev. Lett.* **73** (1994) 2891.

[118] Pan, Q., Huang, K., Ni, S., Yang, F., He, D., *Materials Research Bulletin* **43** (2008) 1440.

[119] Zhang, L., Yu, J.C., Mo, M., Wu, L., Li, Q., Kwong, K.W., *J. AM. Chem. Soc.* **126** (2004) 8116.

[120] Mthethwa, T., Rajasekhar Pullabotla, V.S.R., Mdluli, P.S., Wesely-Smith, J., Revaprasadu, N., *Polyhedron* **28** (2009) 2977.

[121] Wang, L., Zhu, Y., Li, H., Li, Q., Qian, Y. *J. Solid State Chem.* **183** (2010) 223.

[122] Salavati-Niasari, M., Davar, F., Emadi, H., *Chalcogenide Lett.* **7** (2010) 647.

[123] Sun, X., *Appl. Surf. Sci*. **217** (2003) 23.

[124] Wang, Y., Zhu, Q., Tao, L., Su, X., *J. Mater. Chem.* **21** (2011) 9248.

[125] Liu, X. *Mater. Sci. Engineering B* **119** (2005) 19.

[126] Zhou, H., Lv, B., Wu, D., Sun, Y., *Particuology* **10** (2012) 783.

[127] Ma, Z., Liu, K., *Adv. Mater. Research* **503-504** (2012) 459.

[128] Tang, C., Zang, C., Su, J., Zhang, D., Li, G., Zhang, Y., Yu, K., *Appl. Surf. Sci.* **257** (2011) 3388.

[129] Bo, B., Xuemei, H., Pengpeng, W., Weisheng, G., Proc. SPIE 7493 (2012) 1.

[130] Dong, W., An, L, Wang, X., Li, B., Chen, B., Tang, W., Li, C., Wang, G., *J. Alloys Cpds.* **509** (2011) 2170.

[131] Zhao, P., Zeng, Q., Huang, K., *Materials Letters* **63** (2009) 313.

[132] Zhao, W., Zhu, X., Bi, H., Cui, H., Sun, S., Huang, F., *J. Power Source* **242** (2013) 28.

[133] Shuguang, C., Zeng, K., Li, H., Li, F., *J. Solid State Chem.* **180** (2011) 1989.

[134] Zhang, W., Xu, L., Tang, K., Li, F., Qian, Y., *Eur. J. Inorg. Chem.* (2005) 653.

[135] Zhang, Y.-H., Guo, L., He, L., Liu, K., Chen, C., Zhang, Q., Wu, Z., Nanotechnology 18 (2007) 1.

[136] Meng, Z., Peng, Y., Xu, L., Qian, Y., *Materials Letters* **53** (2002) 165.

[137] Wang, J., Chew, S.Y., Wexler, D., Wang, G.X., Ng, S.H., Zhong, S., Liu, H.K., *Electrochem. Commun.* **9** (2007) 1877.

[138] Zhang, H.T., Wu, G., Chen, X.H., *Materials Lett.* **59** (2005) 3728.

[139] Jiang, J., Yu, R., Yi, R., Qin, W., Qiu, G., Liu, X., *J. Alloys Cpds.* **493** (2010) 529.

[140] Idris, N.H., Rahman, M.M., Chou, S.L., Wang, J.Z., Wexler, D., Liu, H.-K., *Electrochimica Acta* **58** (2011) 456.

[141] Guo, H., Ke, Y., Wang, D., Lin, K., Shen, R., Chen, J., Weng, W., *J. Nanopart. Res.* **15** (2013) 1475.

[142] Chi, W.S., Han, J.W., Yang, S., Roh, D.K., Lee, H., Kim, J.H., *Chem. Commun.* **48** (2012) 9501.

Chapter 3: MW-assisted synthesis of NiS_2 nanostructures and their PL properties

3.0 Preamble

This chapter deals with just one of the many phases of nickel sulphide, NiS_2, we have been able to obtain in this study. Some of the contents of this chapter were published recently [a]. The reported work includes the morphological analysis of NiS_2, phase and their photoluminescence (PL) properties.

3.1 Introduction

Transition metal chalcogenide nanomaterials e.g. CdS, ZnO, ZnS, SnO, SnS, CoS, CuS, CuS_2, FeS_2, CoS_2 and NiS_2 have received considerable attention over the years owing to the novel properties observed when compared to their bulk counterparts which results from a quantum confinement effect [1-6]. These material's properties such as opto-electronic, mechanical and chemical properties have aroused intensive investigations for new applications including use in catalysis and in optical and magnetic devices. The nickel disulfide (NiS_2) alloy adopts a pyrite structure and is known to be an antiferromagnetic insulator with a band gap of about 0.3 eV. Its narrow band gap has attracted attention for possible applications in the semiconductor industry especially in infrared emitters and detectors [7]. Methods that have been used to synthesize these types of materials include chemical vapour deposition, solid-state reactions and wet chemical thermal techniques [8-12]. The microwave assisted hydrothermal technique has become one of the methods for nanoscale synthesis [13]. This is because microwave addition to hydrothermal reactions provides quick, straightforward, and inexpensive ways of attaining the desired products from a given chemical reaction. The microwave provides uniform heating of the reaction promoting

[a] Linganiso, E.C., Mhlanga, S.D., Coville, N.J., Mwakikunga, B.W. "Size-dependent and intra-band photoluminescence of NiS_2 nano-alloys synthesized by microwave assisted hydrothermal technique" *J. Alloys Compd.* **552** (2013) 345.

uniform distribution of the product materials, which is not obtained when using conventional heating technique. Also, the solvents used can be green; hazardous by-products are prevented. This makes microwave reactors to be potential alternatives for bulk synthesis of nanomaterials for industrial applications. Challenges such as control of nanomaterial particle size, and morphology can be overcome by controlling various parameters e.g. solvent, reaction time, temperature, pressure etc. Addition of a stabilising agent to control the size and morphology on nanomaterials has been widely studied and shown to be alternative way of obtaining crystalline nanostructures with desired properties. This however is limited to the type of application of the nanomaterials one has in mind.

3.2 Experimental

3.2.1 Reagents and sample preparation

All reagents used were purchased from the Sigma Aldrich chemical company and were used as received without any further purification. To synthesize NiS_2 nanostructures, 1.552 g $Ni(CH_3COO)_2.4H_2O$ was added to an ethanol solution containing 0.400 g sulfur. The mixture was then transferred to a Multiwave 3000 microwave oven that was operated at 600 W for 30 minutes and fan cooled to room temperature for 20 minutes. The black precipitate formed was washed several times with ethanol and dried in an oven at 90 ^oC for 6 hours to optimize for NiS_2 formation. The reaction was repeated and the power used was changed to 700 W and 800 W. Further, the reaction was repeated in the presence of 5.00 g HDA in order to control the size of the nanostructures formed.

3.2.2 Characterization

The phases of the as-synthesized materials were investigated using X-ray diffraction [Philips PW 1830 X-ray diffractometer with a Cu Kα (λ = 0.154 nm)]. Sample morphologies were studied using SEM (JOEL 2000) and high resolution transmission electron microscopy (HR-TEM Joel-Jem 2100). The PL spectra of the as-synthesized samples were recorded at room temperature from 310 nm to 800 nm using a Horiba Jobin Yvon HR320 Spectro-fulorometer

by exciting the samples with the 300 nm line of a deuterium lamp. The emission was detected with a Jobin-Yvon MPT detector.

Density functional theory simulations were carried out using the generalized gradient approximation (GGA) [14] for the exchange and correlation functional, as implemented in the CASTEP code [15]. The interaction between the ionic cores and the valence electrons is described using the ultrasoft pseudo potential of Vanderbilt [16]. The Brillouin zone is sampled using the scheme of Monkhorst and Pack [17]. This k-points sampling gives a good convergence to the total energy calculations. A kinetic energy cut-off of 300 eV was used for the plane wave expansion of the wavefunctions. The positions of all atoms in the NiS_2 unit cell were relaxed using the conjugate gradient algorithm with a tolerance of $2x10^{-5}$ eV for maximal change in total energy. Calculations were considered converged when the residual forces were less than 0.05 eV/Å. The electronic states were occupied in accordance with the Fermi distribution function using a Fermi smearing parameter of k_BT= 0.20 eV.

3.3 Results and discussion

3.3.1 Phase analysis

In order to confirm the product phase synthesized, XRD analysis was carried out. Cubic phase NiS_2 product was confirmed by XRD analysis which corresponds to the literature data (NiS_2: JCPDS Card number 11-0099) with the cell constant a = 5.68 Å. It can be seen form Fig. 3.1 that the NiS_2 formation was optimised at 800 W microwave power level. The increased microwave power level increases the rate at which the product is formed. The crystallite size for the sample synthesized at 800 W was estimated using the Scherrer equation given in Equation 1.

$$D = \frac{K\lambda}{\beta \cos\theta} \qquad (1)$$

where D is the average dimension of the crystallites, K is a constant (usually applied as 0.9), λ (0.154 nm) is the wavelength of the $CuK\alpha_1$ x-ray, β is the full width at half maximum of the diffraction peak (inaccuracies associated with stress and instrumental broadening are expected), and θ is the Bragg angle. The average crystallite size for NiS_2 was estimated

using the reflections shown in Table 1 and 2 and the average obtained was 35 nm. This suggests that the NiS_2 materials prepared are in the nano-range.

Further, the effect of precursor concentration was studied to see its effect on both diameter distribution and size of the products. Fig. 3.2 shows xrd pattern of cubic NiS_2 products obtained from 0.08 M, 0.16 M and 0.4 M precursor concentrations, while other parameters were kept constant at 800 W, 220 ^oC, and 60 minutes. Crystallite size variation with precursor concentration was estimated by applying Scherrer equation to 200 reflection and the results are summarized in Table 1. An increase in crystallite size with increased precursor concentration was observed for the NiS_2 products.

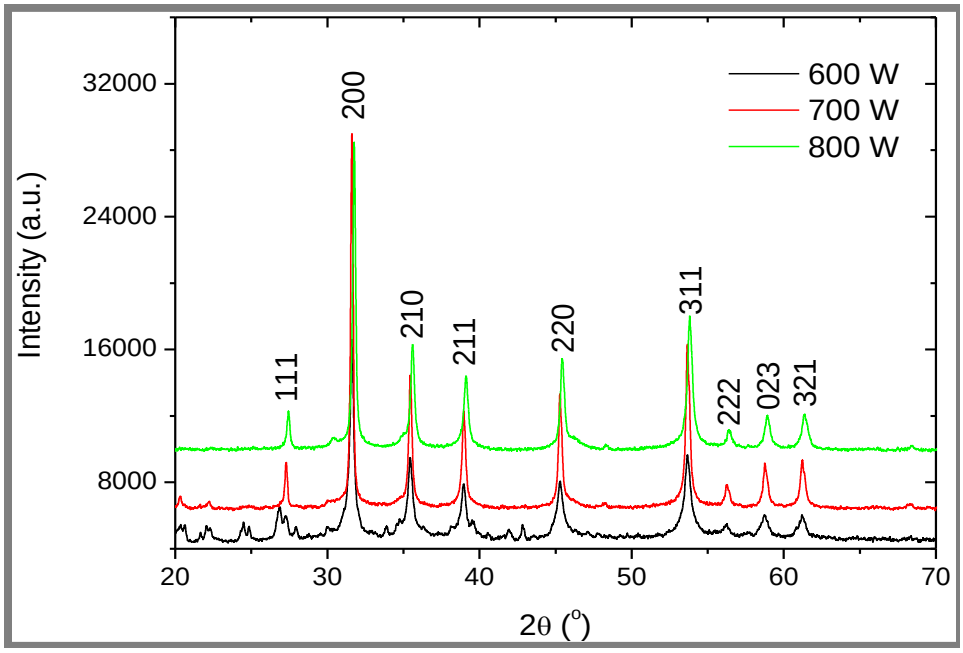


Figure 3.1: XRD pattern of cubic NiS_2 microstructures synthesized at various microwave power levels.

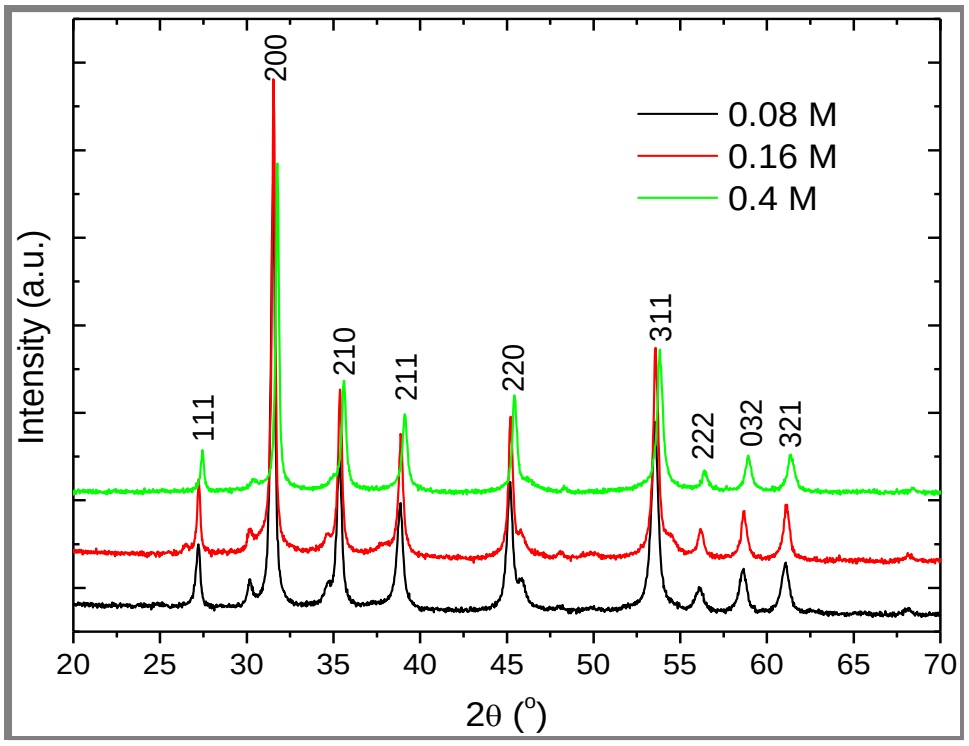


Figure 3.2: XRD pattern of cubic NiS_2 microstructures synthesized using different precursor concentrations while keeping other parameters constant.

Table 3.1: Average crystallite size of the NiS_2 nanostructures synthesized using different precursor concentrations.

Precursor concentration (M)	200 orientation peak position (°)	D (Scherrer = kλ/βcosϴ) [nm]
0.08	31.509	30.4
0.16	31.545	38.7
0.4	31.764	40.9

The same phase was also obtained when HDA capping agent was added to the reaction. It can be observed from Fig. 3.3 that the diffraction peak widths are broad, which is an indication of a small crystallite size. For the HDA capped NiS_2 the average crystallite size was estimated by the Scherrer equation to be 9 nm as shown in Table 2. This is a size control effect of the capping agent on the nanostructures.

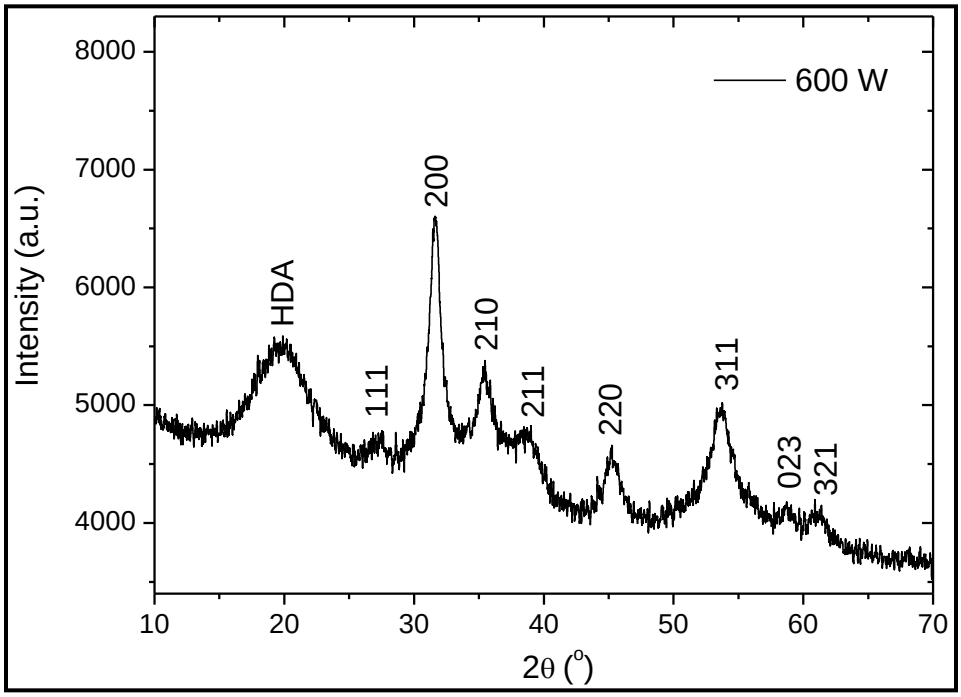


Figure 3.3: XRD profile for the NiS_2 material synthesized in the presence of 5 g HDA which acts as a capping agent.

Table 3.2: Average crystallite size of the NiS_2 nanostructures estimated using the Scherrer equation.

Peak orientation	**D (Scherrer = kλ/βcosϴ) [nm]**	
	Uncapped	**HDA capped**
111	43	14
200	41	9.5
210	32	9.5
211	27	3
220	31	7
Average	34.5 (+/-6)	9 (+/- 4)

3.3.2 Microscopy analysis

Evenly distributed hierarchal microparticles with rough surfaces were observed in the SEM images for all the samples synthesized at different microwave power levels without HDA addition. The images are shown in Fig. 3.4. The average particle size distribution was measured from the SEM images using the image*J* programme. It can be seen from the size distribution that the average size increases from about 300 nm to 500 nm with increased power level which is due to the increased microwave heating rate as the power is increased. From the rough surfaces it can be seen that these hierarchal microparticles are a result of small particles that assemble to form big agglomerates. The size of these structures is a result of progressive Ostwald ripening growth process. In this process; the smallest units of the elements dissolved in solution come together to form particles that grow further to form hierarchal agglomerates. The proposed growth mechanism for these structures is given in Scheme 1.

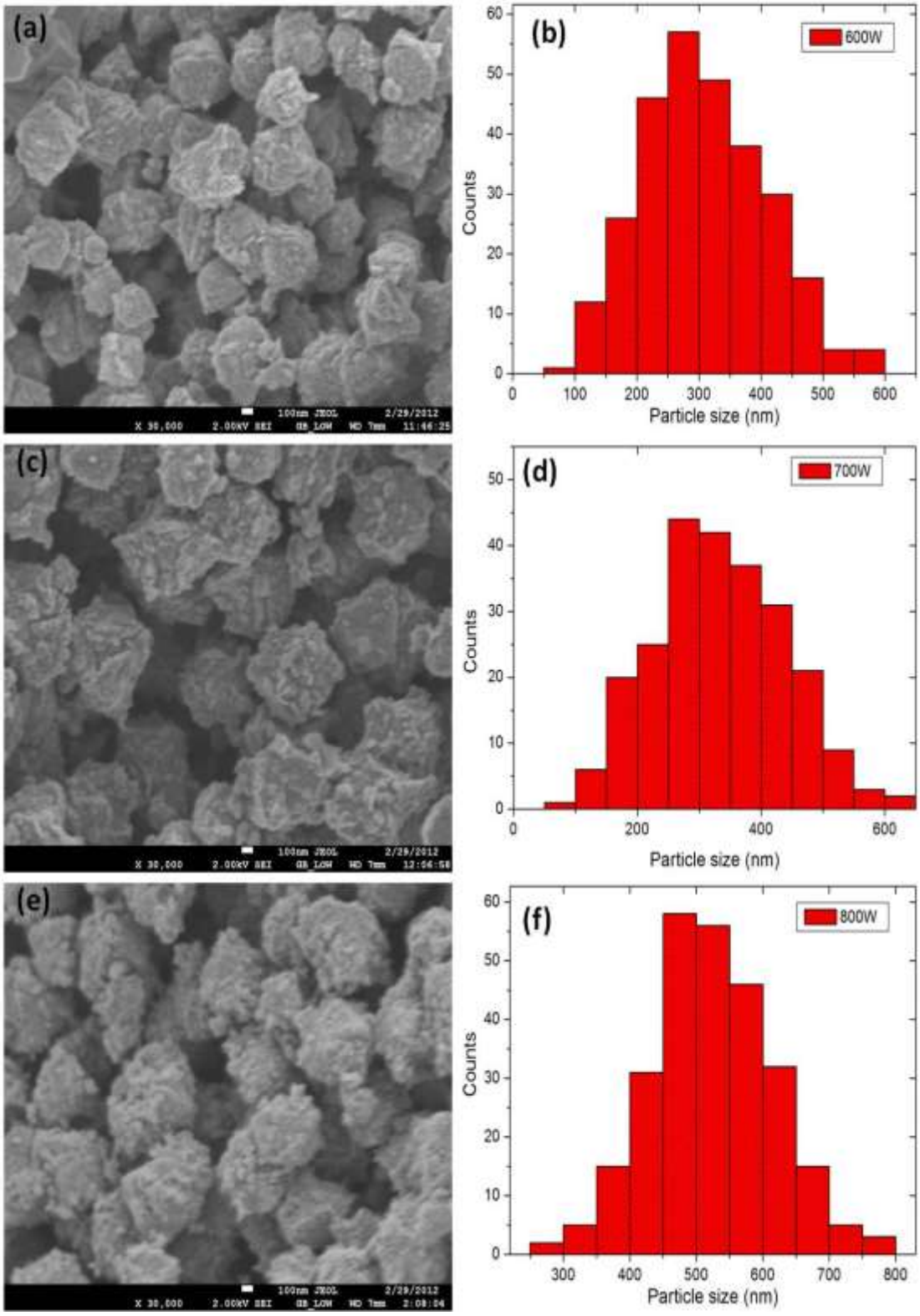


Figure 3.4: SEM images of the samples synthesized at 600 W (a), 700 W (c), 800 W (e), and their corresponding particle size distribution in (b), (d) and (f) respectively.

Fig. 3.5 shows the images of NiS_2 products obtained at different precursors concentrations. The average diameter of the particles was estimated using image*J* programme. It can be seen from the figure that the average diameter of about 150 nm was obtained at 0.08 M and 0.16 M concentrations, and an average diameter of about 500 nm was obtained at 0.4 M precursor concentrations. The difference in outer diameter size can be attributed to difference in competing ionic species in solution during the growth process.

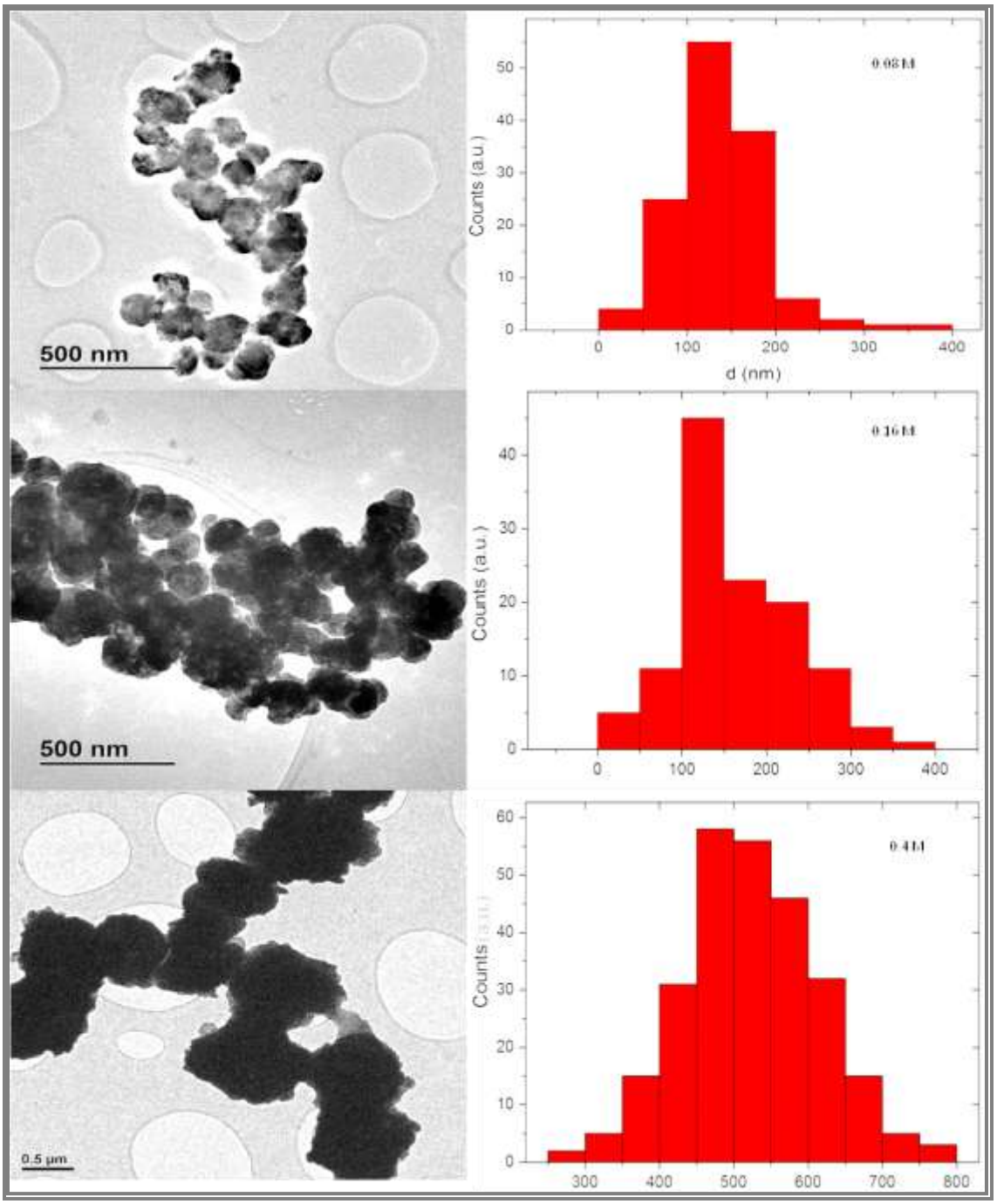


Figure 3.5: SEM images of the samples synthesized using Ni(Ac) concentrations 0.08 M, 0.16 M, 0.4 M and their corresponding particle size distribution from top to bottom respectively.

When HDA was added to the reaction to act as a capping agent, the size of the NiS_2 structures was reduced to a nanometer scale as shown in Fig. 3.6 (a) and (b). It was not possible to see the crystallites by SEM due to their small size. However, it can be seen in Fig. 3.6 (a) that the sample looks like flakes which is a result of the presence of the HDA capping agent. HR-TEM analysis shown in Fig. 3.6 (b) reveals that the NiS_2 particles formed were spherical with an average crystallite size of about 3 nm. The small size is a result of the added HDA capping agent which prevented large particle growth as well as particle agglomeration.

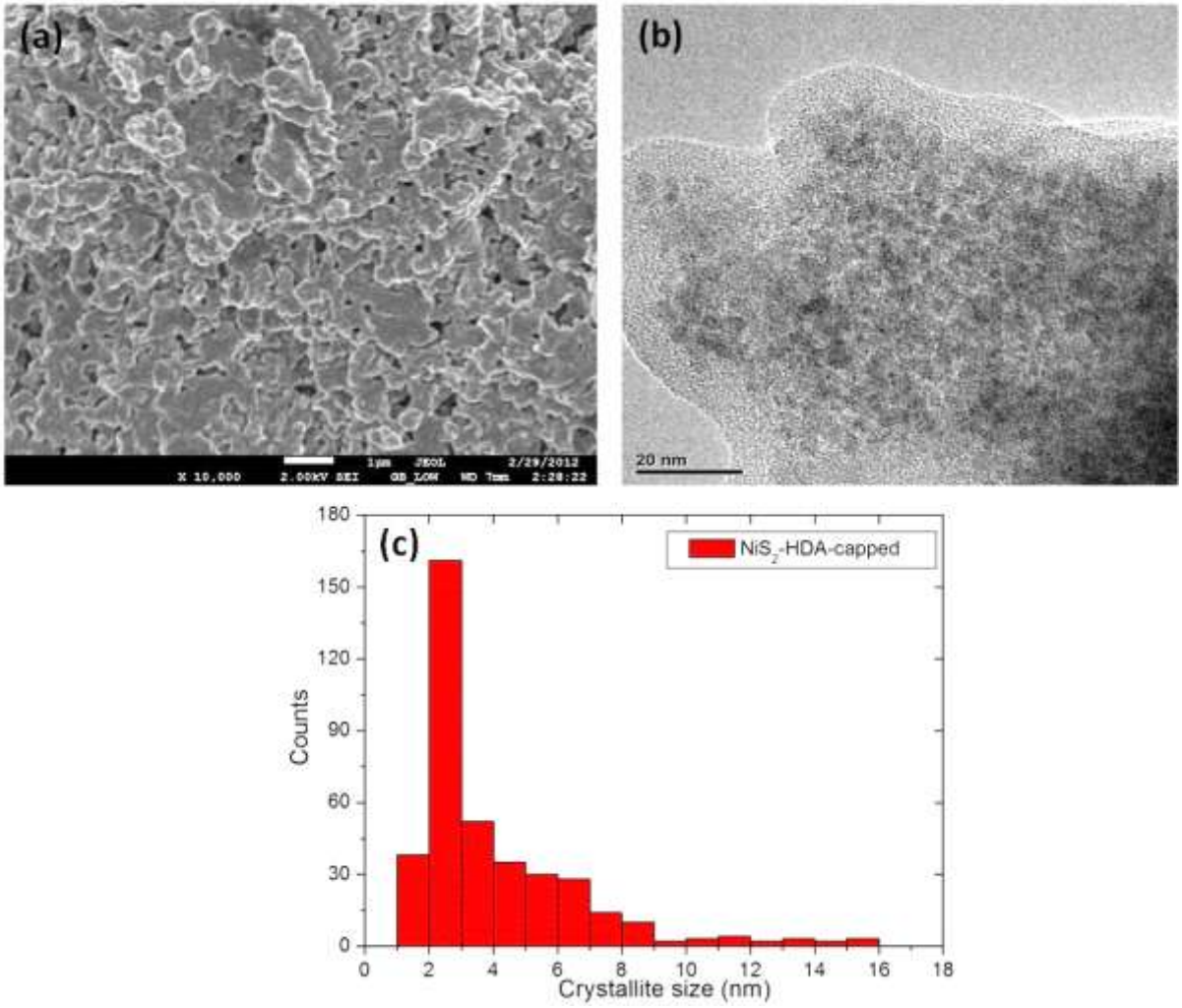
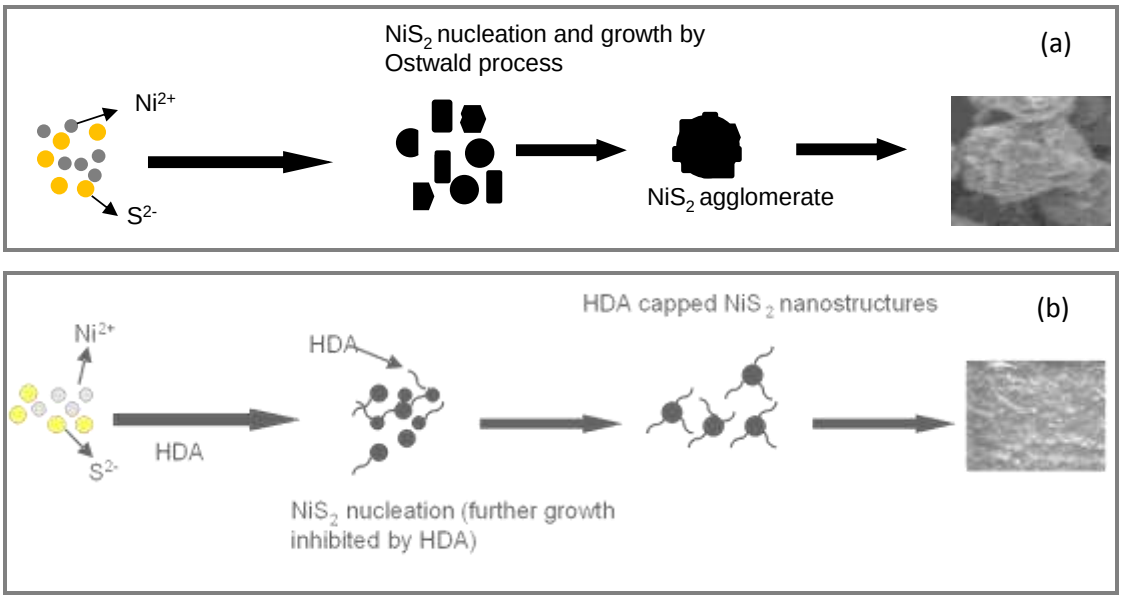


Figure 3.6: SEM (a) and HR-TEM (b) images of NiS_2 nanostructures synthesized at 600 W in the presence of 5 g HDA capping agent. The crystallite size distribution measured from the HR-TEM images is shown in (c).



Scheme 3.1: Proposed growth mechanisms of bare NiS_2 nano-clusters (a) and HDA capped NiS_2 nano-particles (b).

3.3.3 Photoluminescence

Fig. 3.7 shows room temperature PL spectra of the NiS_2 hierarchical structures and HDA capped NiS_2 nanocrystals excited at 300 nm. A UV broad emission peak which is comprised of four peaks located at about 400 nm (3.10 eV), 428 nm (2.90 eV), 447 nm (2.77 eV) and 464 nm (2.67 eV) was observed. The presence of more than one peak may be due to the presence of structural defects within the samples. A second and much more intense PL emission peak was observed in the near IR region. Three peaks were evident with emission maxima located at 710 nm (1.75 eV), 751 nm (1.65 eV)/754 nm (1.64 eV) [NiS_2/HDA-capped NiS_2] and 784 nm (1.58 eV). Both the UV and the near IR emissions observed in our study appear at a much higher energy when compared to the reported band gap of NiS_2 which is within the range 0.3-0.8 eV. The observed emissions can therefore be attributed to intra-band transitions that take place on the NiS_2 band structure during excitation. The multi peaks could also be due to excess S induced energy state transitions. This observation has not been reported for NiS_2 structures before. Wang et al. reported PL results of NiS_2 microspheres of 5 μm constructed of cuboids with 500 nm mean side length. Their fluorescence spectrum was recorded from 270 to 500 nm using an excitation wavelength of 277 nm [18]. Their spectrum

did not show any fluorescence in this recorded region. So if we assume that bulk NiS_2 does not show fluorescence, we can then attribute the observed emissions to a nanosize effect. Further, most materials that are closely related to NiS_2 like FeS_2, CoS_2 and CuS_2 do not show this behaviour. However, the UV emission band with quadruple fine structure was reported by Denzler et al. for colloidal ZnS nanocrystals. Their UV peaks appeared at 416, 424, 430, and 438 nm. They attributed the peaks to transitions that involve vacancy states and interstitial states for Zn and S atoms [19]. Further, they observed low intensity peaks in the IR region which they attributed to transitions between distinct localized states in the gap due to impurities and imperfections [19]. The intense emission peaks they observed in the UV region could also be supported by the wide band gap of ZnS, which is 3.7 eV. Intense emission peaks in the IR region in our case are due to the narrow band gap of NiS_2 material. In addition to the intra-band emission accounted for in this report, NiO nanostructures show room temperature photoluminescence at 400 nm. The chemisorption of oxygen on the NiS_2 surface could be another possible explanation for the UV emission observed in this study. Detailed surface analysis is recommended for better understanding of the surface properties of the synthesized material. It can be observed for both emissions that the small size HDA-capped NiS_2 nanocrystals show enhanced emission when compared to the uncapped NiS_2 structures. This is due to the smaller size of the capped nanocrystals and is in good agreement with what has been reported for other nanomaterials in the literature [20]. The small shift of the HDA capped nanoparticles could be attributed to an increased level of defects due to the smaller size of the NiS_2 particles.

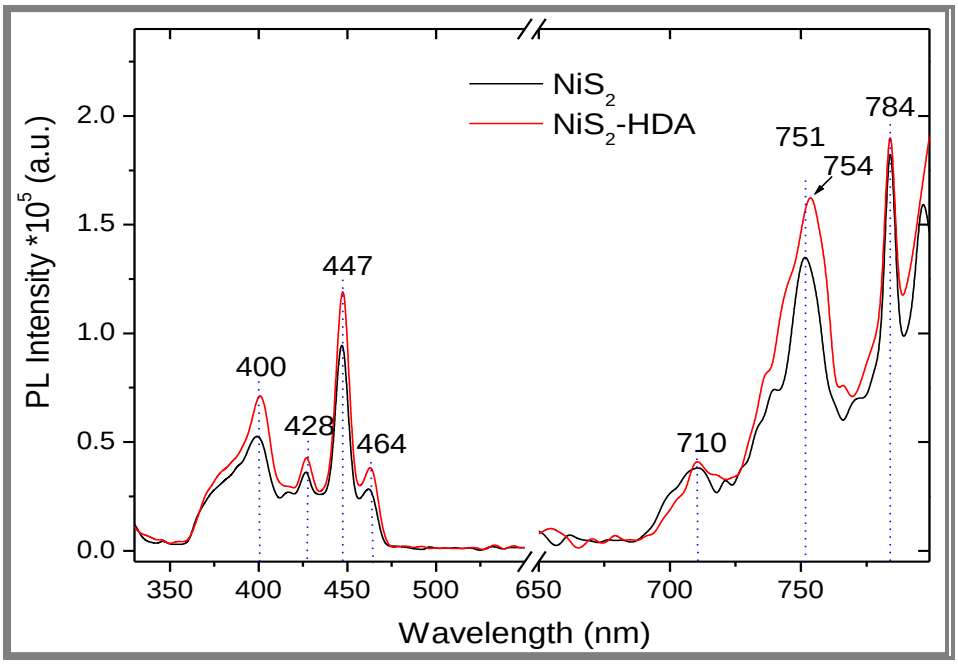


Figure 3.7: Photoluminescence spectra of the as-synthesized hierarchal and the HDA-capped NiS_2 nanostructures excited at λ = 325 nm.

The band energy structure and the local density of states (LDOS) calculated for NiS_2 are shown in Fig. 3.8 (a) and (b). The LDOS spectra shows that the electrons near Fermi level energies (E_F) are mostly from the Ni 3*d* and S 3*p* energy bands. It can also be seen that most electrons active at the lower bands are from 3*p* and 3*s* orbitals which are likely to belong to S atoms. This observation is in agreement with what has been reported in literature, where NiS_2 band opening was attributed to Ni *eg*-orbital splitting via LDA calculations combined with dynamic mean field theory (DMFT) [21]. Kunes et al. did similar calculations accompanied by experimental x-ray photoemission spectroscopy measurements [22]. Their NiS_2 spectral density also shows S-*p* density dominating far from the E_F which suggests dominant S contribution at these energies. This suggests that intra-band transition in the NiS_2 structure is likely due to the presence of S atoms.

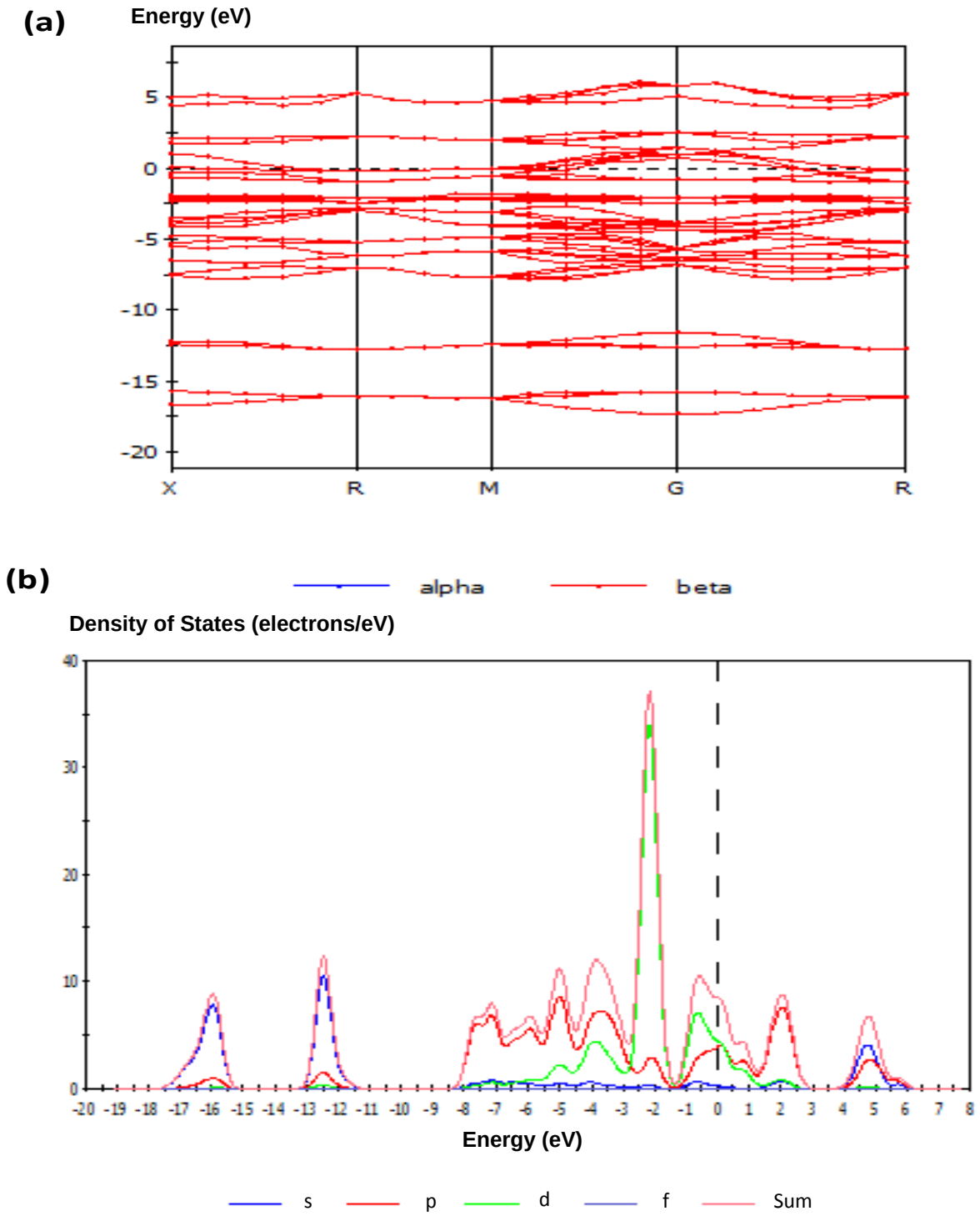


Figure 3.8: (a) The band energy structure of NiS_2 and (b) the electron states of Ni(3*d*), Ni-S hybridisation and S (3*s* and 3*p*) partial density of states.

In as far as the photoluminescence features appearing at various wavelengths, we considered the gamma, G, line of symmetry in the calculated band structure. The bands around the gamma point G in the Brillouin zone of the NiS_2 system in Fig. 3.9 were truncated. The gamma point (where $\pi a/\lambda = 0$) being the centre of the Brillouin zone is appropriate when the photon wavelength,λ of excitation (325 nm) is much longer than the lattice parameter of the NiS_2 system (a ~ 0.568 nm). The energy differences in the band structure as truncated in Fig. 9 were carefully identified to the emission energies in the PL spectra in Fig. 3.7. The luminescence features at wavelengths of 400 nm (3.10 eV), 428 nm (2.90 eV), 447 nm (2.77 eV) and 464 nm (2.67) were attributed to some of those electrons de-exciting from S (3*p*) levels down to the Ni (3*d*) (blue to UV emission) whereas those features at wavelengths of 710 nm (1.75 eV), 751 nm (1.65 eV)/754 nm (1.64 eV) [NiS_2/HDA-capped NiS_2] and 784 nm (1.58 eV) respectively resulted from de-excitations between either Ni(3*d*) or S (3*s*,3*p*) levels and Ni-S hybridization levels (red to near IR emission).

No band-to-band transitions were observed in the experimental PL which suggests that Ni (3*d*) electrons, being close to the Fermi level, do not participate in the visible, near IR and UV emissions. They may be emitting far into the infra-red region which was beyond the detection limits of the PL instrument used for these experiments.

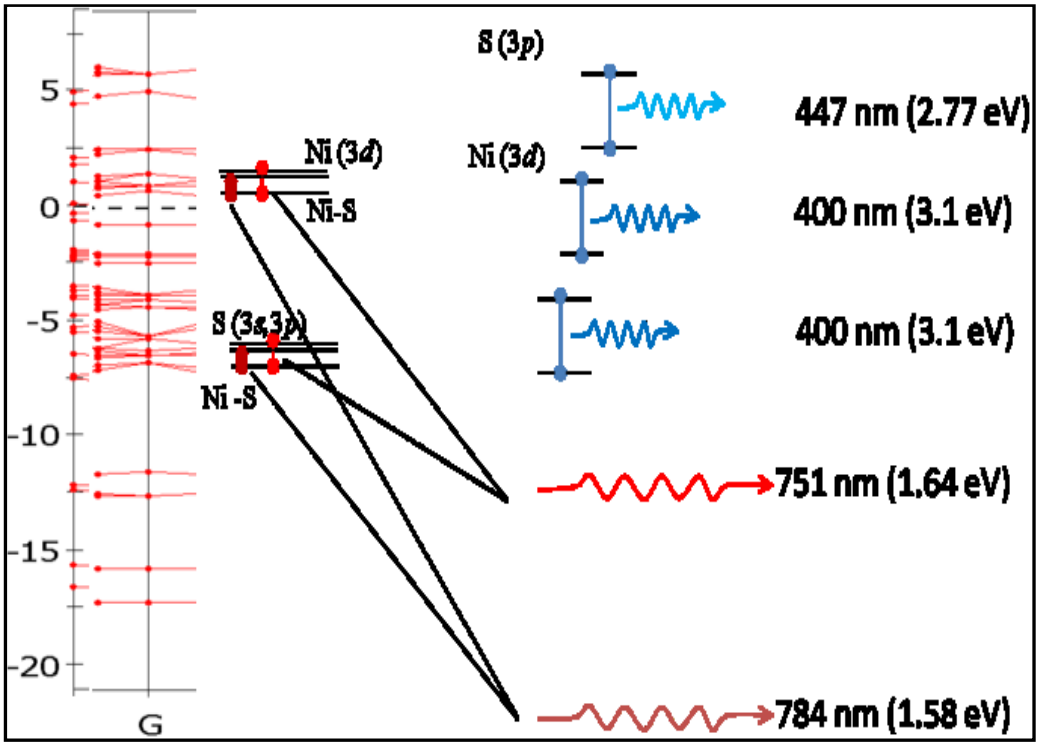


Figure 3.9: Band structure around the gamma point G of the Brillouin zone of the NiS_2 system. Both the 751 nm and 784 nm feature in the PL spectra are identified on this energy diagram as de-excitations either from Ni (3d) or S(3*s*,3*p*) to Ni-S hybridization energy states whereas the luminescence features from 400-464 nm are attributed to S(3p) to Ni(3d) electron relaxations.

3.4 Conclusions

NiS_2 nanostructures have been synthesized through the microwave irradiated thermal technique by heating a mixture of nickel acetate and sulphur in methanol solution. Varying the microwave power level yielded different sized particles with bigger agglomerates of about 500 nm average particle size. XRD analysis showed that the crystallite size of the synthesized material was in the nano-range suggesting that the huge agglomerated particles observed during SEM analysis for the samples synthesized without the addition of a stabilising agent were self-assembled smaller particles. Precursor concentration was also studied to examine its effect on particle morphology and size. NiS_2 nanostructured agglomerated with average particle sizes in the 150 nm range were obtained at 0.08 M precursor concentration. Addition of HDA as a capping agent yielded a NiS_2 with smaller particle sizes of about 9 nm. The smaller size effect due to HDA addition was seen in the PL emission properties of the samples. HDA capped NiS_2 nanostructures showed enhanced PL emission when compared to the uncapped and bigger size NiS_2. The emissions in both samples were attributed to intra-band transitions mostly due to the sulphur content in the samples according to the calculated band energy structure and partial density of states.

3.5 References

[1] Tilley, R.D., Jefferson, D.A., *J. Phys. Chem. B* **106** (2002) 10895.

[2] Salavati-Niasari, M., Davar, F., Mazaheri, M., *J Alloys Compd.* **470** (2009) 502.

[3] Salavati-Niasari, M., Davar, F., Mazaheri, M., *Mater Res Bull* **44** (2009) 2246.

[4] Salavati-Niasari, M., Mir, N., Davar, F., *J. Alloys Compd.* **493** (2010) 163.

[5] Li, F., Kong, T., Wentuan, W., Li, D., Li, Z., Huang, X., *Appl. Surf. Sci.* **255** (2009) 6285.

[6] Salavati-Niasari, M., Davar, F., Fereshteh, Z., "*J. Alloys Compd.* **494** (2010) 410.

[7] Manthiram, A., Jeong, Y.U., *J. Solid State Chem.* **147** (1999) 679.

[8] Chen, X.H., Fan, R., *Chem. Mater.* **13** (2001) 802.

[9] Fujimori, A., Mamiya, K., Mizokawa, T., Sekiguchi, T., Miyadai, T., Takahashi, H., Mori, N., Suga, S., *Physical Review B* **54** (1996) 329.

[10] Qian, X.F., Li, Y.D., Yi, X., Qian, Y.T., *Mater, Chem. Phys.* **66** (2000) 97.

[11] Rao, K.D.M., Bhuvana, T., Radha, B., Kurra, N., Vidhyadhiraja, N.S., Kulkarni, G.U., *J. Phys. Chem.* **115** (2011) 10462.

[12] An, G., Liu, C., Hou, Y., Zhang, X., Liu, Y., *Materials Letters* **62** (2008) 2643.

[13] Nadagouda, M.N., Speth, T.F., Varma, R.S., *Acc. Chem. Res.* **44** (2011) 469.

[14] Perdew, J.P., Burke, K., Ernzerhop, M., *Physical Review Letters* **77** (1990) 3865.

[15] Payne, M.C., Teter, M.P., Allan, D.C., Arias, T.A., Joannopoulos, J.D., *Reviews of Modern Physics* **64** (1992) 1045.

[16] Vanderbilt, D., *Physical Review B* **41** (1990) 7892.

[17] Monkhorst, H.J., Pack, J.D., *Physical Review B* **13** (1976) 5188.

[18] Wang, L., Zhu, Y., Li, H., Li, Q., Qian, Y., *J. Solid State Chem.* **183** (2010) 223.

[19] Denzler, D., Olschewski, M., Sattler, K., *J. Appl. Phys.* **84** (1998) 2841.

[20] Tamrakar, R., Ramrakhiani, M., Chandra, B.P., *The Open Nanoscience Journal* **2** (2008) 12.

[21] Perucchi, A., Marini, C., Valentini, M., Postorino, P., Sopracase, R., Dore, P., Hansmann, P., Jepsen, O., Sangiovanni, G., Toschi, A., Held, K., Topwal, D., Sarma, D.D., Lupi, S., *J. Phys. Rev. B* **80** (2009).

[22] Kunes, J., Baldassarre, L., Schachner, B., Rabia, K., Kuntscher, C.A., Korotin, Dm.M., Anisimov, V.I., McLeod, J.A., Kurmaev, E.Z., *J. Phys. Rev B* **81** (2010).

Chapter 4: Synthesis of hexagonal gallium nitride and hexagonal nickel sulphide nanostructures and sensing properties of their polymer composite based devices

4.0 Preamble

This chapter reports on the microwave solvothermal synthesis of GaN and hydrothermal synthesis of NiS nanostructures and their sensing properties are reported. Some of the contents of this chapter were published recently [a].

4.1 Introduction

GaN is a group (II-V) semiconductor with a wide direct band gap of 3.39 eV at room temperatures. It is a blue/green light emitter making it a candidate for applications such as in light emitting diodes, biomedicine, colour copying [1-6] etc. Numerous studies dedicated to the sensing properties of GaN for the detection of harmful gases have been reported [7-17]. Literature have shown that GaN has a good sensitivity even at room temperature and increased sensitivity towards hydrogen gas (H_2) has been achieved after palladium nanoparticle coating of a GaN surface [17]. Room temperature sensing and selectivity towards single gases are important parameters for industrial application of gas sensors. However, it is still a global challenge to obtain good and reliable nanomaterial based gas sensors with good selectivity.

NiS is one of the group (II-VI) semiconductor materials. It is a p-type semiconductor with a reported band gap of about 0.3 eV [18]. Similar to many metal

[a] Linganiso, E.C., Rodrigues, Mhlanga, S.D., Mwakikunga, B.W., Coville, N.J., Hummelgen, I.A., “GaN nanostructures-poly(vinyl alcohol) composite based hydrostatic pressure sensor device”, *Mater. Chem. Phys*. **143** (2013) 367.

chalcogenide materials, NiS has been widely studied for applications in catalysis, as a cathode material in lithium ion batteries and in IR detectors [19-121]. NiS also forms two phases viz: the rhombohedral phase (β-NiS) and the hexagonal phase (α-NiS). The α-NiS is an interesting material with a metal-to-insulator transition (MIT) occurring at 264 K [22]. This has brought much attention to NiS in regard to a number of applications making use of this MIT. MIT containing materials have been used in applications such as in ultrafast switches [23], laser protection [24] and IR detectors [25]. There is little experimental work in the literature on the application of NiS or similar alloys in gas sensing. This may be associated with its narrow band gap. However, their effect on the gas selectivity challenge encountered when using the wide band gap materials is becoming an emerging area of interest. In our group we have shown that NiS can actually sense H_2 gas with a relatively slow recovery at 300 ^oC [26]. Apart from this communication, we are one of other reports showing the use of NiS for similar applications.

Nanomaterial-polymer based composites have been of interest to many research groups in the field of science and engineering [27, 28]. Polymers offer a high surface area for nanostructures and can aid in the processing of nanomaterials. Since polymers do not affect the properties of nanomaterials, they have been applied in organic based electronic devices to overcome challenges associated with nanomaterial solubility and agglomeration [29]. Polymers are flexible, light weight and the preparation of material composites is quite cheap rendering them quite interesting for device fabrication based on nanomaterials [29]. PVA was applied in the fabrication of our devices due to its advantages such as good mechanical strength and flexibility, low conductivity and its ability to immobilize the nanostructures on the contact electrodes that were used [30, 31]. In this chapter, GaN-PVA and NiS-PVA composite based devices were prepared. Further, ethanol gas, gases evolved in the process of tomato ripening and hydrostatic pressure sensing properties were studied.

4.2 Experimental

4.2.1 Reagents and sample preparation

All reagents used were purchased from the Sigma Aldrich chemical company and were used as received without any further purification. The synthesis procedure followed is similar to the one reported in an earlier publication [a]. GaN nanostructures were synthesized using a microwave assisted solvothermal technique. In a typical reaction, an excess amount of Li_3N (99.5 %) was transferred into a Teflon vessel containing 200 mg $GaCl_3$ (99.9 %) in 30.00 ml benzyl ether solution under a nitrogen flow. The vessel was then placed in a rotor and transferred into an Anton Paar multiwave 3000 microwave reactor system, which was operated at a power of 600 W and pressure of 30 bars for 10 min. The precipitate that formed was centrifuge washed several times, and oven dried at 90°C for 6 h.

NiS nanostructures were synthesized by adding equimolar solutions of about 30 ml $Na_2S.9H_2O$ and 30 ml $NiCl_2.6H_2O$ in distilled water. The mixture was transferred to a 100 ml Teflon vessel which was placed into a Multi-wave 3000 microwave oven. The oven was operated at 600 W for 30 minutes and fan cooled to room temperature for 20 minutes. The NiS black precipitate that formed was washed several times using distilled water, ethanol and acetone and later dried in an oven at 90 ˚C for 6 hours. About 600 mg of the as-synthesized product was weighed and annealed at 300 ˚C for 3 hours under nitrogen flow (200 sccm) using a 20 ^{o}C/min heating rate in a horizontal quartz tube furnace.

4.2.2 Device preparation

Nanoparticles (NPs) of varying concentrations were dispersed in Mili-Q water using an ultra-sonicater for 10 minutes. PVA was added to each sample and the mixtures were stirred at 60 ^{o}C for 6 hours in order to completely dissolve the PVA.

The pressure sensors were prepared by depositing NP-PVA dispersions onto interdigitated electrodes. A micro-pipette was used to deposit the NP-PVA dispersion by depositing 30 μL onto an 8 X 8 mm^2 set of 20 pairs of 100 μm thick ENIG-electrodes (ENIG: Electroless Nickel Immersion Gold) separated by 100 μm from each other in an

interdigitated array onto FR4 epoxy resin/fiber board glass, supplied by Micropress SA. The deposited dispersions were allowed to dry in air over night and further dried in an oven at 100 ^{o}C for 3 hours.

The devices were electrically characterized using a programmable Agilent 4284A LCR meter with an AC signal amplitude of 500 mV as the input signal under ambient conditions. The dependence of the conductance *G* of the devices was investigated using a cylindrical tube (diameter of 44.5 mm) and a piston as previously reported [32]. The pressure was controlled by displacing the piston to modify the confined gas volume in which the sensor was placed. As a sequence of the volume change, the hydrostatic pressure was also changed following the relationship $h_0 p_0 = h_f p_f$ (*h* being the height of the piston in the cylinder, *p* is the pressure, 0 stands for initial and f stands for final).

4.3 Results and discussion

XRD data and photoluminescence spectroscopy of the as-synthesized GaN sample is shown in Fig. 4.1(a) and (b) respectively. The diffraction peaks in Fig. 4.1(a) correspond to the hexagonal wurtzite GaN phase and agrees with JCPDS data for GaN. It was noted that the (101) peak which appears at 36.84^{o} (2θ) for hexagonal GaN, does not appear in this data, and the (002) peak located at 34.58^{o} is the most intense peak. This suggests that the (002) crystalline direction was much more preferred during the growth process. The rest of the identified GaN crystalline orientations were observed in the pattern [4]. All the peaks are relatively broad which can be attributed to the small grain size of the GaN crystalline structures. The XRD profile also shows that the product contains a small amount of β-Ga_2O_3 impurity indicated by (*). The Ga_2O_3 could either be formed during the reaction (due to the presence of O_2 impurities) or more likely during product washing and storage. A very broad and intense emission covering an area from the ultra-violet to the blue region of the PL spectrum was observed for the GaN NPs [Fig. 4.1 (b)]. The peak was deconvoluted into two peaks centred at 3.15 eV and 2.95 eV. The peak centred around 3.1 eV can be attributed to a recombination of neutral donor-acceptor pairs (DAP) and their LO phonon replica and the peak centred at 3.0 eV can be attributed to a blue band (BB) [5, 6]. GaN UV emission peaks appearing

in a similar region has also been reported by Santana et al [4] for a silicon grown GaN thin film which also showed a quite similar diffraction pattern to Fig 4.1 (a). This peak was also attributed to DAP transitions from the shallow donors to the shallow acceptors [4]. The direct band gap emission common for most GaN structures is not pronounced for the as-synthesized nanoparticles.

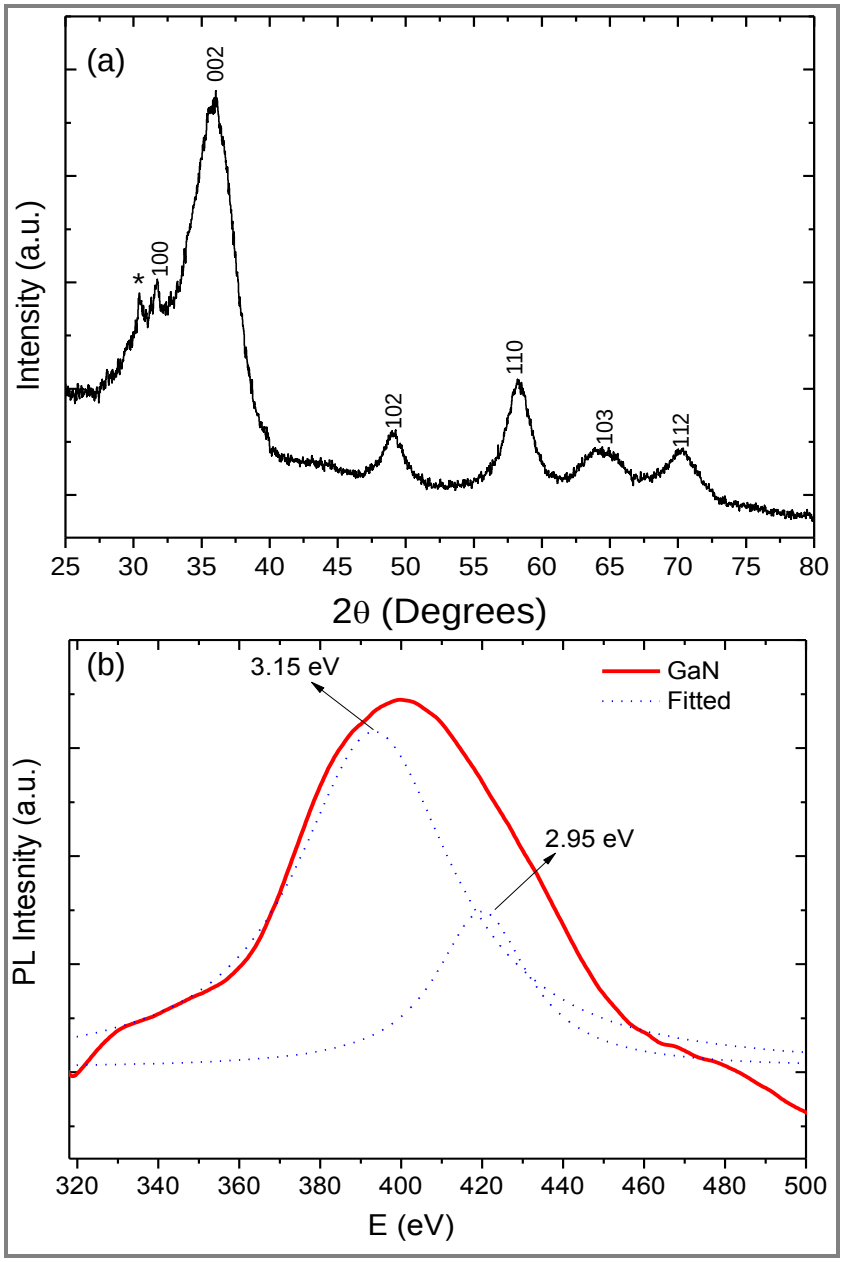


Figure 4.1: XRD patterns of the as-synthesized GaN sample corresponding to hexagonal wurtzite GaN (a) and photoluminescence spectrum of the as-synthesized GaN nanostructures excited at 300 nm (b). Symbol (*) in (a) corresponds to β-Ga2O3 impurity.

XRD data for the synthesized and annealed NiS sample is shown in Fig. 4.2. The diffraction peaks in Fig. 4.2 correspond to the hexagonal phase NiS and agrees with

database profile of α-NiS (JCPDS #: 89-7141). All peaks were indexed to a single phase showing a good crystalline nature of the sample.

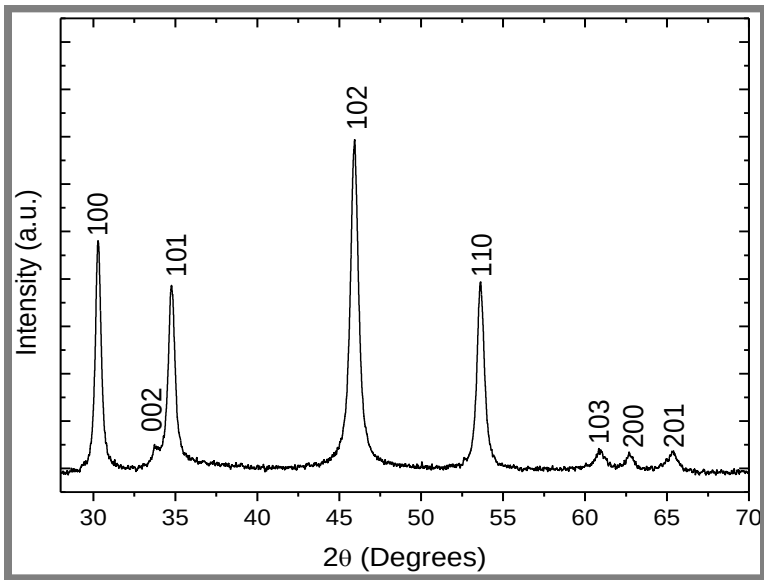


Figure 4.2: XRD data corresponding to hexagonal phase NiS (presented in more detail in chapter 5).

Figures 4.3, 4.4 and 4.5 show $\Delta G/G_0$ versus time data, for the three GaN-PVA composite based sensors (2 mg/ml. 5 mg/ml and 10 mg/ml GaN NP concentrations in 5 mg PVA). The time dependence for each sensor device is shown on the inset of the figure of each sensor device. The conductance of each sensor was observed to increase with applied pressure, and recovery was observed when the pressure was released to initial conditions. The variation in sensor sensitivity was also observed to increase slightly at lower pressures (below 150 kPa) and a drastic increase was observed at higher pressures (above 150 kPa). This shows that the sensors are more sensitive at higher pressures. The response and recovery times were measured for the three devices after applying 147 kPa. All the devices reached 90% of the maximum response in less than 11 s and 90 % of the peak signal was recovered in less than 11 s for all the devices. The devices also showed good reproducibility when measurements were taken two more times for each device.

Fig. 4.6 shows the sensitivity comparison of the devices. The three sensor devices do not show the same sensitivity. However, it can be observed that the sensitivity variation with pressure follows the same trend with all the sensors. The sensors could reach even higher sensitivities as the sensitivity curves do not reach a steady state at the highest applied pressures employed in this work. Le Boulbar *et al*. recently reported on high pressure sensitivity of a AlGaN/GaN high-electron-mobility transistor (HEMT) which sensed pressures of up to 80 bar [33]. Although their device setup is different from ours, the ability of their transistor to sense high pressures is characteristic to the AlGaN/GaN material they used.

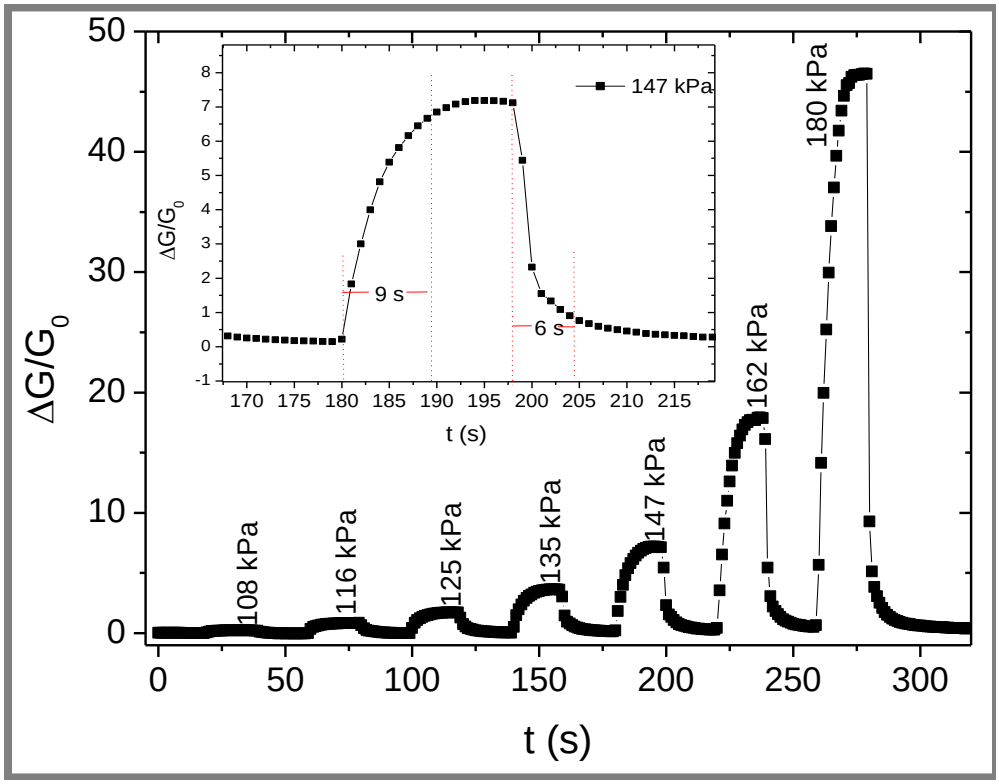


Figure 4.3: Change in conductance and capacitance of GaN(2 mg/ml)-PVA(5 mg/ml) based device as a function of applied pressure.

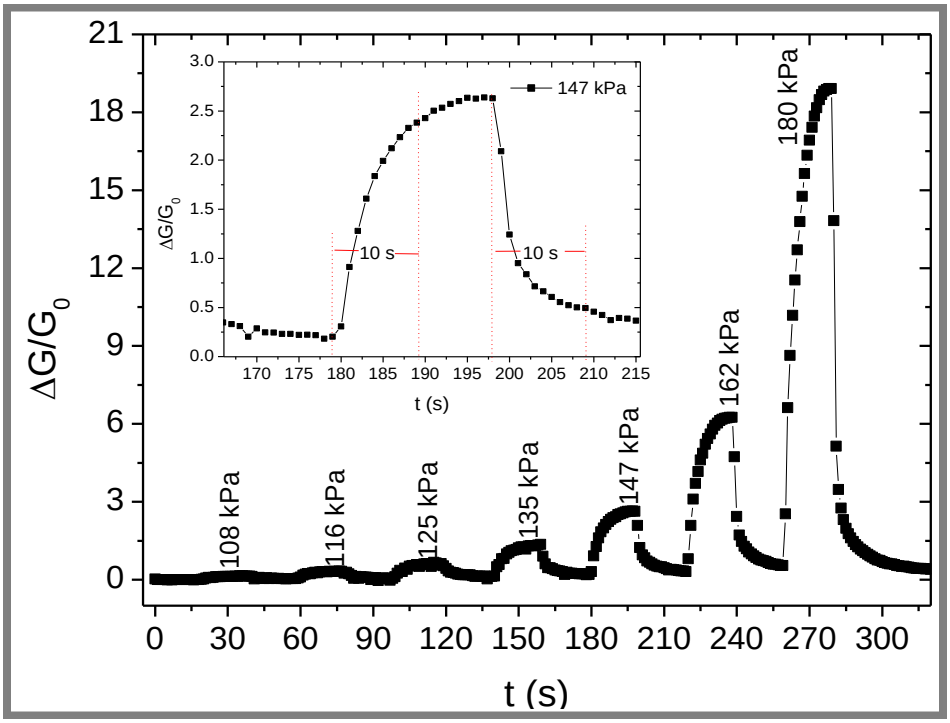


Figure 4.4: Change in conductance and capacitance of GaN(5 mg/ml)-PVA(5 mg/ml) based device as a function of applied pressure.

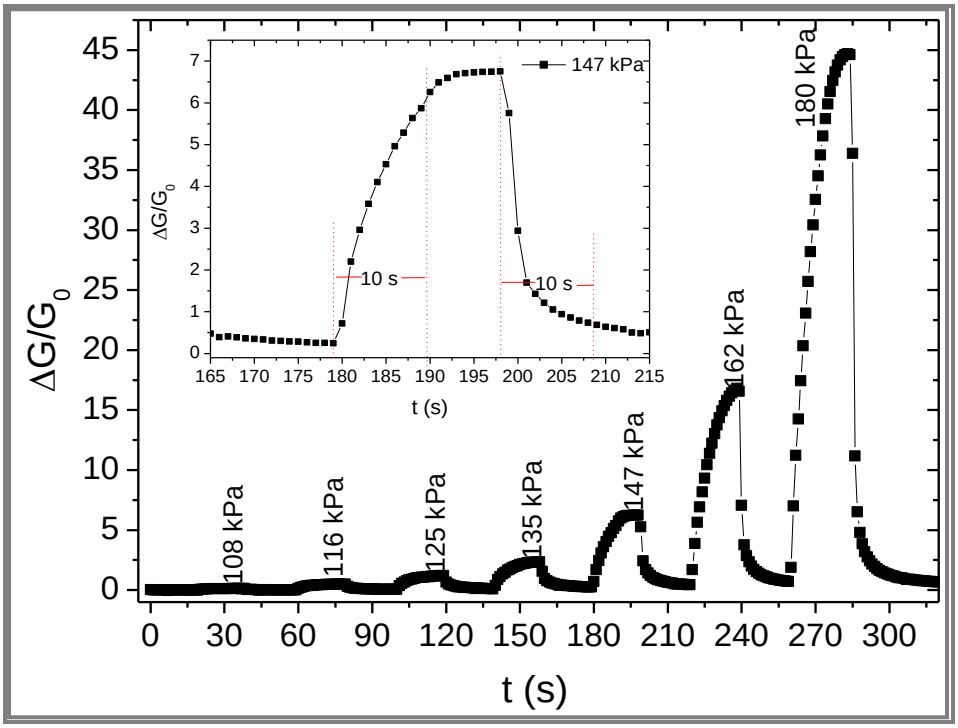


Figure 4.5: Change in conductance and capacitance of GaN(10 mg/ml)-PVA(5 mg/ml) based device as a function of applied pressure.

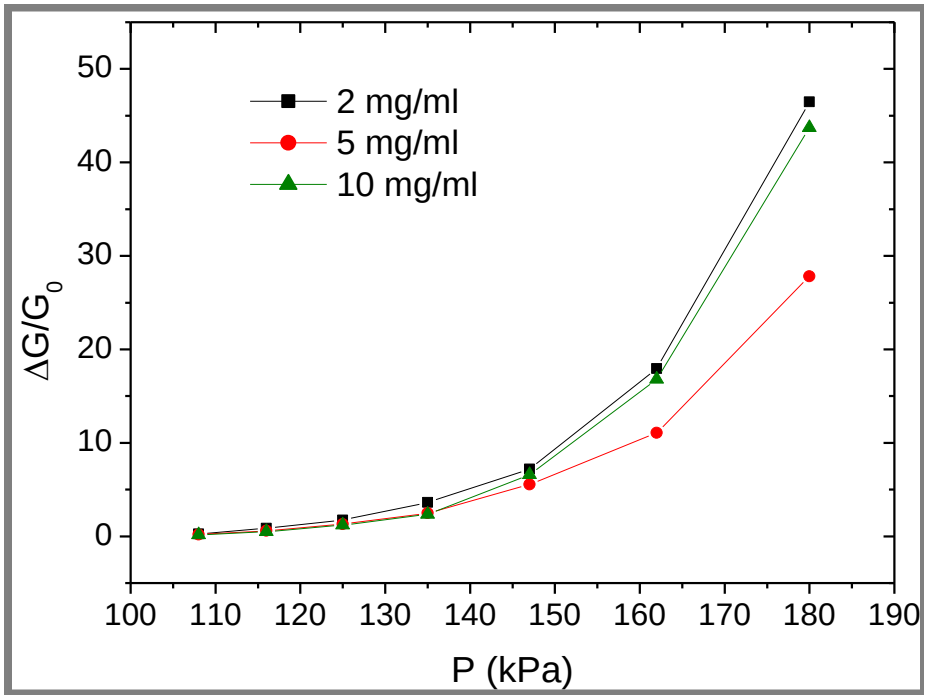


Figure 4.6: Sensitivity comparisons between the GaN/PVA composite based devices to different pressures and varying GaN concentrations.

The hydrostatic pressure sensing of the devices based on NiS-PVA composites was also investigated by measuring the change in conductance of the devices when pressure was applied as shown in Fig. 4.7. Two devices with NP concentrations; 5 mg/ml and 10 mg/ml using 20 mg PVA were applied as shown in Fig. 4.7 top left and top right respectively. The conductance variation of both devices was measured while applying pressure for 10 s and at atmospheric pressure for another 10 s consecutively for different applied pressures. An increase in conductance was observed when the applied pressure was increased, and a decrease was also observed in the absence of applied pressure. The devices also show increased response at elevated applied pressures. However, a poor recovery was obtained. The pressure response comparison graph (Fig. 4.7) shows increased conductance response with increase in NP concentration.

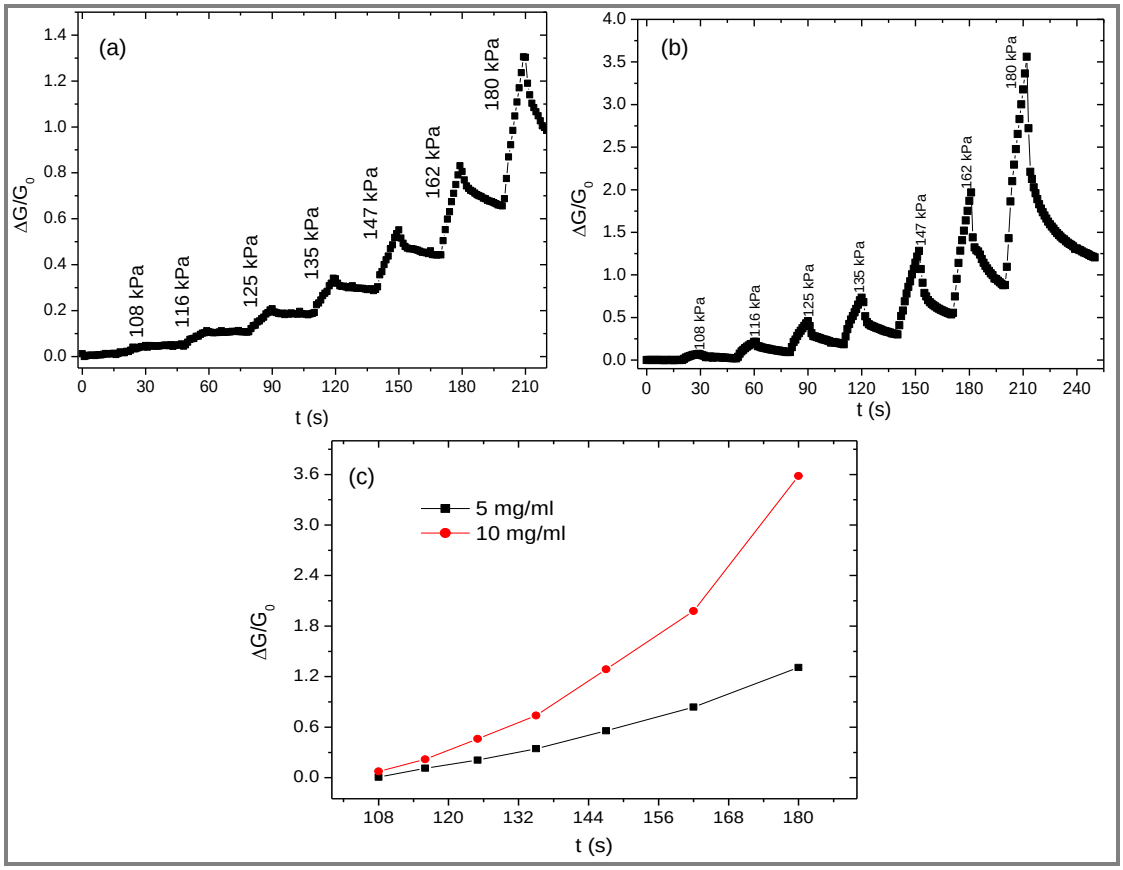


Figure 4.7: Change in conductance of α-NiS/PVA composite based devices as a function of applied pressure and NiS concentration for 5 mg/ml and 10 mg/ml concentrations in 20 mg PVA for left and right respectively. The bottom centred graph shows the difference in the sensitivities of the two samples to pressure.

Conductance measurements as a function of ethanol concentration, using the device fabricated with 5 mg/ml a-NiS and 20 mg/ml PVA, are shown in Fig. 4.8. The measurements were taken in the presence and absence of 370, 740 and 1110 ppb ethanol vapor concentrations at 90 s intervals. An increase in conductance of the device in the presence of ethanol vapor was observed, and a decrease was observed when the device was exposed to atmospheric air. The device shows relatively good response times when compared to other applied materials in the field such as carbon nanotubes and some metal oxides [34, 35]. The recovery time was also observed to be quite long as complete recovery was not reached within 90 s. The slow recovery is common for room temperature gas/vapor sensing devices due to a need for activation energy to

desorb molecules in the presence of air. The inset of Fig. 4.8 shows the ethanol response of the device when exposed to 1100 ppb ethanol concentration over a long period of time. It can be observed that the device can actually recover when given enough time in the air atmosphere. The α-NiS nanostructures could be modified by doping or metal catalyst decoration in order to quicken its response and recovery times.

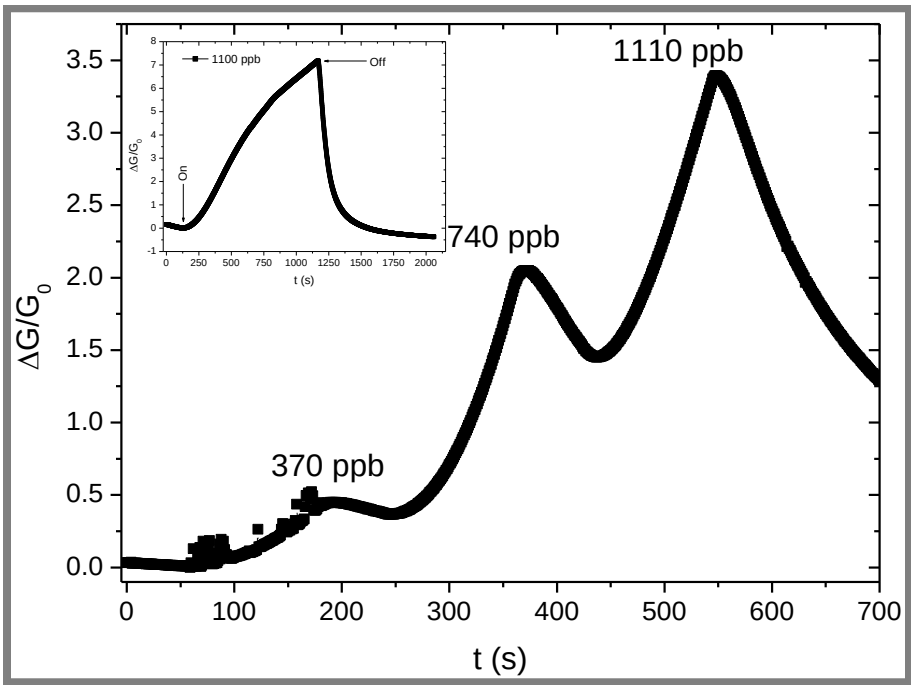


Figure 4.8: Change in conductance of the α-NiS-PVA composite based device in the presence and absence of ethanol vapor with different concentrations.

The mechanism for ethanol sensing on the surface of the NiS material is mainly controlled by the amount of oxygen ions adsorbed on the surface of NiS due to the exposure of the material to air. In this process, the adsorbed oxygen molecules form an oxygen ion by capturing an electron from the conduction band resulting in a formation of a depletion layer on the surface regions. At low temperatures, the adsorbed oxygen species ionises according to equations 1 and 2 [36-38]. When the sensor is exposed to a reducing gas (ethanol) at room temperatures, ethanol reacts with the surface adsorbed oxygen species on the surface of NiS material to give CO_2 and H_2O and release the trapped electrons back to the conduction band, which results in an increase

in conductivity of the sensor [38]. The overall equation for ethanol gas sensing at room temperatures is given in equation 3.

$$O_{2(gas)} \leftrightarrow O_{2(ads)} \quad (1)$$

$$O_{2(ads)} + e^- \leftrightarrow O^-_{2(ads)} \quad (2)$$

$$CH_3CH_2OH + 3O^-_2 \leftrightarrow 2CO_2 + 3H_2O + 3e^- \quad (3)$$

Normally, a series of experiments are done for fruits such as tomato at different maturity stages in order to evaluate fruit quality and maintain fruit flavor until consumption. The tomato volatiles during ripening are derived from lipids via oxidation when cells are disrupted [39]. Other volatiles are contributed by carotenoids, amino acids and terpenoids [39, 40]. The electronic nose system (E-nose) is currently being explored as an alternative way to study fruit maturity stages and to avoid the gas chromatography based techniques. Although E-nose cannot identify (or separate) different chemical compounds, high sensitivity, cost effectiveness, and relatively fast analysis are some of its advantages [41]. In this study, only one stage tomato sample was used to evaluate the sensor devices response. The tomato was randomly picked from a supermarket.

In Fig. 4.9 (a), (b) and (c), the change in conductance of the devices based on the composites; α-NiS (5 mg/ml)-PVA (20 mg/ml), α-NiS (10 mg/ml)-PVA (20 mg/ml), and GaN (10 mg/ml)-PVA (5 mg/ml) was investigated in the presence of tomato volatiles and atmospheric air as a function of frequency (Hz). All the devices showed an increasing conductance with exposure to tomato volatiles and recovery was observed when the devices were exposed to the air atmosphere. Although a small variation was observed in the response intensities for the device [NiS (5 mg/ml)-PVA (20 mg/ml] as a function of frequency, a decrease in respense intensity was observed for the other devices as the frequency was increased from 27 khz to 460 kHz. Slow recovery of the peak intensity was observed when the α-NiS based devices were exposed to air. The GaN based devise showed a relatively fast recovery although the device could not reach saturation after the exposure to tomato atmosphere for about 120 s. This can be atytributed to a very high sensitivity of GaN nanomaterials, while the surface-volatile interaction could be delayed due to nanoparticle packing as well as the PVA effect.

Further studies would require long term studies of the tomato ripening process in order to obtain a signature that can be correlated to the fruit maturity stage.

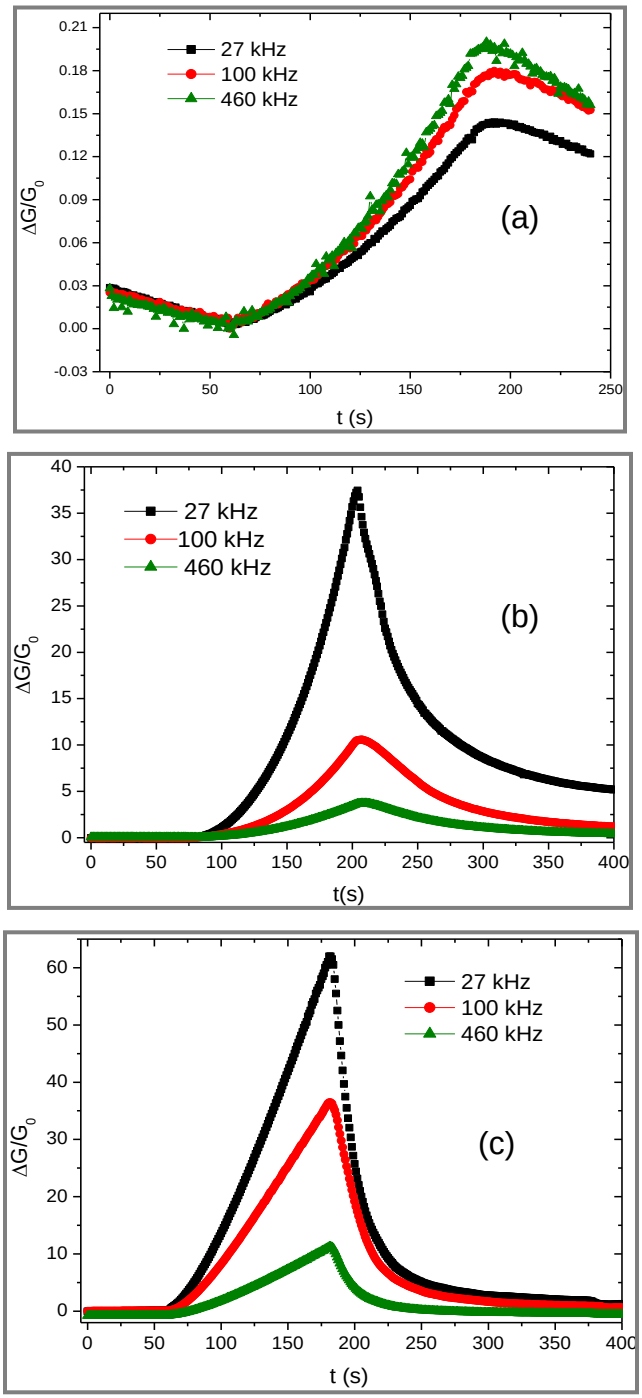


Figure 4.9: Change in conductance and capacitance of (300 ^{o}C annealed) α-NiS (5 mg/ml)-PVA(20 mg/ml) based device in the presence of tomato fruit volatiles (a). Change in conductance and capacitance of α-NiS (10 mg/ml)-PVA (20 mg/ml) based device in the presence of tomato fruit volatiles (b). Change in conductance and capacitance of GaN (10 mg/ml)-PVA (5 mg/ml) based device in the presence of tomato fruit volatiles (c).

4.4 Conclusions

In summary, UV-blue emitting hexagonal GaN nanostructures and hexagonal NiS were fabricated using microwave-assisted solvothermal and hydrothermal techniques respectively. The as-synthesized materials were successfully mounted into devices in a NP-polymer composite form and tested for pressure sensing, ethanol vapor sensing and sensing of organic volatile compounds mixture from tomato. A high sensitivity of GaN based device to applied hydristatic pressure was realised for the different concentrations of a GaN-NPs used. All devices showed a relatively fast response and recovery times of less than 11 s. The GaN based device also showed a good response to the organic volatile compounds mixture from tomato while the NiS based device showed a relatively good response to ethanol vapor.

4.5 References

[1] Lv, W., Wu, L., Wu, Y., Xv, R., Gai, H., Zou, K. *J. Cryst. Growth* **307** (2007) 1.

[2] Okumura, H., Ohta, K., Feuillet, G., Balakrishnan, K., Chichibu, S., Hamaguchi, H., Hacke, P., Yoshida, S., *J. Cryst. Growth* **178** (1997) 113.

[3] Chen, X.J., Gayral, B., Sam-Giao, D., Bougerol, C., Durand, C., Eymery, J., *Appl. Phys. Lett.* **99** (2011) 251910.

[4] Santana, G., De Melo, O., Aguilar-Hernandez, J., Mendoza-Perez, R., Monroy, B.M., Escamilla-Esquivel, A., Lopez-Lopez, M., De Moure, F., Hernandez, L.A., Contreras-Puente G., *Materials* **6** (2013) 1050.

[5] Sahoo, P., Dhara, S., Amirthapandian, S., Kamruddin, M., Dash, S., Panigrahi, B.K., Tyagi, A.K., *Cryst. Growth Des.* **12** (2012) 2375.

[6] Sahoo P., Oliveira, D.S., Cotta, M.A., Dhara, S., Dash, S., Tyagi, A.K., Raj, B., *J. Phys. Chem. C* **115** (2011) 5863.

[7] Chitara, B., Late, D.J., Krupanidhi, S.B., Rao, C.N.R., *Solid State Communications* **150** (2010) 2053.

[8] Sahoo, P., Dhara, S., Dash, S., Amirthapandian, S., Prasad A.K., Tyagi, A.K., *Int. J. Hydrogen Energy* **38** (2013) 3513.

[9] Abdullah, Q.N., Yam, F.K., Hassan, J.J., Chin, C.W., Hassan, Z., Bououdina, M., *Int. J. Hydrogen Energy* **38** (2013)14085.

[10] Chen, T.-Y., Chen, H.-I., Liu, Y.-J., Huang, C.-C., Hsu, C.-S., Chang, C.-F., Liu, W.-C., *Sensors and Actuators B* **155** (2011) 347.

[11] Bajpai, R., Motayed, A., Davydov, A.V., Oleshko, V.P., Aluri, G.S., Bertness, K.A., Rao, M.V., Zaghloul, M.E., *Sensors and Actuators B: Chemical* 171 (2012) 499.

[12] Ramizy, A., Hassan, Z., Omar, K., *Sensors and Actuators B: Chemical* 155 (2011) 699.

[13] Wang, X.H., Wang, X.L., Feng, C., Yang, C.B., Wang, B.Z., Ran, J.X., Xiao, H.L., Wang, C.M., Wang, J.X., *Microelectronics Journal* **39** (2008) 20.

[14] Johnson, J.L., Choi, Y., Ural, A., Lim, W., Wright, J.S., Gila, B.P., Ren, F., Pearton, S.J., *J. Electronic Materials* **38** (2009) 490.

[15] Shah, A.Z., Noor, N.H.M., Hassan, Z., Mahmood, A., Kwong, Y.F., *Malaysian Journal of Fundamental & Applied Science* **8** (2012) 49.

[16] Chen, Y., Jang, S.-D., Kim, J., *Sensor Letters* **10** (2012) 748.

[17] Kim, S.S., Park, J.Y., Choi, S.-W., Kim, H.S., Na, H.G., Yang, J.C., Lee, C., Kim, H.W., *Int. J. Hydrogen Energy* **36** (2001) 2313.

[18] O'Brien, P., Waters, J., *Chem. Vap. Deposition* **12** (2006) 9620.

[19] Zhou, H., Lv, B., Wu, D., Sun, Y., *Particuology* **10** (2012) 783.

[20] Wang, J., Chew, S.Y., Wexler, D., Wang, G.X., Ng, S.H., Zhong, S., Liu, H.K., *Electrochem. Commun.* **9** (2007) 1877.

[21] Tang, C., Zang, C., Su, J., Zhang, D., Li, G., Zhang, Y., Yu, K., *Appl. Surf. Sci.* **257** (2011) 3388.

[22] Fujimori, A., Namatame, H., Matoba, M., Anzai, S*., Physical Review B* **42** (1990) 620.

[23] Petrov, G.I., Yakovlev, V.V., Squier, *J., Appl. Phys. Lett.* **81** (2002) 1023.

[24] Vernardou, D, Pemble, M.E., Sheel, D.W., *Surf. Coat. Technol.* **188-189** (2004) 250.

[25] Pan, M., Liu, J., Zhong, H., Wang, S., Li, Z.-F., Chen, X., Lu, W., *J. Cryst. Growth* **268** (2004) 178.

[26] Linganiso, E.C., Mwakikunga, B.W., Mhlanga, S.D., Coville, N.J., Sone, B.T., Maaza, M., *Proceedings of the IEEE Sensors 2012 Conference*, Taipei, Taiwan, October, (2012).

[27] Wang, C., Guo, Z.-X., Fu, S., Wu, W., Zhu, D., *Progress in Polymer Science* **29** (2004) 1079.

[28] El-Mansy, M.K., Sheha, E.M., Patel, K.R., Sharma, G.D., *Optik* **124** (2013) 1624.

[29] Bell, J.M., Goh, R.G.S., Waclawik, E.R., Giulianini, M., Motta, N., *Materials Forum* **32** (2008) 144

[30] Lindsey, S.E., Street G.B., *Synthetic Metals* **10** (1984) 67.

[31] Zhao, X., Zhang, Q., Chen, D., Lu, P., *Macromolecules* **43** (2010) 2357.

[32] Machado, W.S., Athayde, P.L., Mamo, M.A., van Otterlo, W.A.L., Coville, N.J., Hummelgen, I.A., *Org. Electron.* **11** (2010) 1736.

[33] Le Boulbar, E.D., Edwards, M.J., Vittoz, S., Vanko, G., Brinkfeldt, K., Rufer, L., Johander, P., Lalinsky, T., Bowen, C.R., Allsopp, D.W.E., *Sensors and Actuators A:* Physical **194** (2013) 247.

[34] Liu, C.-K., Huang, M. –W., Wu, J. –M., Shih, H. C., *Diamond & Related Materials* **19** (2010) 981.

[35] Rajesh, N., Kannan, J.C., Krishnakuma, T., Leonardi, S.G., Neri, G., *Sensors and Actuators B* **194** (2014) 96.

[36] Santra, S., Guha, P.K., Ali, S.Z., Hiralal, P., Unalan, H.E., Covington, J.A., Amaratunga, G.A.J., Milne, W.I., Gardner, J.W., Udrea, F., *Sensors and Actuators B* **146** (2010) 559.

[37] Ramgir, N.S., Haur, M., Sharma, P.K., Datta, N., Kailasaganapathi, S., Bhattacharya, S., Debnath, A.K., Aswal, D.K., Gupta, S.K., *Sensors and Actuators B* **187** (2013) 313.

[38] Gu, F., Zhang, L., Wang, Z., Han, D., Guo, G., *Sensors and Actuators B* **193** (2014) 669.

[39] Berna, A.Z., Lammertyn, J., Saevels, S., Natale, C.D., Nicolai, B.M., *Sensors and Actuators B* **97** (2004) 324.

[40] Farneti, B., Cristescu, S.M., Costa, G., Harren, F.J.M., Woltering, E.J., *J Food Sci.* (2012) C1.

[41] Peris, M., Escuder-Gilabert, L., *Analytica Chimica Acta* **638** (2009) 1.

Chapter 5: Effect of NaOH and precursor on the nickel monosulphide phase

5.0 Preamble

This chapter reports on the synthesis of binary phase nickel monosulphide. Water and NaOH were applied as solvents for the microwave-assisted hydrothermal synthesis of NiS. The effect of NaOH concentration, precursor concentration and reaction time were investigated.

5.1 Introduction

Metal chalcogenide nanomaterials (e.g. CdS, ZnO, ZnS, SnO, SnS, CoS, CuS, NiS etc.) have been a topic of interest over the years owing to their novel properties resulting from the quantum confinement effect shown by these materials [1-5]. Nanomaterials have remarkable electronic, mechanical and chemical and other properties and this has resulted in intensive investigations to find new applications for these materials. In particular, NiS nano-materials have been widely researched for potential applications in catalysis, rechargeable batteries, hydrogen storage devices, optoelectronic devices and magneto-electronic devices [6-9]. These materials are relatively cheap to make with most fabrication reactions occurring at temperatures below 473 K and H_2O being used as a solvent [10-12].

Chemical methods that have been used to synthesize NiS include the conventional reflux method [13], chemical bath deposition method [14], successive ionic layer adsorption and reaction (SILAR) method [15], hydrothermal method [16, 17], etc. Reaction parameters such as temperature, pressure, reaction time, type of solvent, precursor source, concentration of reagents and the solubility of precipitate at precipitation, play a huge role in the morphology distribution of the products, as well as the type of crystal structure obtained from a given reaction [18, 19].

To further explore methods to make NiS phases a microwave-assisted hydrothermal technique was chosen to make these nanostructures of NiS due to the advantages of the microwave synthesis technique over conventional hydrothermal techniques. Microwaves provide for homogenous heating throughout the reaction vessels, which provide a uniform nucleation environment and thus promote uniformity of the product produced. As outlined in the literature review chapter, the NiS nanomaterial synthesis has not been explored much, by the microwave synthesis method.

In this work we show the effect of NaOH concentration, reaction holding time, the S source and the precursor concentration on the final product. The microwave assisted hydrothermal method was employed to synthesize binary phase NiS nanostructures with varying morphologies and phase distributions.

5.2 Experimental

5.2.1 Reagents and sample preparation

All reagents were purchased from the Sigma Aldrich chemical company, SA, and were used as received without any further purification. NiS nanostructures were synthesized by adding equimolar solutions of S (with excess of 0.002 M per reaction) and Ni sources using distilled water (H_2O) or sodium hydroxide (NaOH) as a solvent. The precursor mixture was transferred to a 100 ml Teflon vessel which was placed into a Multi-wave 3000 microwave oven from Anton Paar. The oven was operated at 600 W for 15, 25 or 30 minutes and fan cooled to room temperature for 20 minutes. The pressure maximum was set at 40 bars. A black precipitate of NiS material was obtained and washed with distilled water, ethanol and acetone to remove impurities. All the products were dried in an oven at 90 ^{o}C for 6 h. The different parameters employed for the reactions carried out are shown in Table 5.1.

5.2.2 Characterization

The structural analyses was performed using a Panalytical X'Pert PRO PW 3040/60 X-ray diffractometer with a Cu Kα (λ = 0.154 nm) monochromated radiation source. XRD spectra were collected in θ-2θ scan (10-90˚) with a measurement step of 0.02˚. The crystallite size for all the samples was estimated using the Scherrer equation given in Equation 1,

$$D = \frac{K\lambda}{\beta \cos\theta} \qquad (1)$$

where D is the average dimension of the crystallites, K is a constant (usually applied as 0.9), λ (0.154 nm) is the wavelength of the Cu$K\alpha_1$ X-ray, β is the full width at half maximum of the diffraction peak (inaccuracies associated with stress and instrumental broadening are expected), and θ is the Bragg angle.
The surface morphology was determined from high resolution-transmission electron microscopy images (JEOL HR-TEM -2100) and scanning electron microscopy (Carl-Zeiss SEM).

Table 5.1: The different parameters used for each reaction carried out.

Precursors	Ni precursor Concentration (M)	Reaction time (min)	[NaOH] (M)
$NiCl_2.6H_2O + CS(NH_2)_2$	0.13	15	5
$NiCl_2.6H_2O + CS(NH_2)_2$	0.13	25	5
$NiCl_2.6H_2O + CS(NH_2)_2$	0.13	35	5
$NiCl_2.6H_2O + CS(NH_2)_2$	0.13	15	3
$NiCl_2.6H_2O + CS(NH_2)_2$	0.13	15	5
$NiCl_2.6H_2O + CS(NH_2)_2$	0.13	15	7
$NiCl_2.6H_2O + Na_2S.9H_2O$	0.13	15	0
$NiCl_2.6H_2O + Na_2S.9H_2O$	0.13	15	5
$NiCl_2.6H_2O + S$	0.13	15	5
$NiCl_2.6H_2O + CS(NH_2)_2$	0.13	15	5
$Ni(CH_3COO)_2.4H_2O + Na_2S.9H_2O$	0.03	15	0
$Ni(CH_3COO)_2.4H_2O + Na_2S.9H_2O$	0.04	15	0
$Ni(CH_3COO)_2.4H_2O + Na_2S.9H_2O$	0.06	15	0
$Ni(CH_3COO)_2.4H_2O + Na_2S.9H_2O$	0.07	15	0
$Ni(CH_3COO)_2.4H_2O + Na_2S.9H_2O$	0.08	15	0
$Ni(CH_3COO)_2.4H_2O + Na_2S.9H_2O$	0.11	15	0

5.3 Results and discussion

5.3.1 Reaction holding time effect: phase and morphology analysis

X-ray analysis performed on the samples synthesized from $NiCl_2.6H_2O$ and $CS(NH_2)_2$ using 5 M NaOH and different reaction times (15, 25 and 35 minutes) confirmed that the binary phases, α- and β-NiS, were formed. It was observed in Fig. 5.1 that the XRD peaks shift towards the lower angles as the reaction holding time was increased from 15 min to 35 min. Crystallite sizes estimated by Scherrer equation for the peaks centred at

48.9^{o} and 46^{o} for β-NiS and α-NiS respectively, were calculated for the different reaction times used and are shown in Table 5.2. It was observed that the average crystallite sizes increase with increase in holding time which can be attributed to sintering effect. The XRD profile also confirmed that when the holding time was increased, the rhombohedral phase NiS was dominant, while the hexagonal phase was reduced in content with holding time. It is also worth noting that the peak due to the presence of $Ni(OH)_2$ located around 38^{o}, is present in all the samples. This suggest insufficient S^{2-} ions in solution which leave some of the intermediate $Ni(OH)_2$ phase present after the reaction between Ni^{2+} and S^{2-} ions. It is shown in the next chapter that this $Ni(OH)_2$ peak disappeared after annealing the samples at 300 ^{o}C for 3 h or more, leaving a highly crystalline product with a slightly different (S deficient) Ni:S stoichiometry.

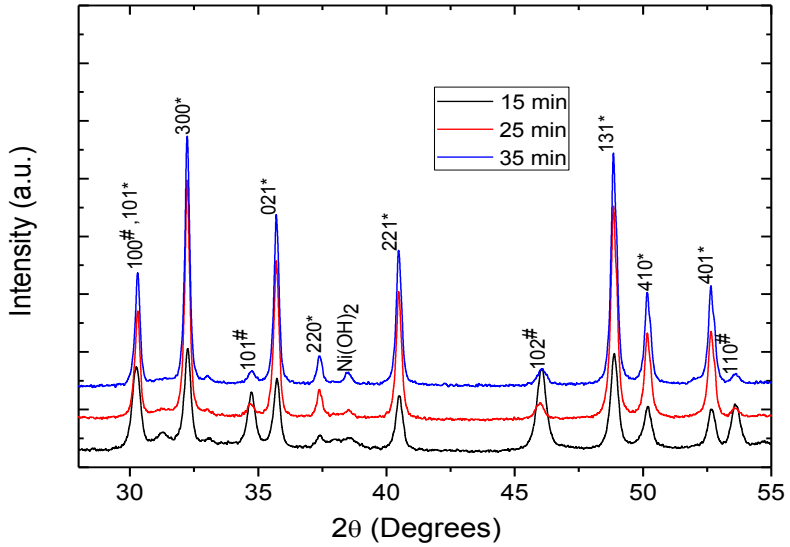


Figure 5.1: XRD patterns showing NiS samples synthesized at different times. The symbol ($^{\#}$) represent the α-NiS phase and the symbol (*) represents the β-NiS phase.

Table 5.2: Peak shift and estimated crystallite size for 131 orientations for β-NiS phase.

NiS phase	Reaction time (min)	Peak orientation α (#), β(*)	Peak position [2θ (°)]	Estimated crystallite size (nm)
β	15	131*	48.88	61
	25		48.86	73
	35		48.85	76
α	15	102#	46.06	19
	25		45.97	22
	35		46.06	21

TEM analysis showed that the product consisted of nanorods and a few smaller irregular shaped particles. The diameter of the rods was observed to increase in size as the holding time was increased [Fig. 5.2]. When the holding time was increased to 35 minutes, the rods agglomerated to form flower-like structures. The synthesis of flower-like structures is common for metal chalcogenide nanostructures. Also, the use of a strong base as a solvent has been shown to favour the formation of nanostructure-based flower-like structures [20]. Wahab et al. [20] reported on the growth mechanism of ZnO nanostructures synthesized in the presence of NaOH and they studied the effect of pH on the product morphology. They attributed the formation of nanoflowers at pH 12 to uncontrollable and unselective hydrolysis or condensation which generates large interconnected particles/structures [20]. In our case reaction holding time was varied in the presence of NaOH. It is clear that as the reaction continues, the particles grow bigger and after a longer reaction holding time is employed, the structures become attached to one another. Chen et al. reported a growth mechanism of β-NiS from thiourea and $NiCl_2$ using ethylenediamine as a solvent in an autoclave reactor. They attributed the formation of similar types of flowers to a slow S substitution in spherical groups of Ni-thiourea complexes with further growth adding to the [001] direction to form rod-like structures from the core [21]. Contrary to their finding, our image analysis shows that both particles and rods are both present at short times and they agglomerate

with the diameter of the rods also increasing in length. However, the mechanism explained by Chen could also be applicable in our case, with the particles observed due to reaction termination during the early stages of formation. This however, would suggest that the energy distribution inside the microwave reactor is not very uniform.

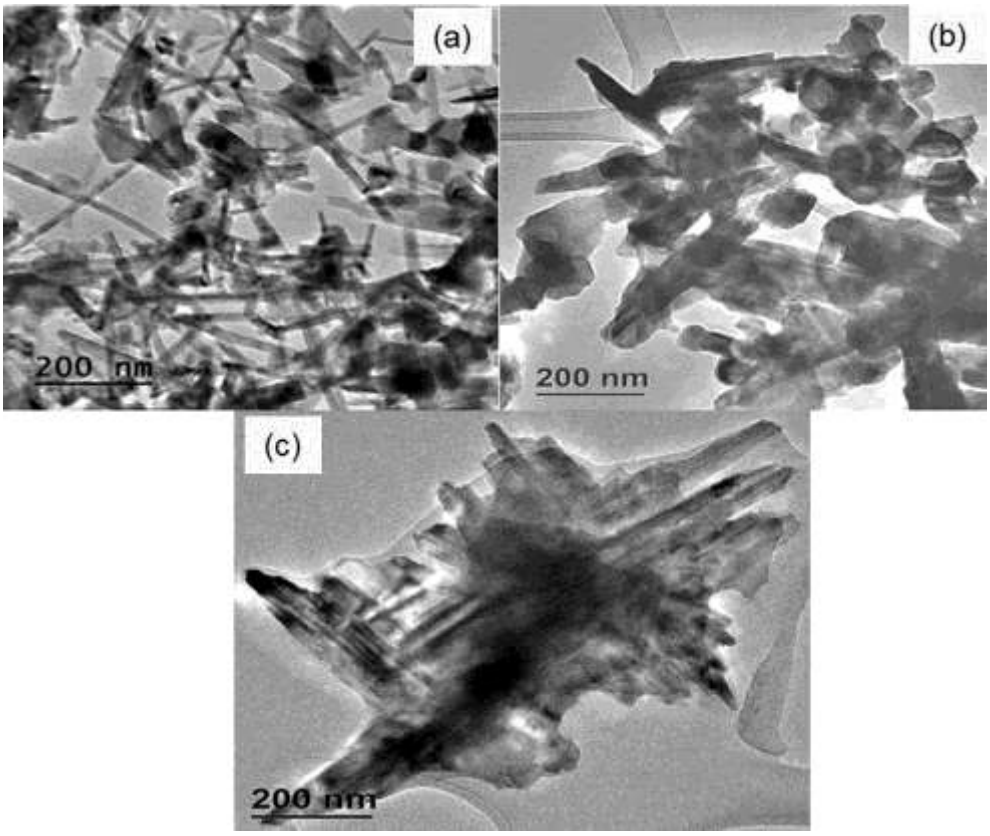


Figure 5.2: TEM images of NiS samples synthesized at different (a) 15 min, (b) 25 min, and (c) 35 min.

In our case, it is possible to explain the growth mechanism of the nanorod-based flower-like structures, as promoted by the agglomeration of both nanoparticles and nanorods with simultaneous increase in the diameter of the rods. Because of the length difference of the rods coming together, breakage of longer rods during merging is likely to occur, resulting in a rod length determined by the shorter merging nanorod. There is a possibility that these particles are associated with the α-NiS phase while the rods are due to the β-NiS phase. Cheng et al. also reported on an increasing β-NiS at the

expense of α-NiS phase after reaction completion due to thermodynamic stability of the β-NiS phase [21].

5.3.2 NaOH concentration effect: phase and morphology analysis

X-ray analysis performed on the samples synthesized from $NiCl_2.6H_2O$ and $CS(NH_2)_2$ using 15 min reaction time and varying the NaOH concentration (3, 5 and 7 M), confirmed that binary phase, α- and β-NiS phases were both formed. It can be seen in Fig. 5.3 and Table 5.3 that the XRD peaks shift towards the lower angles as the solvent concentration is increased from 3M to 7M. This can be associated with increasing crystallinity of the products as a function of solvent concentration. An increase in the α-NiS phase as the NaOH concentration is increased was observed (peak orientation [102]), and a decrease in relative β-NiS peak intensities was also observed when the NaOH concentration was increased over similar reaction times (peak orientation [220]). Peak ratios (β/α) for peak orientations [131]/[102] were calculated to be 1.81, 1.10, and 0.66 for 3 M, 5 M, and 7 M respectively. The β-NiS phase is thermodynamically more stable than α-NiS and it has been reported to have a higher solubility constant when compared to α-NiS [11, 22]. The increasing relative intensity of α-NiS can be attributed to the precipitation of α-NiS occurring first, due to its lower solubility constant, which was observed to transform to β-NiS when reaction time is increased. It can also be noted that the relative intensity of the $Ni(OH)_2$ peak increases with increased NaOH concentration. This may be attributed to less S^{2-} ions available and the increasing concentration of OH^- ions as NaOH concentration is increased.

Microwave hydrothermal synthesis of binary phase α-,β-NiS has been reported by Idris et al. [23]. In their study, they observed increasing β-NiS phase in the expense of α-NiS with increased temperature. This was accompanied by appearance of needle-like structures at higher temperatures compared to the irregular shaped particles they observed at lower temperatures [23].

Table 5.3: Variation of the estimated crystallite size of the samples synthesized using different NaOH concentrations.

NiS phase	NaOH concentration (M)	Peak orientation α (#), β(*)	Peak position [2θ (°)]	Estimated crystallite size (nm)
β	3	300*	32.27	40
	5		32.25	31
	7		32.21	36
α	3	102#	46.13	23
	5		46.05	21
	7		45.81	26

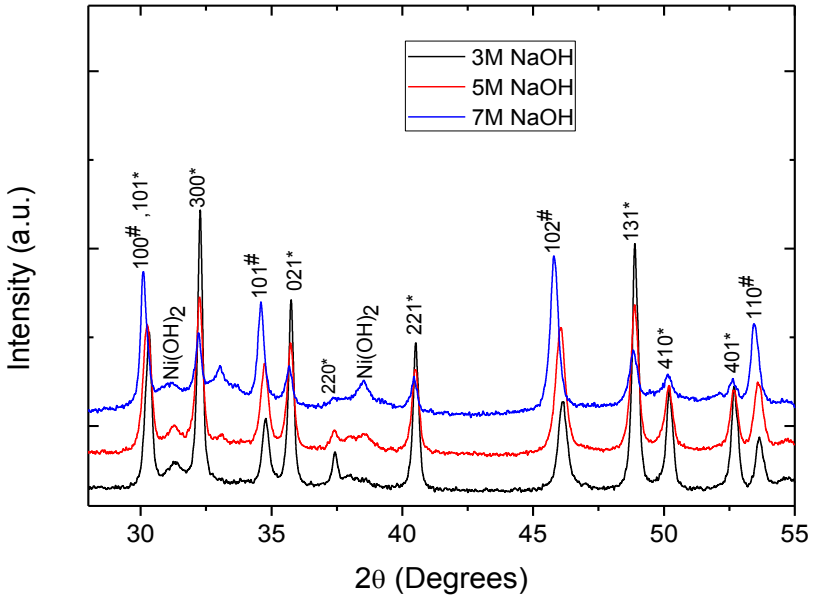


Figure 5.3: XRD patterns showing NiS products synthesized at different NaOH concentrations. Symbol (*) represent β-NiS while symbol (#) represents α-NiS phase.

SEM and TEM analysis for the products showed that they consisted of structures varying from a mixture of particles and rods at lower NaOH concentrations, with nanorods dominating at 5 M NaOH concentration and rod-based flower-like structures

at 7M NaOH. The diameter of the rods was observed to increase in size as the concentration increased [Fig. 5.4]. Unlike the flowers observed when time was varied in Fig 5.2, the flowers observed when 7 M NaOH was used appear to have relatively dense centers in the TEM image. The insets on Fig 5.4 bottom SEM image are cropped images showing the appearance of hexagonal platelets at the centres of the flower-like structures. This of cause was not observed for all the flower-like structures, but it was dominant in most of the TEM images. This was evidenced by the lower number of particles in β-NiS phase dominated sample while more particles were observed for the sample with relatively high α-NiS content in Fig 5.1 and Fig 5.2. The hexagonal platelets are more likely to be the hexagonal phase structures while the rods are more likely to be the rhombohedral phase. Assuming this is the case, we can predict the growth mechanism of the flowers. While both α-NiS and β-NiS are present in solution, the rods are drawn to the different sides of the hexagonal platelets.

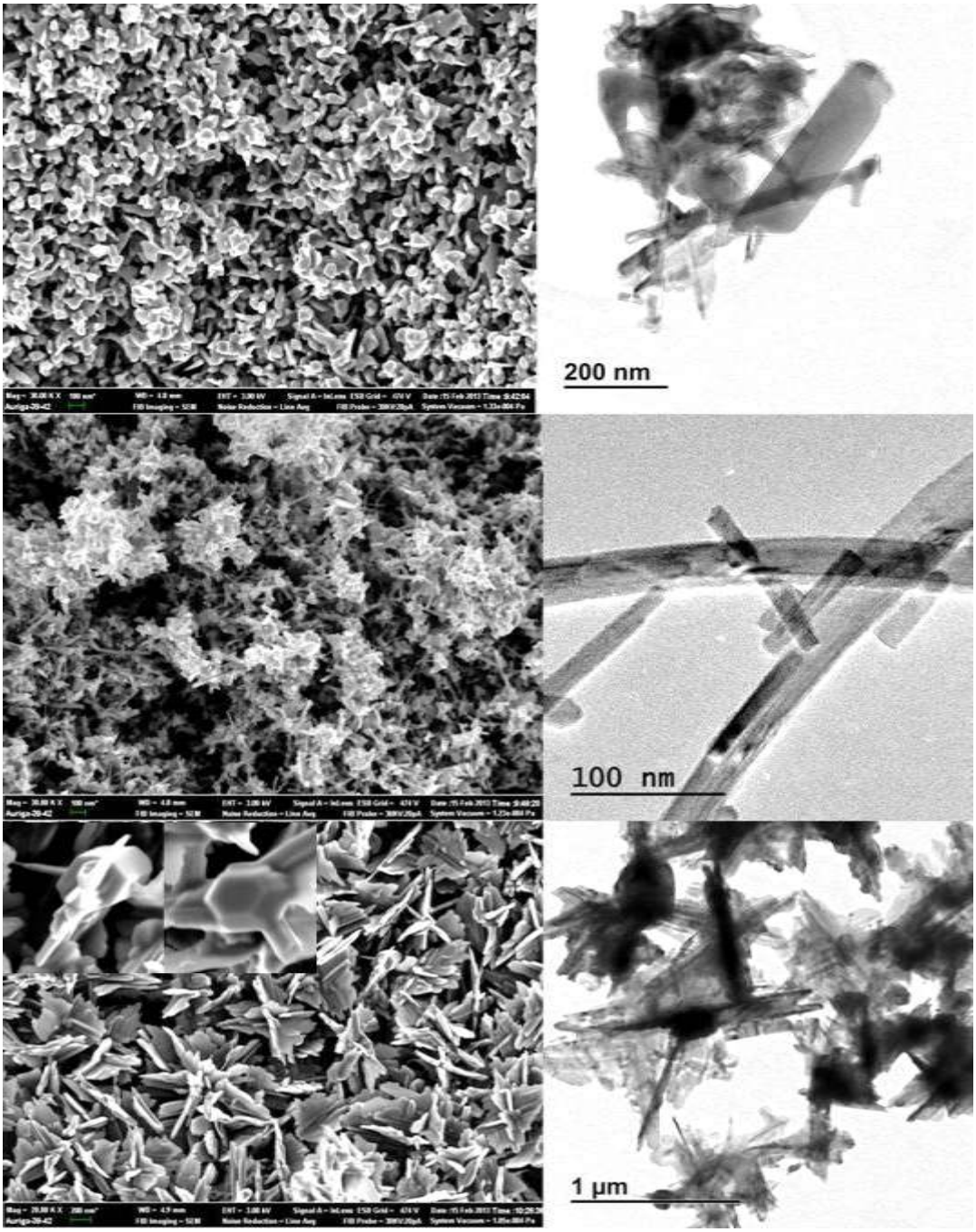


Figure 5.4: SEM (left) and TEM (right) images of NiS synthesized with different NaOH concentrations 3M, 5M and 7M from top to bottom respectively. The two insets on the 7M SEM image (bottom) show hexagonal platelets at the centre of the flowers.

The platelets later dissolve and form part of the β-NiS phase (when given enough reaction times). Due to short reaction time employed in this case, the hexagonal platelets were not yet dissolved into the flower-like structure in Fig. 5.4 bottom image. Fig.5.5 shows the proposed growth mechanism of the flower-like NiS structures. The NaOH concentration clearly plays a role in the formation of the flower-like structures. This can be attributed to the increased concentration of OH^- ions in solution, which form $Ni(OH)_2$. The $Ni(OH)_2$ has been shown to favour layer-like structures, and the flower fashion of the product may be influenced by this [24]. Further, the increasing amount of α-NiS as a function of NaOH concentration may be another indication that the α-NiS first forms and later converts to β-NiS phase.

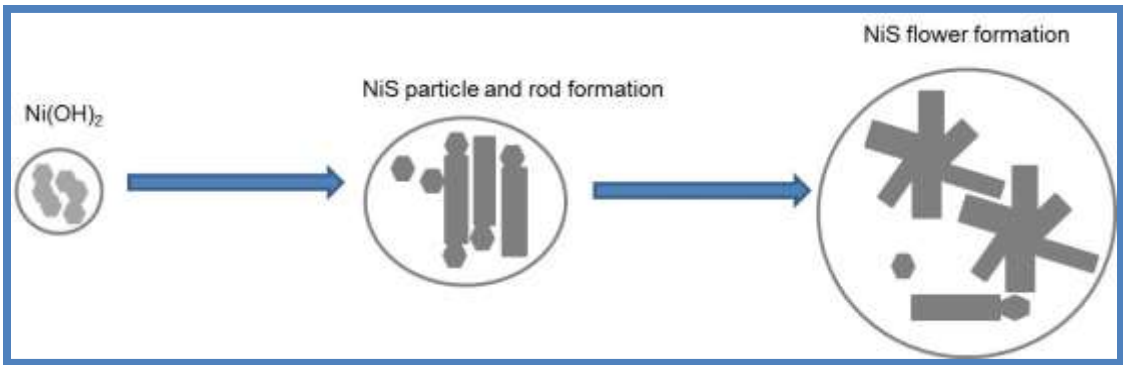


Figure 5.5: Proposed growth mechanism for the binary phase NiS, from particles and rods to flower-like structures.

5.3.3 Precursor effect: phase and morphology analysis

X-ray analysis of samples synthesized using $NiCl_2.6H_2O$ and $Na_2S.9H_2O$ in distilled water and 5M NaOH solvent are shown in Fig. 5.6. It was observed that when water is used as a solvent, only the α-NiS phase was formed. When 5M NaOH was used under similar conditions, the β-NiS phase began to form. This is due to the high solubility constant of β-NiS phase when compared to the α-NiS phase. Further, when the S sources were varied between $Na_2S.9H_2O$, S powder and $CS(NH_2)_2$, while NaOH concentration was kept constant at 5M, the binary phase NiS was formed. The major difference in this case was the rate of solubility of the S sources, with $Na_2S.9H_2O$ being the highly soluble S source. It can be seen from Fig 5.6 that the product obtained from

this source had the most intense peaks when compared to the other samples. This was due to fast accessibility of S^{2-} ions to react with the $Ni(OH)_2$ complex which resulted in a relatively high crystalline product. Further, the α-NiS is much preferred compared to β-NiS when $Na_2S.9H_2O$ is used as an S source. The sample prepared using $CS(NH_2)_2$ as an S source had the β-NiS relatively higher than α-NiS phase. When S powder was used as an S source, binary phase NiS was formed. It is worth noting here that this sample has the least intense peaks and a relatively high $Ni(OH)_2$ peak when compared to the other samples. This was attributed to the low solubility of S powder in the solvent when compared to $Ni(OH)_2$ at the given reaction conditions which resulted in relatively less complete dissolution of S^{2-} ions on the $Ni(OH)_2$ complex.

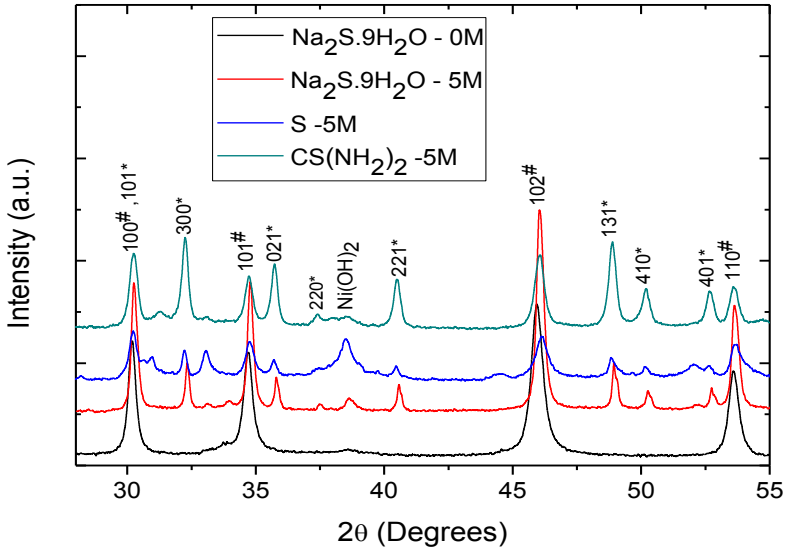


Figure 5.6: XRD patterns of the samples prepared using the same S source ($Na_2S.9H_2O$) but different solvents (water and NaOH) and samples prepared using different S sources; $Na_2S.9H_2O$, S powder, $CS(NH_2)_2$, while keeping everything else the same. The symbol (#) represent the α-NiS phase and the symbol (*) represents the β-NiS phase.

The TEM images of the NiS materials were observed to vary with solvent and an S source used as shown in Fig. 5.7. When water was used as a solvent, interconnected structures with layer–like appearance at a higher magnification were obtained. These

layer-like structures consist of ultra-thin layers of about 5 nm (width) as shown on the rectangular cropped image in Fig 5.7 (c). When 5 M NaOH was used in a similar reaction as above, hexagonal shaped nanoplatelets, nanorods and some irregular shaped particles were obtained (Fig. 5.7 d - j). This agreed well with the XRD observation made in Fig 5.6, where a binary phase (α-NiS and β-NiS) was obtained. The hexagonal shaped nanoplatelets and nanoparticles were mostly α-NiS phase, while the rods were probably β-NiS. When S powder was used as an S source, a mixture of hexagonal nanoplatelets and nanorods was obtained as shown in Fig. 5.7 d. The rectangular cropped image from the hexagonal nanoplatelet (Fig. 5.7 h) shows the lattice fringes of the platelet, confirming the presence of crystalline structures. A power spectrum was performed on the selected rectangular structure from the hexagonal nanoplatelet which confirmed a hexagonal structure (Fig. 5.7 i). When $CS(NH_2)_2$ was used as an S source, uniformly shaped nanorods were obtained with a relatively few nanoparticles present (Fig. 5.7 j & k). This was in good agreement with the XRD patterns of the β-NiS phase yield enhanced on the expense of the α-NiS phase.

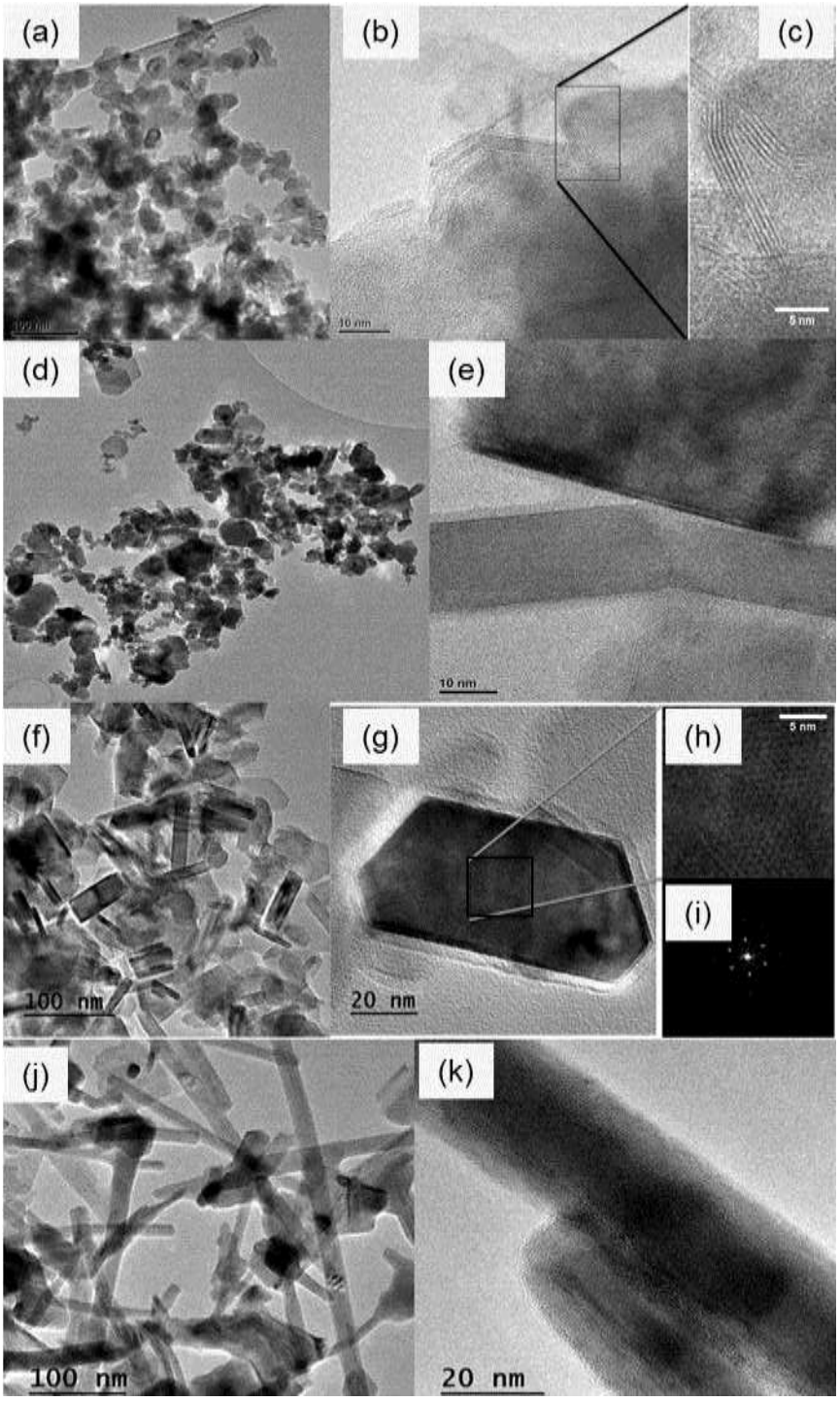


Figure 5.7: TEM images of the samples prepared using the same precursor and water (a-c) and NaOH (d & e) solvents. The samples prepared using different S sources; $Na_2S.9H_2O$ (d &e), S powder (f-i), $CS(NH_2)_2$ (j & k), while keeping everything else the same. Image (i) shows the power spectrum the image (h).

5.3.4 Precursor concentration effect: phase and morphology analysis

X-ray diffraction patterns for the samples obtained when $Ni(CH_3COO)_2.4H_2O$ and $Na_2S.9H_2O$ were used as Ni and S sources respectively, as shown in Fig. 5.8. The precursor concentrations were varied between 0.03 M and 0.11 M. It was observed that the XRD peaks shift towards right and left relative to the 0.03 M peak, depending on the concentration. A consistent observation was the reduction in the relative intensity of $Ni(OH)_2$ peak with increased precursor concentration. This could be due to the minimum particle-particle space realized at higher concentrations when compared to low concentrations which increases the Ni^{2+} and S^{2-} ions reacting probability. Further, the pH of the reagents, which also contributes to OH^- ion concentration in solution, was maintained between 8.0 and 8.1.

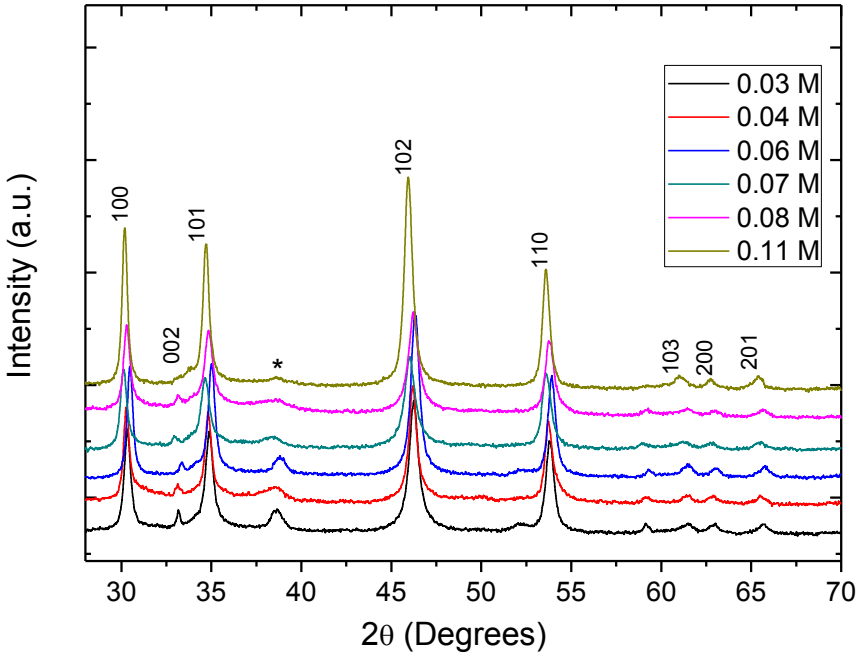


Figure 5.8: XRD profile showing α-NiS phase samples obtained at varied precursor concentrations. The symbol (*) indicates the $Ni(OH)_2$ peak.

Using the Scherrer equation, the crystallite size of a particle was found to be inversely proportional to the peak width. Fig. 5.9 shows the variation in the peak widths for the different concentrations on the left and a relative comparison between the different samples is shown for the peak centered at about 45^o on the right of Fig. 5.9. It was

observed that as the precursor concentration was increased from 0.03 M to 0.11 M, a concentration for minimum crystallite size nucleation obtained was reached at 0.07 M and the crystallite size increased again to a maximum value occurring at 0.11 M from the selected range of concentrations.

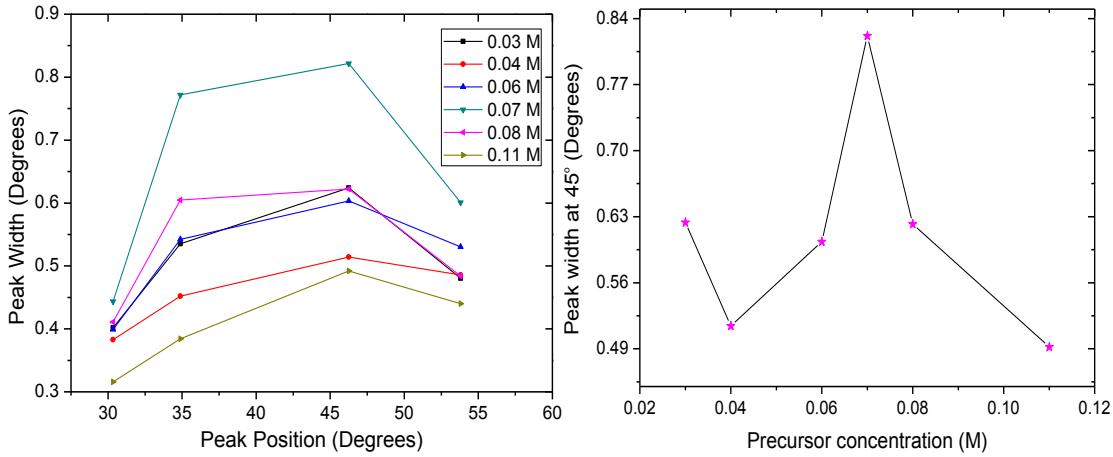


Figure 5.9: Peak width variation of the α-NiS samples as a function of concentration and peak position (left) and the variation of the peak width centered at about 45° as a function of precursor concentration.

The TEM images of the materials synthesized using different precursor concentrations show relatively similar structures (Fig. 5.10). The structures consisted of irregular shaped layer-like structures that were fused together in an irregular manner. The α-NiS phase has been reported to form layer-like structures when prepared by a hydrothermal technique using $Ni(CH_3CO_2)_2$ and $CS(NH_2)_2$ as Ni and S source respectively and water was used as a solvent in a stainless steel tank at 200 °C for 4h by Sun [25]. The structures obtained in this study do not differ much from the hydrothermally synthesized NiS structured obtained using the conventional heating methods reported in the literature review chapter. The microwave offers a fast reaction rate and less energy consumption to obtaining NiS nanostructures.

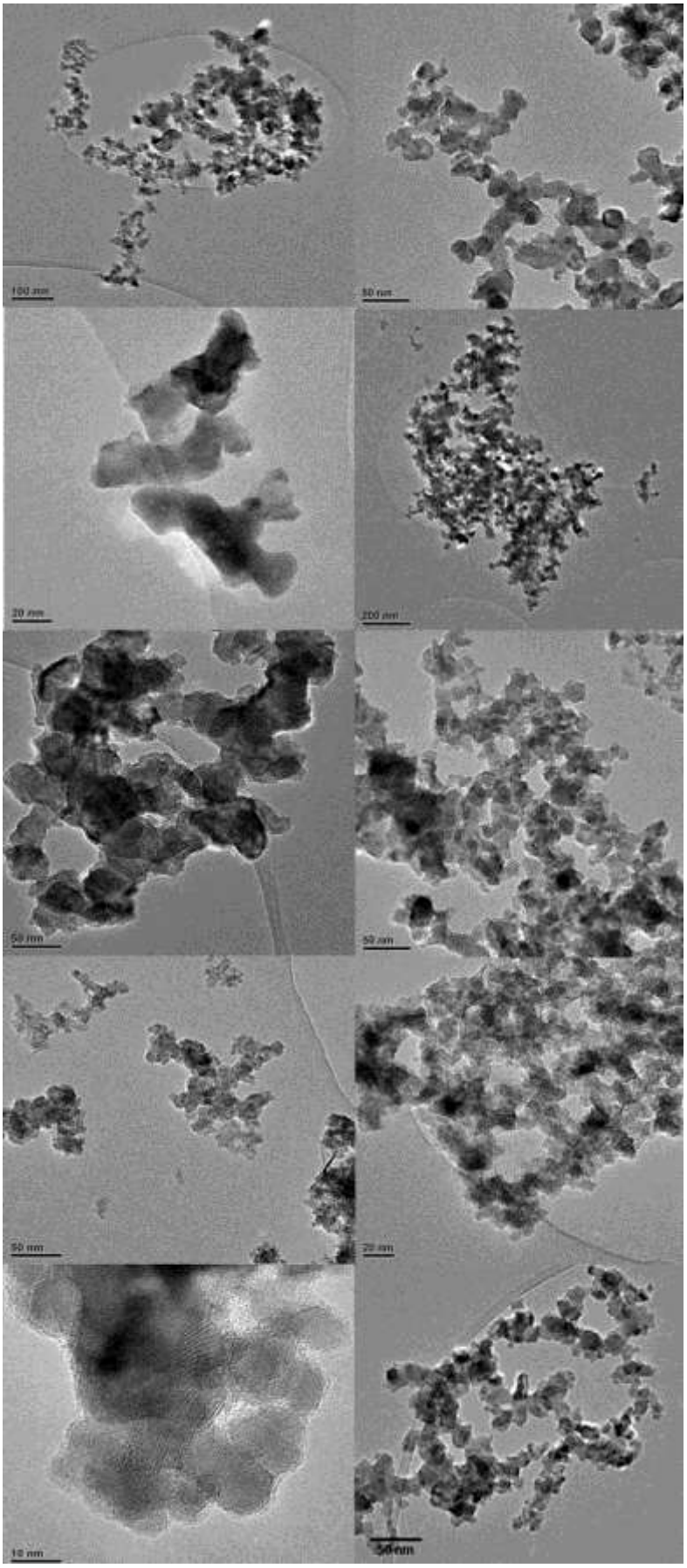


Figure 5.10: TEM images of the products from precursor concentrations 0.03 M, 0.04 M, 0.06 M, 0.07 M and 0.08 M from top to bottom respectively.

5.4 Conclusions

In Summary, a microwave-assisted hydrothermal technique for the synthesis of nickel monosulphide using Ni:S ratio of 1:1 was employed. The use of NaOH as a solvent was shown to favour a binary phase (α- and β-) NiS when the reactants; $NiCl_2.6H_2O$ and $CS(NH_2)_2$ were reacted. When holding time was evaluated in a similar reaction as above, it was shown to affect both the phase as well as the crystallite size of the products. The NaOH concentration effect was evaluated and attributed to the hydroxyl ions concentration and the reaction heating rate which affects the final phase of the product. Further, a growth mechanism was proposed due to observations made on the morphologies of the previous reactions, by the assistance of SEM and TEM imaging analysis. Water was shown to be selective to only α-NiS phase for the reaction between $NiCl_2.6H_2O$ and $Na_2S.9H_2O$, and for the reaction between $Ni(CH_3COO)_2.4H_2O$ and $Na_2S.9H_2O$. The S source effect was evaluated and the results were attributed to precursor solubility and $Ni(OH)_2$ solubility which affect the rate of NiS formation. The precursor concentration was also evaluated for the reaction between $Ni(CH_3COO)_2.4H_2O$ and $Na_2S.9H_2O$ and it was shown that the crystallite size decreases to a certain minimum and then increases between a selected range of 0.03 M to 0.11 M precursor concentrations. This study demonstrates that nanomaterials were sensitive to the reaction parameters used. The next chapter focuses on the annealing effect of the α-NiS phase nanostructures.

5.5 References

[1] Tilley, R.D., Jefferson, D.A., *J. Phys. Chem. B* **106** (2002) 10895.

[2] Salavati-Niasari, M., Davar, F., Mazaheri, M., *J. Alloys Compd.* **470** (2009) 502.

[3] Salavati-Niasari, M., Davar, F., Mazaheri, M., *Materials Research Bulletin* **44** (2009) 2246.

[4] Salavati-Niasari, M., Mir, N., Davar, F., *J. Alloys Compd.* **493** (2010) 163.

[5] Li, F., Kong, T., Wentuan, W., Li, D., Li, Z., Huang, X., *Applied Surface Science* **255** (2009) 6285.

[6] Sartale, S.D., Lokhande, C.D., *Mater. Chen. Phys.* **72** (2001) 101.

[7] Guozhen, S., Chen, D., Tang, K., An, C., Yang, Q., Qian, Y., *J. Solid State Chem.* **173** (2003) 227.

[8] Welters, W.J.J., Vorbeck, G., Zandbergen, H.W., de Haan, J.W., de Beer, V.H.J., van Santen, R.A.J., *J. Catal.* **150** (1994) 155.

[9] Zhang, X.M., Wang, C., Xie, Y., Qian, Y.T., *Materials Research Bulletin* **34** (1999) 1967.

[10] Pan, Q., Huang, K., Ni, S., Yang, F., He, D., *Materials Research Bulletin* **43** (2008) 1440.

[11] Tang, C., Zang, C., Su, J., Zhang, D., Li, G., Zhang, Y., Yu, K., *Applied Surface Science* **257** (2011) 3388.

[12] Dong, W., An, L., Wang, X., Li, B., Chen, B., Tang, W., Li, C., Wang, G., *J. Alloys Compd.* **509** (2011) 2170.

[13] Zhang, J., Qiao, S.Z., Qi, L., Yu, J., *Phys. Chem. Chem. Phys.* **15** (2013) 12088.

[14] Kassim, A., Min, H.S., Tee, T.W., Fei, N.C., *Am. J. Appl. Sci.* **8** (2011) 359.

[15] Sartale, S.D., Lokhande, C.D., *Mater. Chem. Phys.* **72** (2001) 101.

[16] Wang, L., Zhu, Y., Li, H., Li, Q., Qian, Y., *J. Solid State Chem.* **183** (2010) 223.

[17] Liu, X. *Mater. Sci. Engineering B* **119** (2005) 19.

[18] Salavati-Niasari, M., Ghanbari, D., Davar, F., *J. Alloys and Compounds* **488** (2009) 442.

[19] Al-Azri, K., Md Nor, R., Amin, Y.M., Al-Ruqeishi, M.S., *Appl. Surf. Sci*. **256** (2010) 5957.

[20] Wahab, R., Ansari, S.G., Kim, Y.S., Song, M., Shin, H.S., *Appl. Surf. Sci.* **255** (2009) 4891.

[21] Chen, S, Zeng, K., Li, H., Li, F., *J. Solid State Chem.* **184** (2011) 1989.

[22] Mane, R.S., Lokhande, C.D., *Mater. Chem. Phys.* **65** (2000) 1.

[23] Idris, N.H., Rahman, M.M., Chou, S.L., Wang, J.Z., Wexler, D., Liu, H.-K., *Electrochimica Acta* **58** (2011) 456.

[24] Zhao, W., Zhu, X., Bi, H., Cui, H., Sun, Shengrui, Huang, F., *J. Power Sources* **242** (2013) 28.

[25] Sun, X., *Appl. Surf. Sci.* **217** (2003) 23.

Chapter 6: Structural characterization, optical and magnetic properties of hexagonal NiS: Effect of annealing temperature

6.0 Preamble

This chapter describes the MW-assisted synthesis of single phase NiS using H_2O solvent. The effect of annealing temperature on the stability of NiS is studied by XRD analysis. PL and ESR properties of the annealed samples are also reported.

6.1 Introduction

Nickel and sulphur form many polymorphs such as NiS, NiS_2, Ni_3S_4, Ni_3S_2, etc [1]. Nickel monosulphide (NiS) is one of these polymorphs that crystallizes in two phases i.e. a low temperature rhombohedral (β-NiS, millerite) phase and the high temperature hexagonal (α-NiS) phase. Interest in this material came after Sparks and Komoto [2] discovered that the α-NiS phase exhibited a metal-to-insulator (MIT) phase transition which is accompanied by a paramagnetic-to-antiferromagnetic phase transition at a temperature of 264 K. Theoretical and experimental studies have been dedicated into finding out the cause of this transition as well as factors that affect it [3-10]. Nanotechnology based research has also taken its part in developing procedures for the fabrication of this unique material. This includes the search for possible applications of the material in the field of nanotechnology. Some applications are determined by the ultra-violet visible and infra-red optical applications of the nanomaterials due to possible band gap tuning as a result of a quantum confinement effect [11-26]. Electrical, optical and magnetic properties are some of the notable properties of these materials. As a result, they have a wide range of potential applications in light emitting diodes, solar cells, gas sensors and lithium ion batteries. Ni-S polymorphs are studied specifically for potential use as a cathode material in a rechargeable lithium battery,

hydrodesulfurization catalyst, in magnetic devices, and most recently as a possible replacement for Pt in visible-light photo-catalysed H_2 production reactions [23-24] and as counter electrodes for dye-sensitized solar cells [25-26].

Chemical methods that have been employed to synthesize this material include the conventional reflux method [23], a chemical bath deposition method [27], a successive ionic layer adsorption and reaction (SILAR) method [28] and a hydrothermal method [12,18]. In this work, due to its time and cost efficiency, we employ the microwave assisted hydrothermal method to synthesize α-NiS. This method is also a candidate for large scale production of nanomaterials since it is relatively fast, economical method that gives a high product yield [29-31]. A simple method to obtain novel α-NiS architectures as well as the study of their crystalline structures and optical and magnetic properties as a function of annealing temperature, is presented.

6.2 Experimental

6.2.1 Reagents and sample preparation

All reagents used were purchased from the Sigma Aldrich chemical company and were used as received without any further purification. NiS nanostructured materials were synthesized by adding equimolar solutions of $Na_2S.9H_2O$ (30 ml in distilled water) and $NiCl_2.6H_2O$ (30 ml in distilled water) together. The precursor mixture was transferred to a 100 ml Teflon vessel which was placed into a Multi-wave 3000 microwave oven. The oven was operated at 600 W for 30 minutes and fan cooled to room temperature for 20 minutes. A black precipitate of NiS formed which was washed several times using distilled water, ethanol and acetone and later dried in an oven at 90 ˚C for 6 hours.

6.2.2 Annealing

About 600 mg portions of the as-synthesized products were weighed and annealed under an air atmosphere in horizontal quartz tube furnace. The annealing temperatures were varied between 150 ˚C and 600 ˚C and annealing was carried out for 3 hours under a nitrogen gas flow (200 sccm) and a ramping rate of 20 ^{o}C/min was used.

6.2.3 Characterization

The structural analysis was performed using a Panalytical X'Pert PRO PW 3040/60 X-ray diffractometer with a Cu Kα (λ = 0.154 nm) monochromated radiation source. XRD spectra were collected in θ-2θ scan (10-90˚) with a measurement step of 0.02˚. The surface morphology was performed using a high resolution transmission electron microscope (JEOL HR-TEM 2100). Fourier transform infrared (FT-IR) spectroscopy was carried out using a Perkin-Elmer FT-IR spectrometer. The IR spectra were collected from 500 to 3500 cm^{-1}. The microwave absorption measurements were carried out using a JEOL electron paramagnetic resonance (EPR) spectrometer operated at a constant X-band microwave frequency of 9.4 GHz. For the analysis, the films were mounted in the cavity centre at a position where the microwave magnetic field is at its maximum. The DC static field was slowly swept between 0 and 500 mT. The microwave power was kept at 5 mW during the measurements. The DC field was modulated with a superposed AC field whose amplitude was varied between 0.1 mT and 0.6 mT at 100 kHz frequency. The microwave response was measured as a derivative of its microwave absorption signal at room temperature (298 K). Differential scanning calorimetry (DSC) analysis was performed using a DSC Q2000 in a nitrogen atmosphere at a flow rate of 50 ml/min. The samples were loaded on an aluminium pan and about 200 mg was weighed, and the pan was sealed for each sample. Electrical measurements were taken using a Kiethley source meter.

6.3 Results

6.3.1 Phase analysis

XRD analysis performed on the as-synthesized (raw) sample made from Na_2S and $NiCl_2$ using the microwave procedure confirmed that a hexagonal NiS phase was formed. The experimental *d*-spacing values obtained for the NiS phases were in good agreement with the JCPDS standards PDF # 897141. It can be seen in Fig. 6.1 that the XRD peaks shift towards lower angles as the NiS sample is annealed from 90 ^{o}C to 300 ^{o}C. From 300 ^{o}C, the peaks shift back towards higher angles as the NiO peaks begin to form due to the replacement of sulphur by oxygen. It can also be observed that the NiS

peaks are still dominant in the annealed samples at 400 ^{o}C, after which the NiO peaks become dominant and after 600 ^{o}C annealing temperatures only cubic NiO peaks are observed in the XRD pattern. These results are similar to results reported by Uplane *et al.* [32]. They fabricated NiO thin films from NiS in a thermal oxidation reaction at oxidation temperatures of 425, 475 and 525 ^{o}C [32]. In their report, they obtained a single NiO phase at all oxidation temperatures. This is not exactly result that was obtained in our case probably due to the different dimensions of the samples as well as the different synthesis techniques employed. This observation is further confirmed by FTIR studies (Fig. 6.5). Further information on the XRD analysis of the annealed samples is summarised in Fig. 6.2 - 6.4 and Table 6.1. Although no gas analysis of the by-products was done during the XRD analysis, the overall oxidation reaction taking place at 600 ^{o}C can be summarized in Equation 1.

$$2NiS_{(s)} + 3O_{2(g)} \xrightarrow{600\ ^{o}C} 2NiO_{(s)} + 2SO_{2(g)} \qquad (1)$$

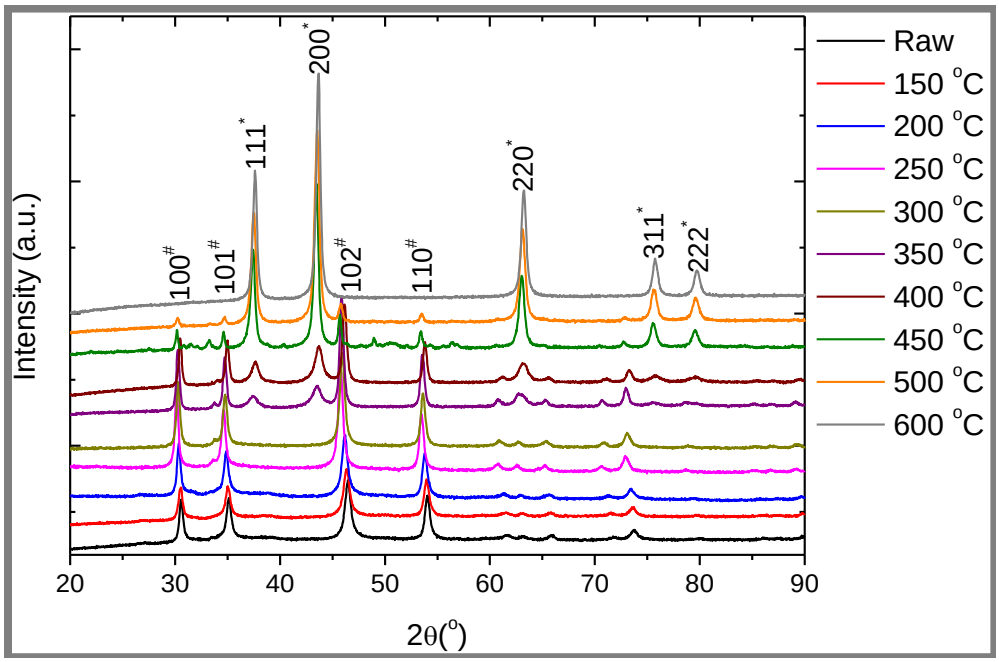


Figure 6.1: XRD pattern of NiS annealed at different temperatures (90 to 600 ^{o}C). Symbols ($^{\#}$) and (*) correspond to the indexed peaks for α-NiS and c-NiO respectively.

The crystallite size for all the samples was estimated using the Scherrer equation given in Equation 2.

$$D = \frac{K\lambda}{\beta \cos\theta} \qquad (2)$$

where D is the average dimension of the crystallites, K is a constant (usually applied as 0.9), λ (0.154 nm) is the X-ray wavelength of the CuKα_1, β is the full width at half maximum of the diffraction peak (inaccuracies associated with stress and instrumental broadening are expected) but neglected in this analysis, and θ is the Bragg angle.

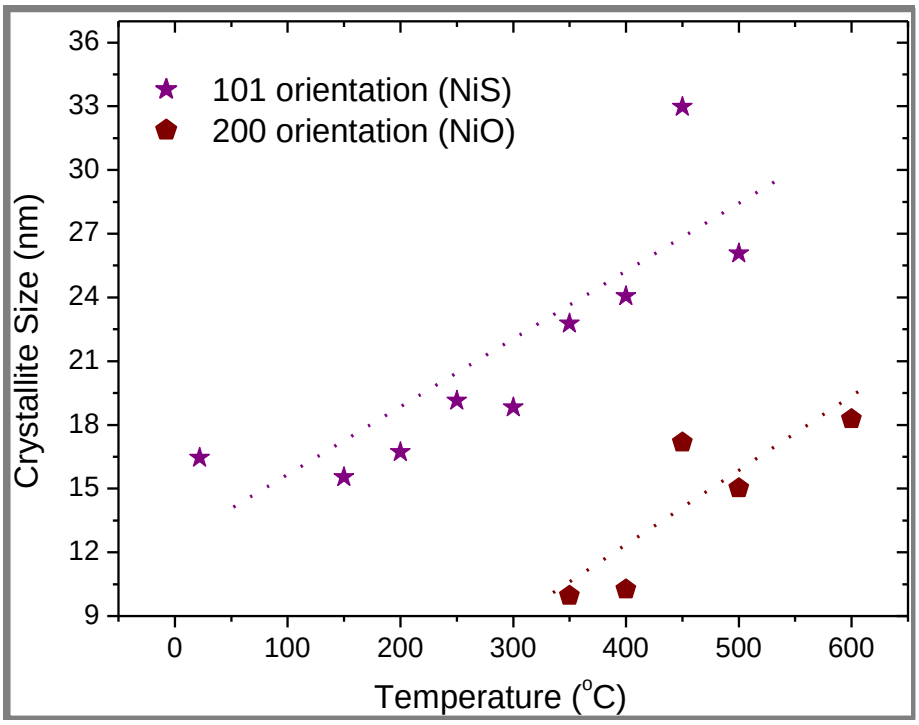


Figure 6.2: Crystallite size variation with annealing temperature, estimated by application of the Scherrer equation.

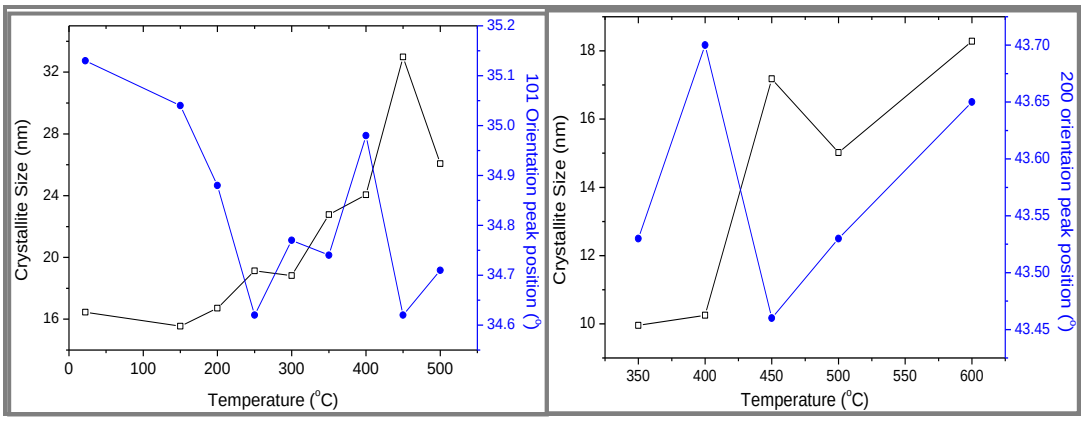


Figure 6.3: Peak shift vs estimated crystallite size as a function of temperature for the 101 peak of NiS (left) and the 200 peak of NiO (right) respectively.

Table 6.1: Summary of the shift in the XRD peak positions and crystallite sizes of NiS/NiO samples with annealing temperature.

*C-size stands for crystallite size

Annealing temperature (^oC)	Peak 101 position α-NiS (^{o})	*C-size (nm)	Peak 200 position c-NiO (^{o})	*C-size (nm)
Raw	35.13	16.45	-	-
150	35.04	15.54	-	-
200	34.88	16.72	-	-
250	34.62	19.13	-	-
300	34.77	18.83	-	-
350	34.74	22.77	43.53	9.96
400	34.98	24.06	43.70	10.25
450	34.62	32.98	43.46	17.18
500	34.72	26.08	43.53	15.02
600	-	-	43.65	18.28

A high magnification of the XRD profile of the low T data shown in Fig. 6.1 is shown in Fig. 6.4. This profile shows a very small peak for nickel hydroxide ($Ni(OH)_2$). This peak is normally observed when NiS is synthesized by solution phase techniques and is due

to the initial complexation of Ni^{2+} ions with OH^- ions in solution. $Ni(OH)_2$ is actually an intermediate phase product before NiS formation. It is worth noting that after annealing at temperatures of 250 and 300 ^oC, this peak disappears. These temperatures are the same temperatures that absorbed H_2O is expected to completely evaporate [33]. The disappearance of the $Ni(OH)_2$ peak means that OH groups have been replaced by S. This is supported by the absence of a Ni peak which appears at approximately 38^o in the XRD profile. More evidence is shown in the DSC results (Fig. 6.6). Further, the 002 orientation of α-NiS (shown in Fig. 6.4) becomes more intense after annealing of the sample at 250 and 300 ^oC. This is associated with increased crystallinity of the sample as well as phase stability of α-NiS at these temperatures.

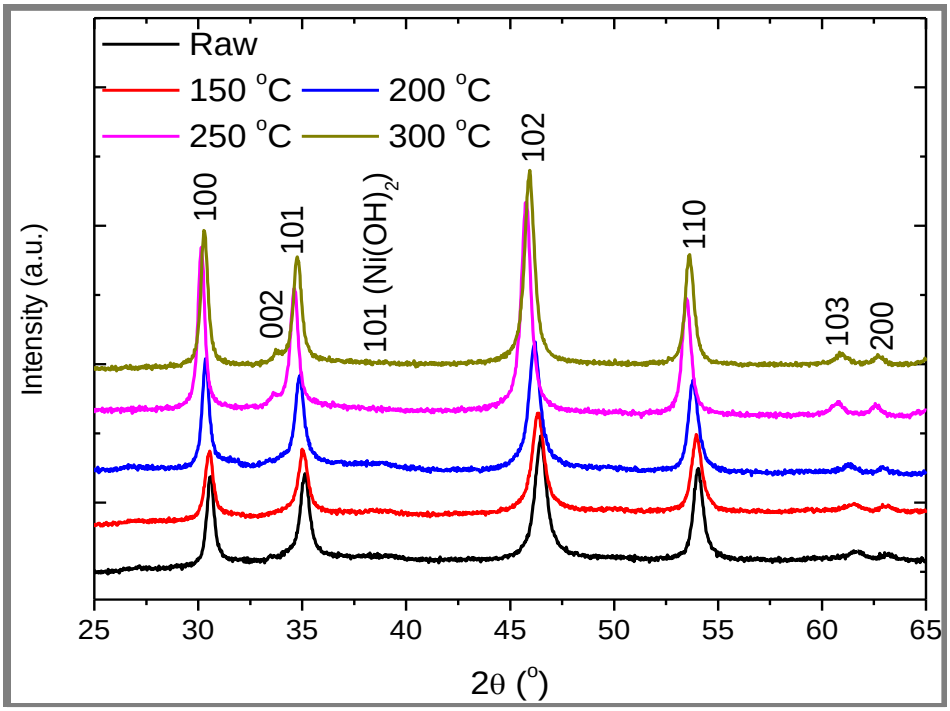


Figure 6.4: XRD pattern showing the peaks in the range; 25^o to 65^o for the α- NiS samples as a function of annealing T.

6.3.2. IR absorption properties

FTIR spectroscopy was performed on the samples as shown in Fig. 6.5. There is a clear separation between the samples dominated by NiS (black) and the samples dominated by NiO (grey). In agreement with XRD results, the samples (raw and annealed up to 400 ^{o}C) show a relatively low percentage transmittance as compared to the samples annealed between 450 to 600 ^{o}C. A relatively high transmittance is observed at 450 ^{o}C and almost 100 % transmittance for the sample annealed at 600 ^{o}C. This is related to the different optical properties of NiS and NiO. NiS is a small band gap material (about 0.3 eV) while NiO has a wide band gap (3.6 eV) and has been reported to show high percentage transmittance [34].

From the transmittance spectra, it can also be noted that SO_3^-, S-H and SO_4, vibrations are present. These are associated with the reactants used and H_2O from the atmosphere. The S-H vibration band appearing at 2097 cm^{-1} can be attributed to the interaction of the surface S with the adsorbed atmospheric H_2O vapour by H bonding. These peaks are almost completely suppressed at higher annealing temperatures, showing the absence of S-H interactions. Further, a broad band centred at 3300 cm^{-1} is observed after annealing NiS at 500 and 600 ^{o}C. This is associated with an O-H asymmetrical stretching band from adsorbed moisture from the atmosphere. Another band at 1637 cm^{-1} can be attributed to the O-H bending mode of H_2O. A small peak is observed for the NiS samples around 1070 cm^{-1}. This peak can be attributed to the presence of S=O stretching mode due to the presence of sulphate ions as a result of surface adsorbed moisture. A much more intense peak is also observed around 1070 cm^{-1} for the samples annealed at 500 and 600 ^{o}C. This peak can be attributed to C=O stretching mode which comes from atmospheric CO_2 adsorbed by the NiO phase dominated samples. Peaks for both NiS and NiO could not be identified as they appear at lower wavenumbers, below the working range of the FTIR spectrometer.

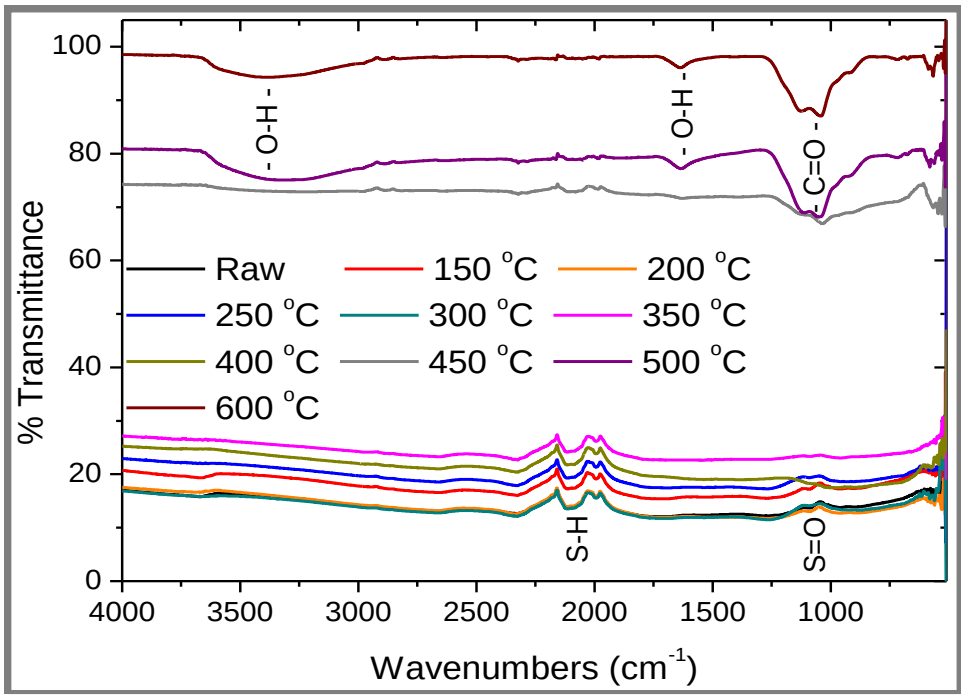


Figure 6.5: FTIR spectra of the NiS samples annealed at different temperatures (90 to 600 ^{o}C).

6.3.3. Thermal analysis

DSC patterns were recorded for all the samples. Fig. 6.6 shows the variation of heat flow with temperature for the samples; raw and annealed up to 300 ^{o}C [Fig. 6.6 (a)] and annealed at 350 to 600 ^{o}C [Fig. 6.6 (b)]. Endotherms appearing between 100 ^{o}C and 130 ^{o}C for the samples annealed below 400 ^{o}C were observed during the heating cycle. These peaks can be attributed to the elimination of physically adsorbed H_2O in the samples. A decrease in the intensity of the peaks was observed as the annealing temperature was increased. This suggest that some H_2O was eliminated during the annealing process but some residual physically adsorbed H_2O appears present and decreases in amount with increased annealing temperature. An endotherm appearing at 188 ^{o}C was observed for the raw and 150 ^{o}C annealed samples only. This can be attributed to the elimination of chemically bonded hydroxyl groups present in small amounts. This is confirmed by the small $Ni(OH)_2$ peak observed in the XRD analysis. The samples annealed above 400 ^{o}C do not show the H_2O elimination peaks. Due to

the small volume change (2%) in the crystal unit structure of the α-NiS at the point of transition, there was no significant change in heat flow at the point of metal-to-insulator transition of the samples [2]. The transition was studied by measuring the change in resistance of the sample with temperature in Fig. 6.10.

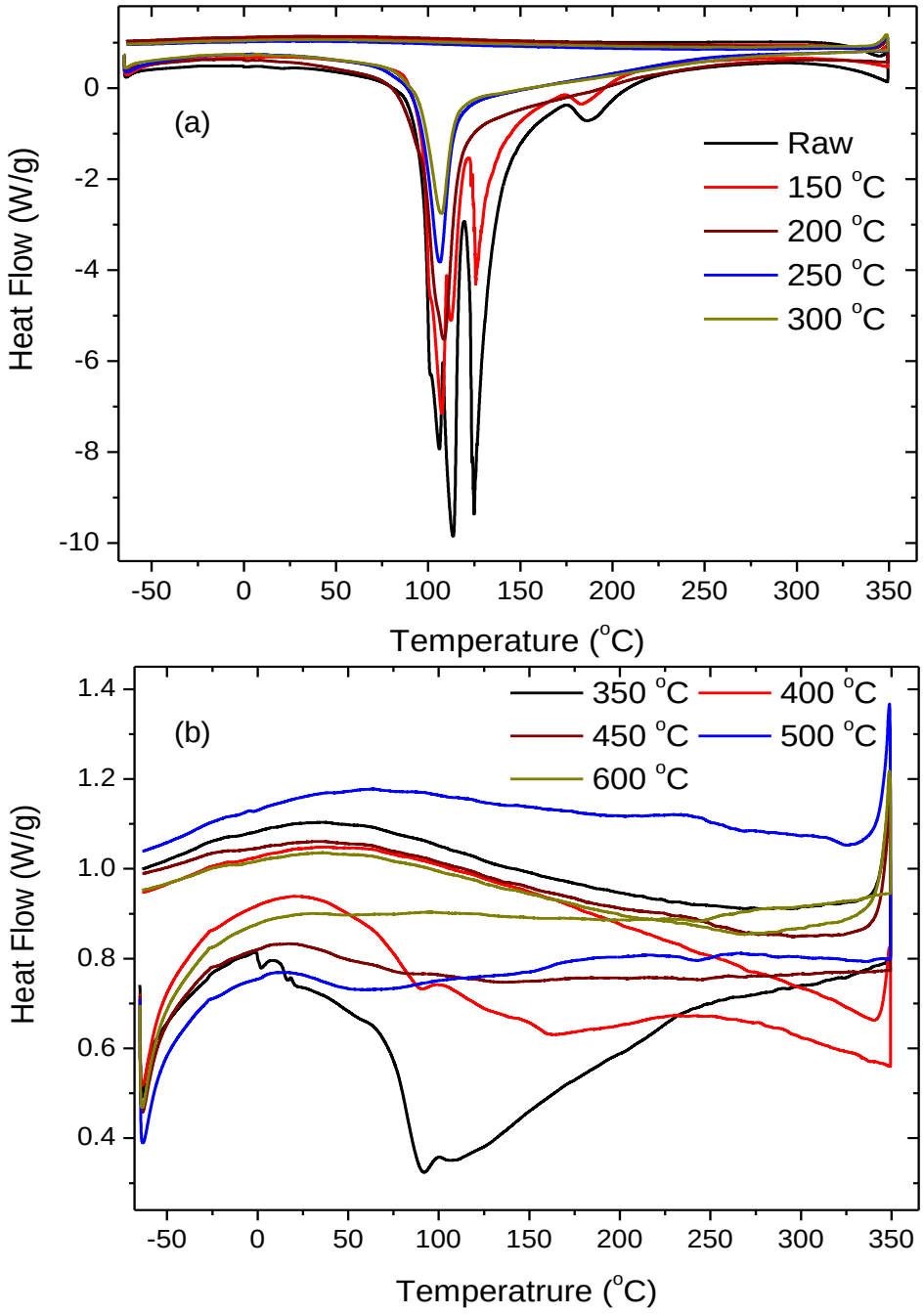


Figure 6.6: DCS plots for the raw and annealed NiS samples (a) from raw to 300 °C and (b) from 350 to 600 °C (b).

6.3.4 Microscopy analysis

TEM image analysis was performed on the raw NiS sample and the annealed samples as shown in Fig. 6.7. It can be observed from the images that the particles fused together forming hierarchical networks. These networks of particles were uniformly distributed throughout the samples as shown in the SEM images in Fig. 6.9. A high resolution image of the fused particles in Fig. 6.8 (a) reveals that the particles are actually made up of highly crystalline layer-like structures. The corresponding power spectrum of the selected area (rectangle) shown in the inset of the image in Fig. 6.8 (a) confirmed that the as-synthesized hexagonal phase NiS nanostructures are single crystalline. The average diameters of the as-synthesized NiS and the annealed samples were estimated using the image*J* program. It can be seen in Fig. 6.8 (b) that the fused layers have an average diameter of approximately 20 nm. The change in the size of the particle diameters with annealing temperature is negligible. However, it can be seen by eye observation that the surfaces are actually becoming smoother with annealing temperature, as the oxygen atoms substitute sulphur atoms. The synthesis of α-NiS by microwave-assisted hydrothermal technique has been reported by Nurul et al. where they used Ni(ac), thiourea, citric acid trisodium, 40 ml water as a solvent and 20 ml ammonia solution. They are the only group that reports on α-NiS synthesis method via microwave hydrothermal heating. They heated the reactants at 140 ^{o}C for 15 min. In their image analysis they obtained prismatic particles around 500-900 nm in size [36]. Comparing to their results, our method obtained quite narrow distributed particles without the use of a capping agent.

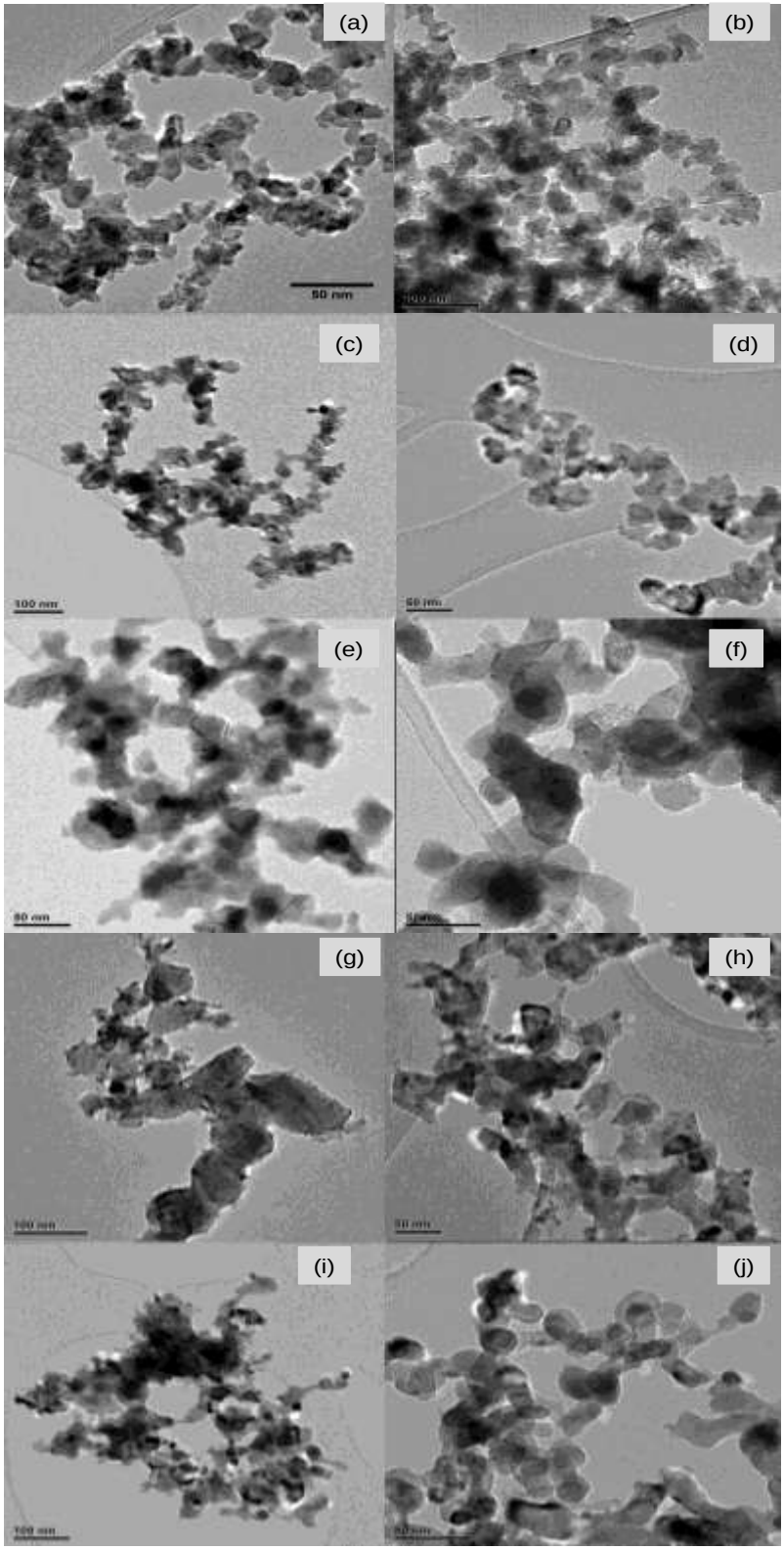


Figure 6.7: TEM images of NiS samples annealed at different temperatures (90 to 600 ^{o}C) and corresponding to images (a) – (j) respectively.

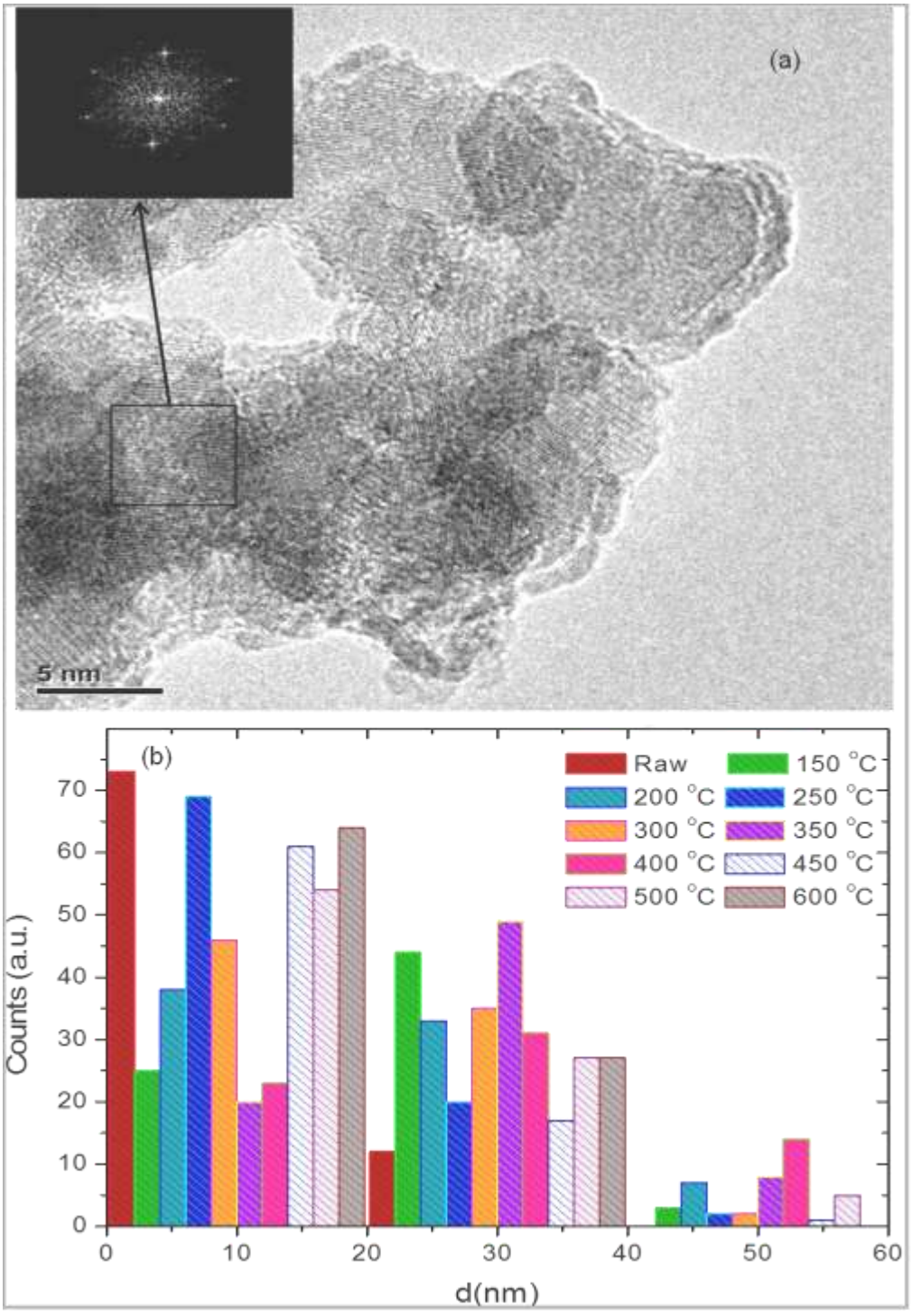


Figure 6.8: (a) High resolution TEM image of the as-synthesized NiS nanostructures and (b) diameter distribution of the annealed samples. The inset to (a) shows the power spectrum of the rectangle selected area confirming a single crystalline phase.

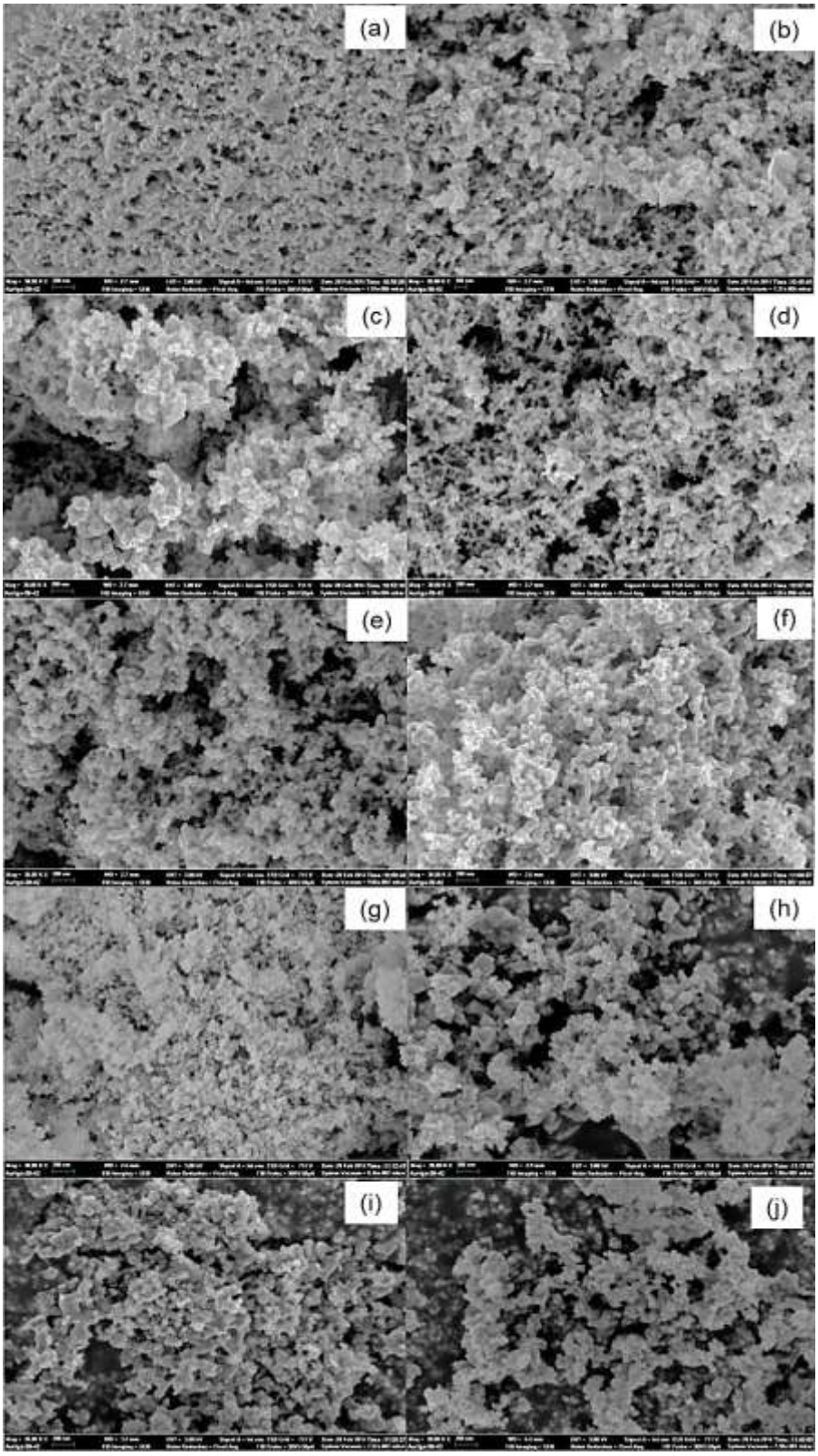


Figure 6.9: SEM images of the NiS samples annealed at different temperatures (90 to 600 ^{o}C) and they correspond to images (a) – (j) respectively.

6.3.5 Magnetic properties

The EPR measurements taken at room temperatures and 15 mW microwave power are shown in Fig. 6.10. A strong resonance peak was observed for all the samples around 300 mT and a weak signal was observed for some of the samples at lower fields (around 25 mT). The weak signal was observed to decrease with increase in annealing temperature and disappeared at an annealing temperature 300 ^{o}C. This peak may be influenced by trapped electrons on the surface of the nanomaterials or ionized surface due to the presence of defects, which disappears as the sample is annealed and gets more crystalline [37]. A new peak in the same region (around 35 mT) starts to emerge at an annealing temperature 500 ^{o}C (and 600 ^{o}C). The peak is shifted towards higher fields and it can be associated with defects of the new (NiO) formed species. The broader peak centered around 300 mT appear symmetrical for most of the samples and the position does not change, symbolising some similarities in the magnetic properties of the NiS and NiO phases. This is expected since the substitution of S with O takes place with a minimum change in the morphology and size of the nanostructures as the phase transforms from hexagonal NiS to cubic NiO.

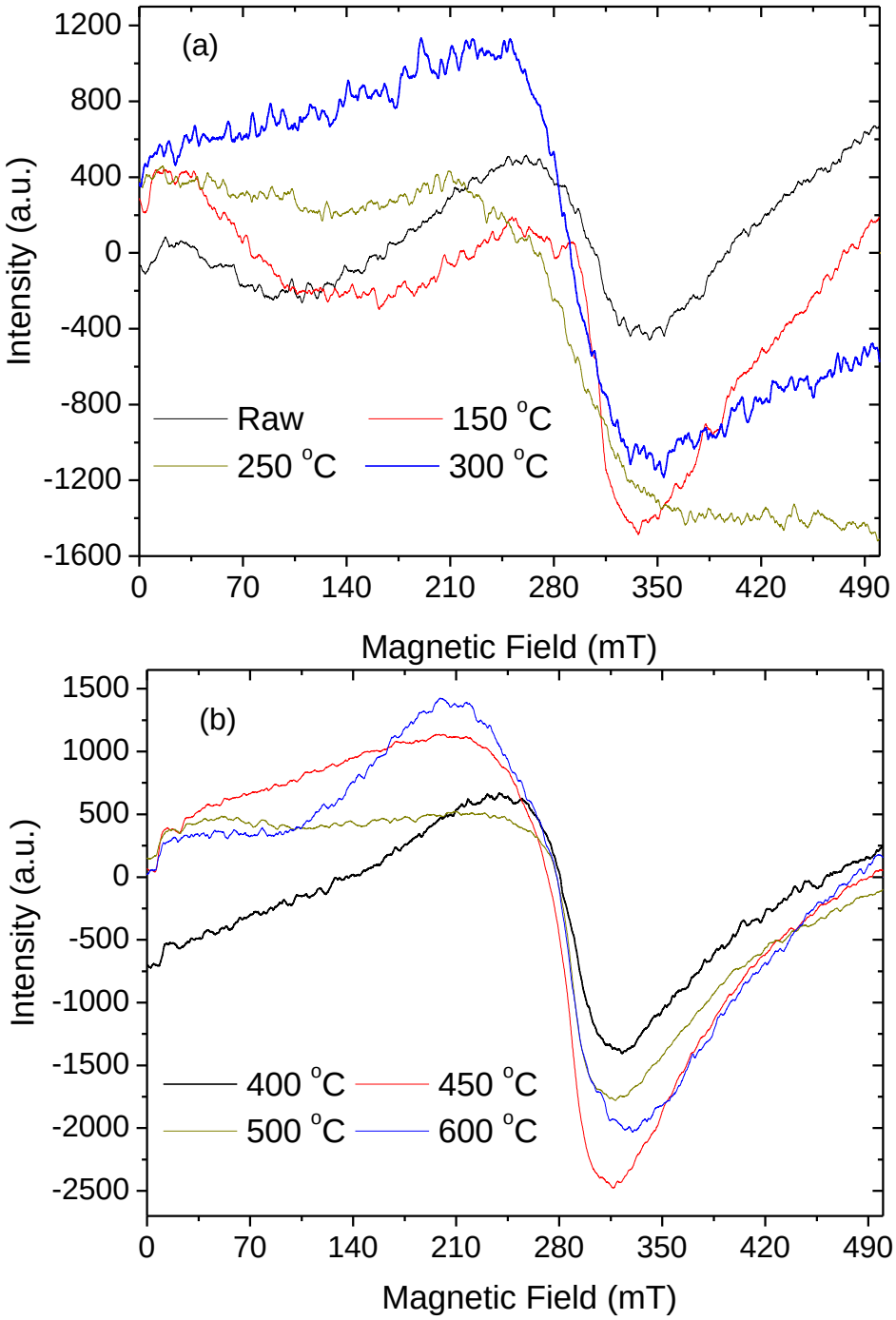


Figure 6.10: ESR results of the raw and annealed NiS samples up to 300 ^{o}C (a) and samples annealed at 400 to 600 ^{o}C (b).

The data contained in the study are interesting as they show the lineshapes in electron spin count I at various magnetization fields, H. It is usual to fit the lineshapes with either

a Gaussian or Lorentzian fit. One has to try either of the lineshape equations and choose which one fits best. After the fitting, the parameters H0, ΔH and I0 are obtained for each lineshape which in the present data are lineshapes for the raw, 150, 200, 250 …600 ^{o}C samples. Once these parameters are obtained, the number of spins A (we shall denote them as ℵ), can be quantified,. Unfortunately, neither the Gaussian nor Lorentzian could fit to the EPR data obtained because there was no perfect fit. Numerical integration of the I(H) data was therefore performed by applying the Trapezium method of finding the area under each curve as shown in Equation 3:

$$\aleph = \int_{-\infty}^{\infty} I(H)dH = \tfrac{1}{2}\left|\sum_{n=-\infty}^{n=\infty}(I_{n+1}+I_n)(H_{n+1}-H_n)\right| \qquad (3)$$

Table 6.2: Number of spins calculated using the Trapezium method for each annealing temperature.

Annealing T	#Spin
25	*122731*
150	*193598.2*
250	*350525.2*
300	*2703119*
400	*235342.7*
450	*456546.5*
500	*309045.1*
600	*412781.4*

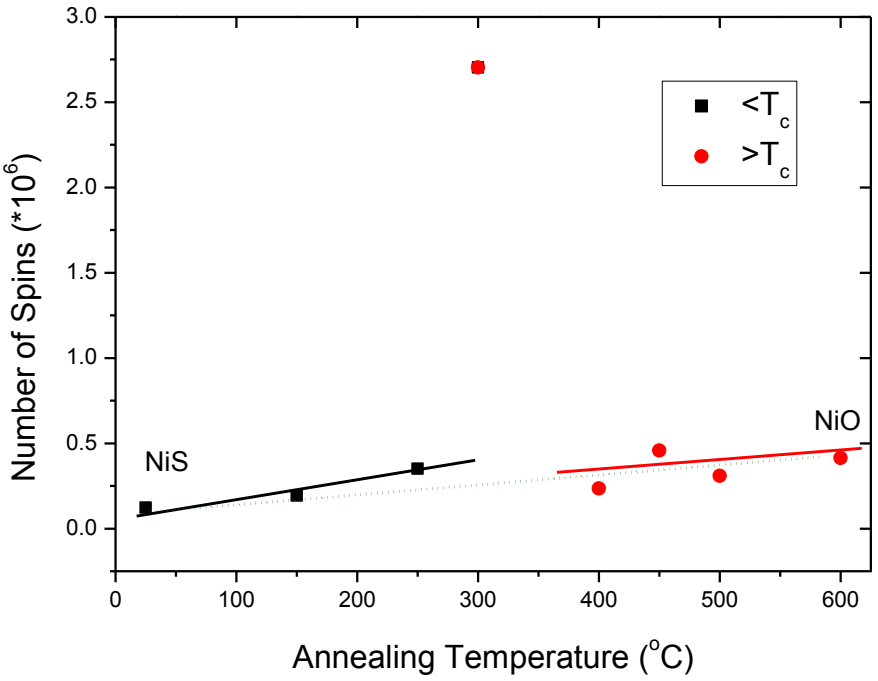


Figure 6.11: A plot of number of spins in each sample as a function of annealing temperature.

The plot in Fig. 6.11 from the values obtained in Table 6.2 reveals two possibilities in the profile of number of spins against temperatures of annealing: (1) a clear outlier point just at 300 ^{o}C and (2) the general linearity in the data below or above 300 ^{o}C. If one takes the assumption that the huge number of spins at 300 ^{o}C is not an outlier, one then has to take this as the transition temperature from NiS to the formation of NiO. The second argument seems to be more plausible i.e. at T_c, there should be a huge number of unpaired electrons as the structure of one phase (NiS) is disintegrating and the new structure of NiO is forming. However the slopes of the data above and below Tc are slightly different. The slope is steeper before [994±285 $^{o}C^{-1}$] than after [575±722 $^{o}C^{-1}$] T_c.

6.3.6 Electronic measurements

The electronic measurements were carried out on powders of the raw sample by measuring resistance versus time as the sample was heating up from liquid N_2 from about 120 K to about 291 K. The temperature was recorded manually from a thermocouple which was inserted beneath the sample holder and the recorded temperature was later used in place of time by applying the sigmoidal conversion shown in the inset of Fig. 6.11. A transition in Fig. 6.12 is evident starting around 264 K which is in good agreement with what has been reported in literature for α-NiS [3-6]. Due to the limitations of the homemade chamber, the cooling cycle could not be measured.

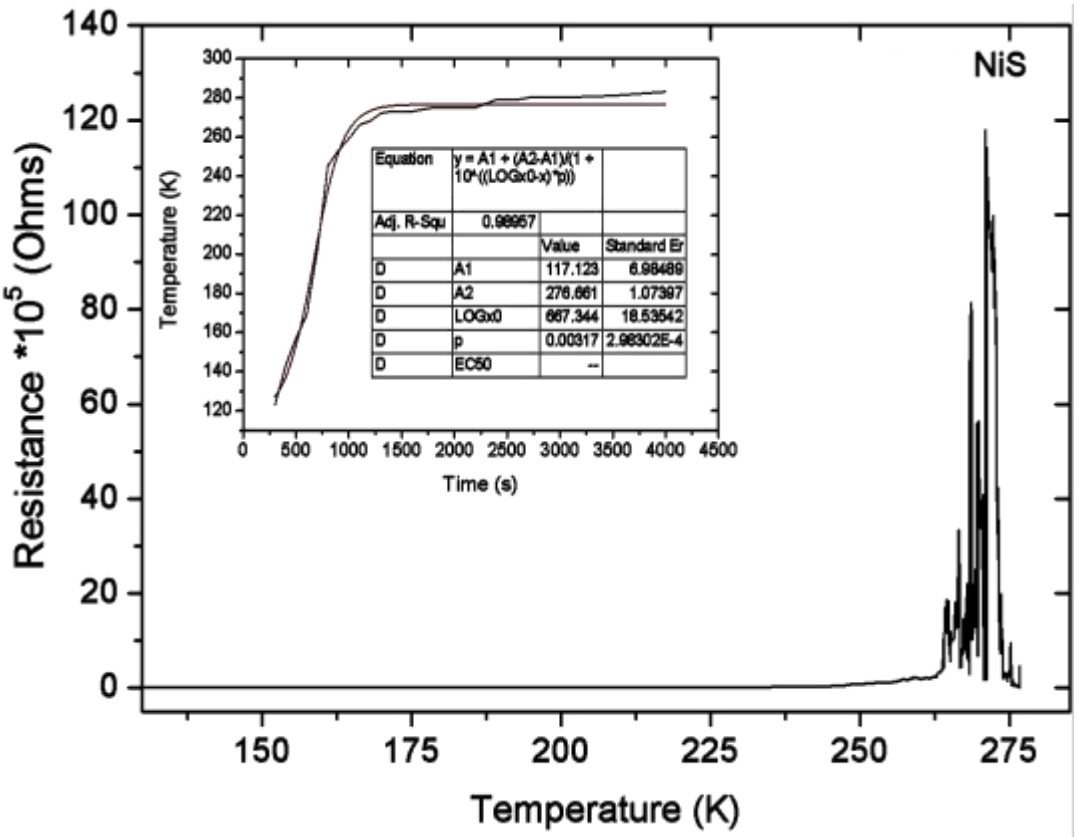


Figure 6.12: Low temperature electronic measurement of the raw sample powder. The inset is a sigmoidal curve shows the time and temperature relationship, which was used to plot resistance change as a function of temperature.

6.4 Conclusions

In summary, novel α-NiS nanostructured inter-connected networks have been synthesized by a simple and straight forward microwave irradiated hydrothermal technique, by reacting nickel chloride with sodium sulphide using water as a solvent. The obtained structures were annealed at different temperatures and characterized by XRD, FTIR, DSC, TEM, EPR techniques and electric properties were studied. A clear transition from NiS below 400 ^{o}C annealing temperature to NiO above 400 ^{o}C temperature was observed in XRD, FTIR and DSC, which is due to oxidation of the NiS material. TEM analyses confirmed that the synthesized structures have average diameters around 20 nm and were single crystalline. Both NiS and NiO showed similar magnetic properties as the hexagonal phase NiS transformed to a cubic phase NiO. The electric measurements confirmed the presence of a phase transition when heating up the raw NiS sample toward room temperature. The transition was confirmed to be around 265 K.

6.5 References

[1] Wang, L., Zhu, Y., Li, H., Li, Q., Qian, Y. *J. Solid State Chem.* **183** (2010) 223.

[2] Sparks, J.T., Komoto, T. *J. Appl. Phys.* **34** (1963) 1191.

[3] Sparks, J.T., Komoto, T. *Phys. Lett. A* **25** (1967) 398.

[4] Townsend, M.G., Tremblay, R., Horwood, J.L., Ripley, L.J. *J. Phys. C: Solid St. Phys.* **4** (1971) 598.

[5] White, R.M., Mott, N.F. *Philos. Mag*. **24** (1971) 845.

[6] Matthesis, L.F. *Phys. Rev. B.* **10** (1974) 995.

[7] Fujimori, A., Namatame, H., Matoba, M., Anazi, S. *Phys. Rev. B* **42** (1990) 620.

[8] Brusetti, R., Coey, T.M.D., Czyzek, G., Fink, J., Gomp, F. *J. Phys. F: Metal Phys.* **10** (1980) 33.

[9] Nakamura, M., Sekiyama, A., Namatame, H., Kino, H., Fujimori, A., Misu, A., Ikoma, H., Matoba, M., Anzai, S. *Phys. Rev. Lett.* **73** (1994) 2891.

[10] Krishnakumar, S.R., Shanthi, N., Mahadevan, P., Sarma, D.D. *Phys. Rev. B* **61** (2000) 16370.

[11] Salavati-Niasari, M., Davar, F., Mazaheri, M. *Mater. Res. Bull.* **44** (2009) 2246.

[12] Mane, R.S., Lokhande, C.D. *Mater. Chem. Phys.* **65** (2000) 1.

[13] Dong, W., An, L., Wang, X., Li, B., Chen, B., Tang, W., Li, C., Wang, G. *J. Alloys Compd.* **509** (2011) 2170.

[14] Meng, Z., Peng, Y., Xu, L., Qian, Y. *Mat. Lett.* **53** (2002) 165.

[15] Sun, X. *Appl. Surf. Sci.* **217** (2003) 23.

[16] Lai, C.-H., Lu, M.-Y., Chen. L.-J, J. *Mater. Chem.* **22** (2012) 19.

[17] Han, S.-C., Kim, K.-W., Ahn, H.-J., Ahn, J.-H., Lee, J.-Y. *J. Alloys Compd.* **361** (2003) 247.

[18] Liu, X. *Mater. Sci. Engineering B* **119** (2005) 19.

[19] Wang, J., Chew, S.Y., Wexler D., Wang, G.X., Ng, S.H., Zhong, S., Liu, H.K. *Electro. Commun.* **9** (2007) 1877.

[20] Tang, C. Zang, C., Su, J., Zhang, D., Li, G., Zhang, Y., Yu, K. *Appl. Surface Sci.* **257** (2011) 3388.

[21] Zhang, H.T., Wu, G., Chen, X.H. *Mater. Lett.* **59** (2005) 3728.

[22] Idris, N.H., Rahman, M.M., Chou, S.-L., Wang, J.-Z., Wexler, D., Liu, H.-K. *Electrochemica Acta* **58** (2011) 456.

[23] Zhang, J., Qiao, S.Z., Qi, L., Yu, J. *Phys. Chem. Chem. Phys.* **15** (2013) 12088.

[24] Zhang, L., Tian, B., Chen, F., Zhang, J. *International Journal of Hydrogen Energy* **37** (2012) 17060.

[25] Zhao, W., Zhu, X., Bi, H., Cui, H., Sun, S., Huang, F. *J. Power Sources* **242** (2013) 28.

[26] Li, Z., Gong, F., Zhou, G., Wang, Z.-S. *J. Phys. Chem. C* **117** (2013) 6561.

[27] Kassim, A., Min, H.S., Tee, T.W., Fei, N.C. *American J. Appl. Sci.* **8** (2011) 359.

[28] Sartale, S.D., Lokhande, C.D. *Mater. Chem. Phys.* **72** (2001) 101.

[29] Li, M.-L. Yao Q. –Z, Zhou, G. –T., Qu, X.F., Mu, C.F., Fu, S.-Q. *Cryst. Eng. Comm*. **13** (2001) 5936.

[30] Xuan, T., Wang, X., Liu, J., Li, H., Pan, L., Sun, Z. *J. Mater. Chem. C* **1** (2003) 4550.

[31] Firth, A.V., Tao, Y., Wang, D.S., Ding, J.F., Bensebaa, F. *J. Mater. Chem.* **15** (2005) 4367.

[32] Uplane, M.M., Mujawar, S.H., Inamdar, A.I., Shinde, P.S., Sonavane, A.C., Patil, P.S. *Appl. Surf. Sci.* **253** (2007) 9365.

[33] Le Parlouer, P. *Thermochimica Acta* **121** (1987) 307.

[34] Sato, H., Minani, T., Takata, S., Yamada, T. *Thin Solid Films* **236** (1993) 27.

[35] Coey, J.M.D., Brusetti, R., *Phys. Rev. B* **11** (1975) 671.

[36] Idris, N.H., Rahman, M.M., Chou, S.L., Wang, J.Z., Wexler, D., Liu, H.-K., *Electrochimica Acta* **58** (2011) 456.

[37] Alvi, N.H., ul Hasan, K., Nur, O., Willander, M., *Nanoscale Res. Lett.* **6** (2011) 130.

Chapter 7: Preliminary studies on synthesis and relative humidity sensing of Ni_3S_2 layer-based flower-like structures and impurity Se and Te doped Ni_3S_2

7.0 Preamble

This chapter describes the synthesis of the Ni_3S_2 phase of nickel sulphide. The microwave heating method was used to synthesize this material. The Ni_3S_2 was also doped with small amounts of Se and Te impurities. Relative humidity gas sensing of the pure phase of the material was studied.

7.1 Introduction

Nickel sulphide (Ni_3S_2) is the most stable of the nickel sulphide polymorph phase. The material occurs in nature as a mineral called heazlewoodite which has a rhombohedral phase. It has recently been reported to have applications in lithium ion batteries and solar cells [1, 2]. This material has been reported to be a good metallic conductor with a room temperature resistivity of about 1.8×10^{-5} Ω cm [3]. There has been little research that has been done to study the physical properties of the Ni_3S_2 material that include its photoluminescence (PL) properties, magnetic properties and gas sensing properties especially when it has nanoscale dimensions. Of the metal sulphide group of materials, ZnS has received much attention in the area of gas sensing and has been reported to show sensitivity to NO_2 gas that is comparable or much higher than the reported sensitivity of some MO_x materials [4].

Doping of semiconductors with metal/non-metal impurities is done to introduce localised energy levels in the forbidden band and/or tune the energy band gap of a semiconductor [5]. This affects the emission properties of the semiconductor and its overall electronic properties. Doping of a single phase nickel sulphide material is a

challenge due to the existence of different polymorphs. Both Se and Te have been reported to affect the properties on nanostructures when doped in small percentages [6, 7]. The Ni_3S_2 material was chosen for doping due to its high chemical stability when compared to the other NiS_x phases. In this study, small amounts of Se and Te were used to dope Ni_3S_2 materials and. Further, relative humidity (RH) sensing of the Ni_3S_2 materials was studied.

7.2 Experimental

7.2.1 Reagents and sample preparation

All reagents used were purchased from the Sigma Aldrich (South Africa, Gauteng) chemical company and were used as received without any further purification.

Ni_3S_2 nanostructures were obtained from a reaction of $NiCl_2.6H_2O$ (0.010 mol) and thiourea (0.013 mol) in distilled H_2O (50 ml). The mixture was stirred for 5 minutes to ensure homogeneity and transferred into a 100 ml Teflon vessel. The reactants were then heated under microwave irradiation at 600 W and 110 ^oC for 30 minutes and fan cooled to room temperature. The black precipitate obtained was washed several times with distilled H_2O and ethanol followed by drying in an oven at 90 ^oC for 6 hours.

To dope Ni_3S_2 with Se or Te, a similar method was followed. $NiCl_2.6H_2O$ (0.010 mol), thiourea (0.012 mol) and [NaO_3S_2 (0.0003 mol) or TeO_2 (0.0003 mol)] in distilled H_2O (50 ml). The mixtures were stirred for 5 minutes to ensure homogeneity and transferred into a 100 ml Teflon vessel. The reactants were then heated under microwave irradiation at 600 W and 110 ^oC for 30 minutes and fan cooled to room temperature. The products obtained were washed several times with distilled H_2O and ethanol followed by drying in an oven at 90 ^oC for 6 hours. (**NB:** The doping percentage is labelled from the experimental percentage dopant content used and not the actual yield).

7.2.2 Characterization

The phases of the prepared samples were investigated using X-ray diffraction [Philips PW 1830 X-ray diffractometer with a Cu Kα (λ = 0.154 nm)]. Sample morphologies were studied using a scanning electron microscopy (ZEISS SEM) and transmission electron microscopy (JEOL-JEM 2100). The chemical compositions of the samples were obtained by energy dispersive X-ray spectroscopy (EDS) using a ZEISS SEM attachment. The photoluminescence spectra (PL) of the samples were recorded at room temperature from 310 nm to 800 nm using a Horiba Jobin Yvon HR320 Spectro-fluorometer by exciting the samples with the 300 nm line of a deuterium lamp. The emission was detected with a Jobin-Yvon MPT detector. The drop cast method was used to make the sensing device by stirring Ni_3S_2 powder in ethanol and casting a drop on top of Pt electrodes which were supported on alumina substrates. The RH sensing was measured at room temperature by use of humidifier (water bath) and synthetic air was used as the carrier gas. The RH sensing was varied between 25 % and 63 % and Kiethley source meter was used as a voltage source.

7.3 Results and discussion

7.3.1 Phase analysis

XRD analysis of the as-synthesized products, shown in Fig. 1 confirms that a single phase Ni_3S_2 was formed and all the peaks were indexed to the rhombohedral phase. There were no new diffraction peaks observed that were associated with the doped materials from XRD patterns. This suggests that the small amount of dopants added exist in the form of impurity atoms and they did not change the crystal structure of Ni_3S_2. A shift of the XRD peaks to lower angles [Fig 7.1 (b)] was observed for both the samples doped with Se and Te which can be attributed to coordination doping of the Se and Te metal impurities into the Ni_3S_2 matrix [8]. Since both doping elements coordinate differently to Ni, the lattice parameters are expected to change. The crystalline size of the samples was estimated using the Scherrer equation, assuming that strain effects were homogeneous throughout the samples. The results are listed for selected

orientations in Table 7.1. The shift in peak positions for the doped samples was accompanied by decreased grain size, which indicated that the dopants have a deteriorating effect on the Ni_3S_2 crystalline quality [9].

Table 7.1: Crystallite sizes in nm of the prepared samples estimated by the Scherrer equation.

Orientation	Ni_3S_2	$Ni_3S_{1.95}Se_{0.05}$	$Ni_3S_{1.95}Te_{0.05}$
101	31.8	28.3	29.9
110	25.5	19.2	21.5
202	25.9	21.1	25.9

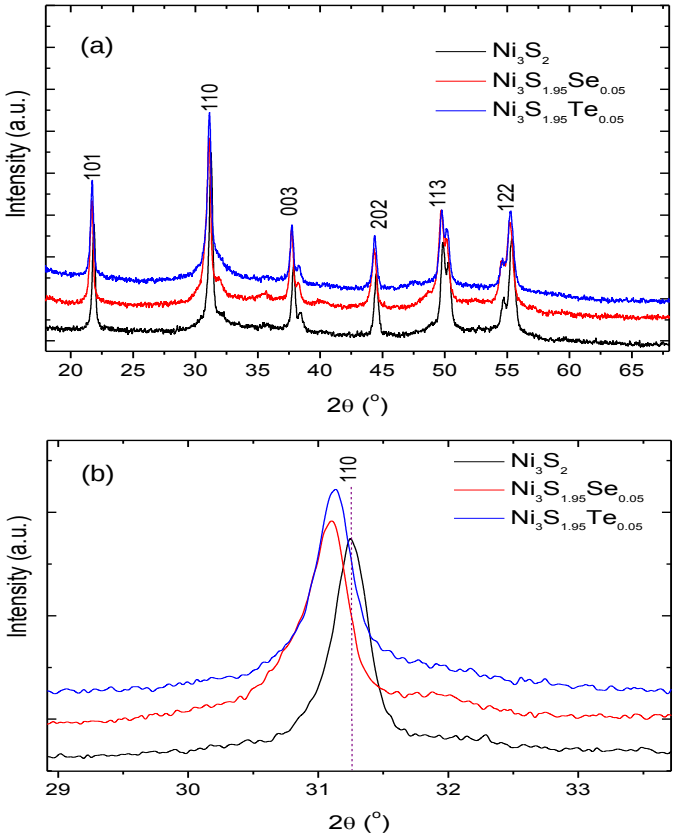


Figure 7.1: (a) XRD patterns of the samples prepared without doping and with 2.5 % Se and Te doping. (b) Zoomed image of the 110 crystalline orientations showing a shift in peak positions as a function of doping.

7.3.2 Microscopy analysis

TEM images revealed that the synthesized structures formed were layer-based flower-like structures with dimensions in the micrometer range. It can be seen in the SEM images in Fig. 7.2 (b-d) that the thin layer structures form clusters that appear like flowers.

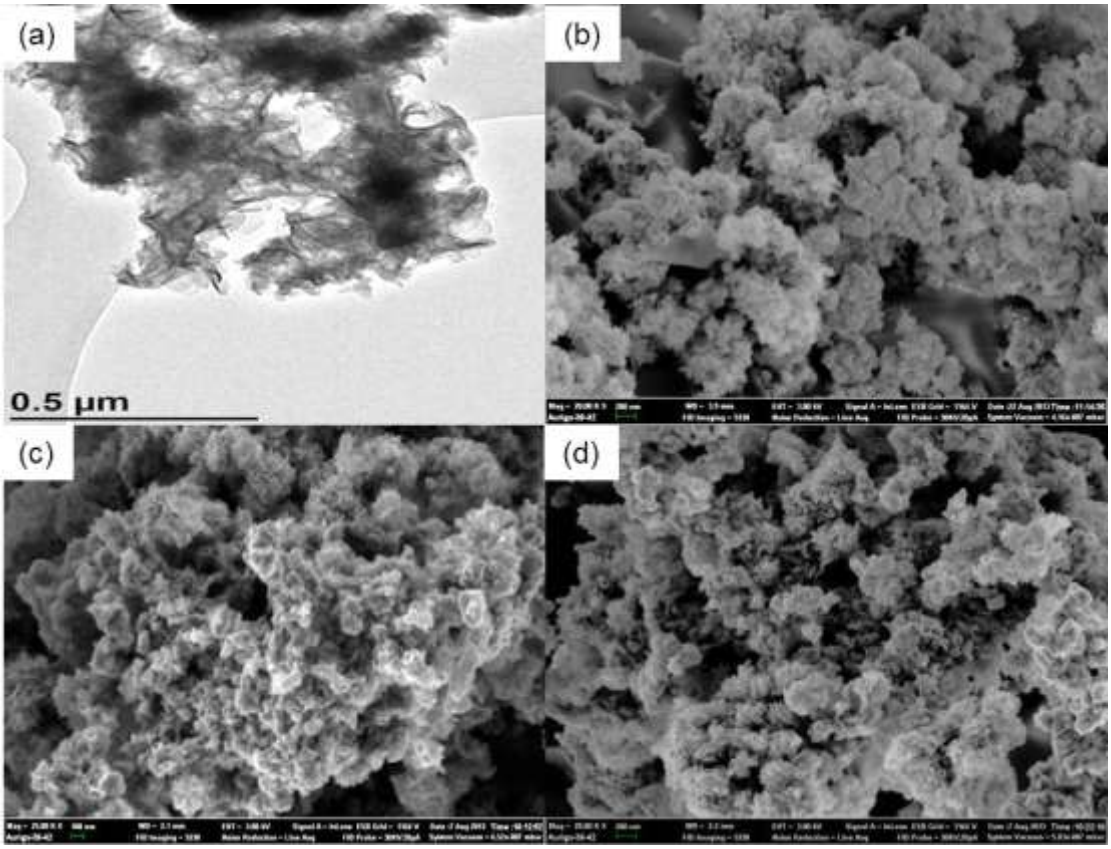


Figure 7.2: TEM and SEM images of the flower-like Ni_3S_2 materials. (a & b) pure Ni_3S_2, (b) $Ni_3S_{1.95}Se_{0.05}$, and (c) $Ni_3S_{1.95}Te_{0.05}$.

7.3.3 EDS analysis

Elemental analysis of the prepared samples was determined by EDS and data is shown in Fig. 7.3. Both Ni and S were detected with varying concentrations. Ni has high cocentration as expected from the XRD phase analysis. The presence of oxygen can be attributed to surface adsorbed oxygen. A similar observation was made for the Se

doped samples with the exception of high C content. This is related to the selected area for X-ray analysis which had much of the C support used to disperse the samples exposed during time of analysis. The presence of Te was also confirmed in Fig. 7.3 (c) by the presence of Te peaks.

The elemental composition mapped images shown in Fig. 7.4 show the distribution of all the elements in the doped samples. It can be seen from both images for Se and Te that the doped elements are uniformly distributed throughout the sample. This suggest that the dopants nucleated and precipitated at the same time Ni_3S_2 formation.

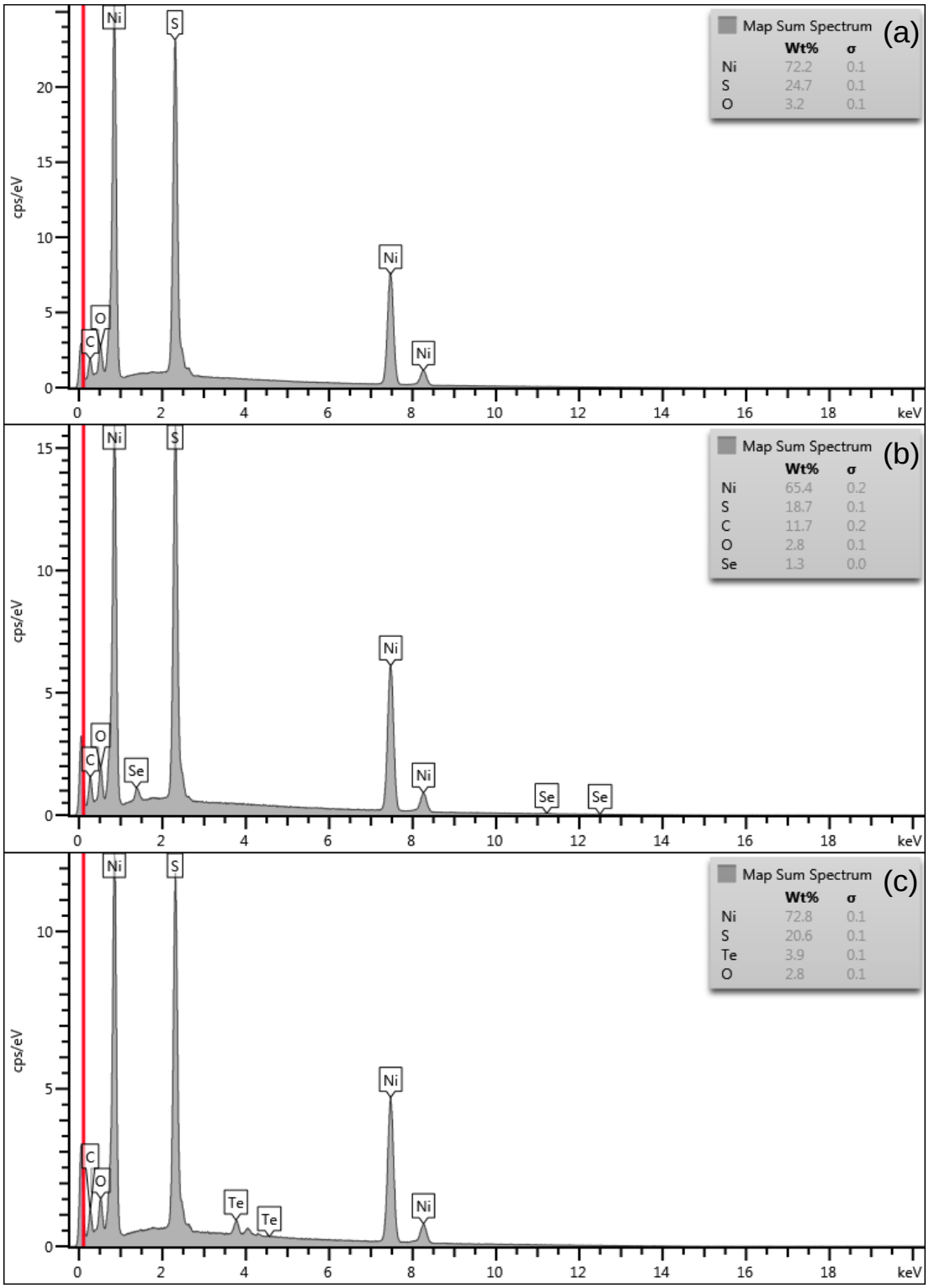


Figure 7.3: EDS spectra of the prepared samples (a) pure, (b) Se doped and (c) Te doped.

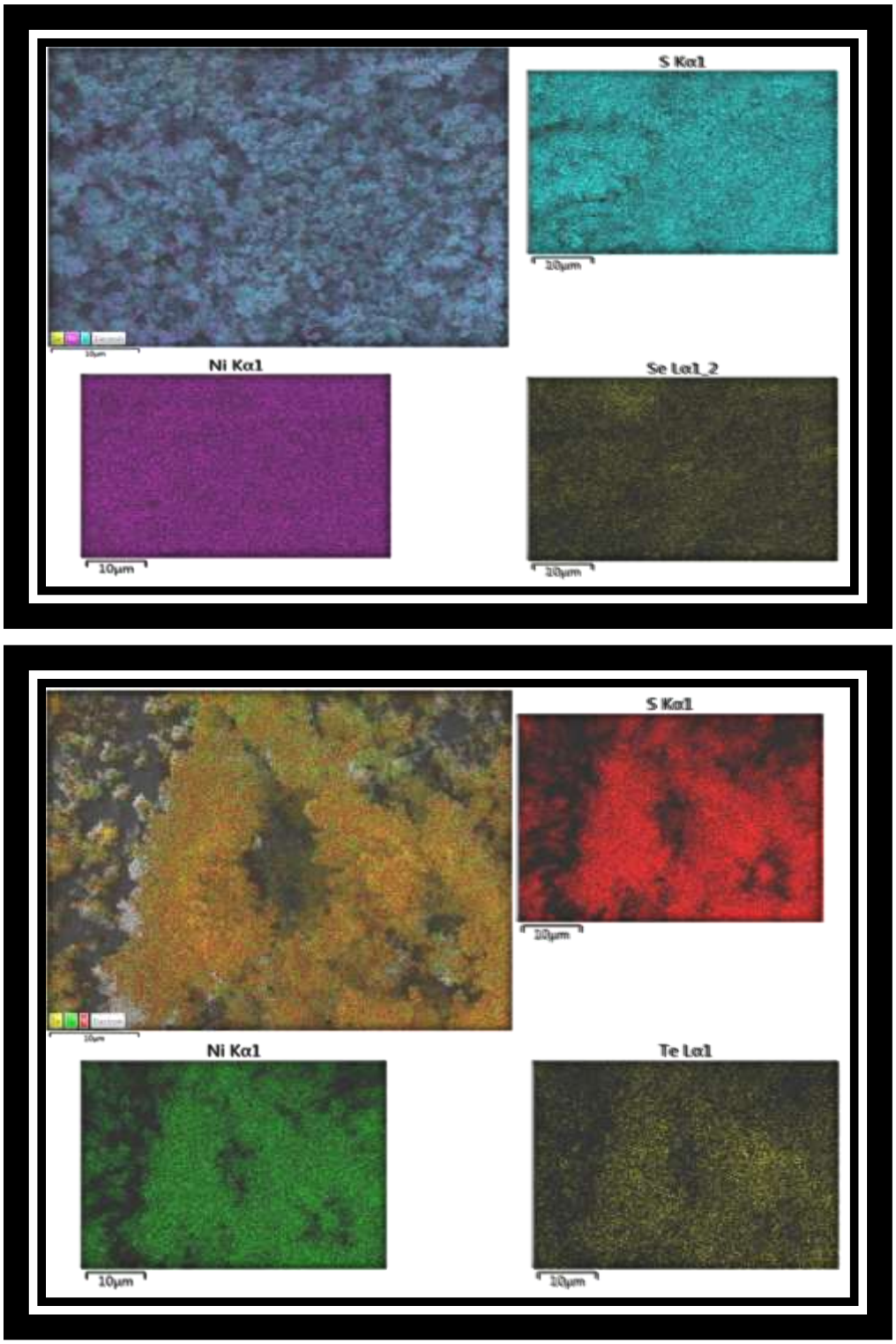


Figure 7.4: EDS mapped images of the Se doped (top) and Te doped samples showing elemental distribution of the elements Ni, S, Se and Te.

7.3.4 Photoluminescence

The room temperature PL properties of the materials were investigated. A broad UV emission peak located around 360 nm and another broad near infrared (NIR) peak centered at 700 nm were observed for Ni_3S_2 in Fig. 7.5. These can be attributed to the recombination of electrons with holes that are trapped within the energy band structure of Ni_3S_2 since this material does not have an energy gap in the visible range [3]. After doping with Se both the UV and NIR emission peaks appeared to be quenched while new peaks were observed, at higher wavelengths. The observed shift can be attributed to charge separation. Modified electronic states exist, which a rise during the nucleation of the particles which cause alteration of the Ni_3S_2 energy levels due to overlap with Se states [10]. An enhancement in the PL emission for the Te doped sample was observed for both the UV and NIR emissions. This suggests that there is an energy transfer from Te to Ni_3S_2 upon excitation, which enhances the overall emission.

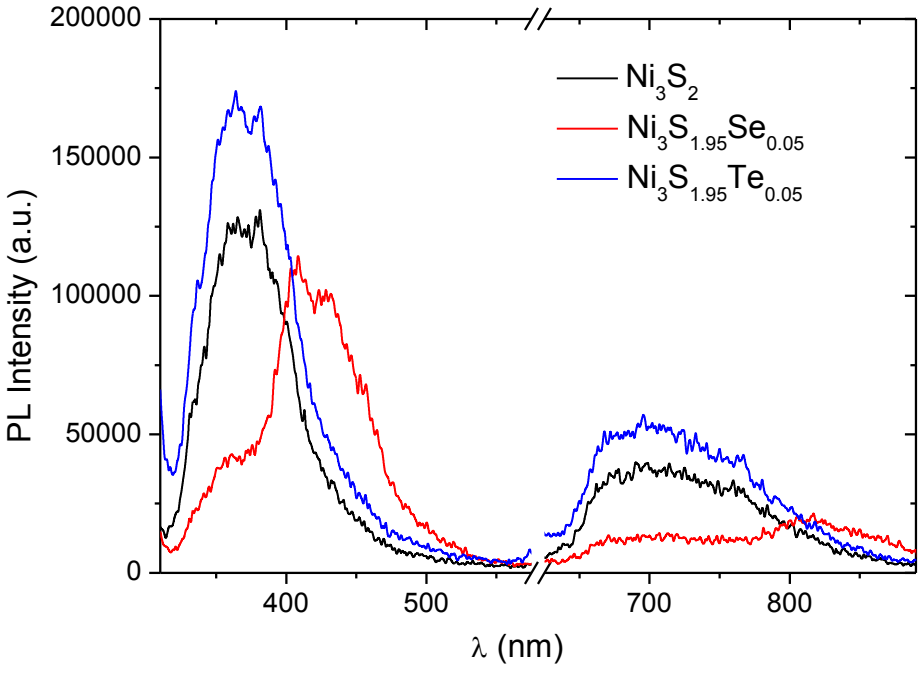


Figure 7.5: Shows photoluminescence spectra of the prepared samples excited at λ = 300 nm.

7.3.5 Relative humidity (RH) sensing

The RH sensing of the prepared pure, Se doped and Te doped Ni_3S_2 based devices was measured at controlled room temperatures of 25 ^oC by recording a change in the resistance of the device when different RH percentages were introduced to the sensor and dry synthetic air was used to monitor the sensor recovery. A drop in resistance was observed in the presence of RH which changed with RH %. A recovery of the peak intensity was also observed in the presence of air [Fig. 7.6 (a)]. The sensing response (S) of the sensor was calculated by using $S = R_{air}/R_{RH}$ [11], where R_{air} is the resistance of the sensor in air environment and R_{RH} is the maximum resistance reached by the sensor in humid environment. A sensitivity of up to 4.5 was achieved at 70 % RH for pure Ni_3S_2 as shown in Fig. 7.6 (b). This can be attributed to the high surface provided by the layer-like strictures of the sensing material. A sensing response of up to 2.5 and 1.4 was obtained for the Se and Te doped samples respectively. Improvement of the procedure for device fabrication should allow for easy interpretation of the differences on the sensitivities of the sensor devices. Future experiments should verify whether the dopants can be used to reduce or improve humidity sensitivity of the nickel sulphide materials.

The change in resistance as a result of RH sensing is due to the adsorption of moisture on the sensor surface. Moisture adsorption affects the protonic conduction taking place on the surface, which affects the sensor conductivity as the amount of adsorbed water molecules change. Depending on the conduction mechanism of water molecules on the sensor surface, humidity sensing can be ionic or electronic [12]. At low humidity, conduction is due to proton hopping between hydroxyl ions on the first layer of chemisorbed water, while at higher humidity, protons hop between physisorbed molecules with a Grotthus chain reaction mechanism [12, 13]. In the latter case, H^+ proton diffuses through the ordered hydrogen bonded array of water molecules. The proton hops

from one water molecule to another in the direction of externally applied electric field. Because protonic transport increases with increasing RH there will be a decrease in the device impedance. This is confirmed by the decreasing resistance of the sensor device when RH is introduced.

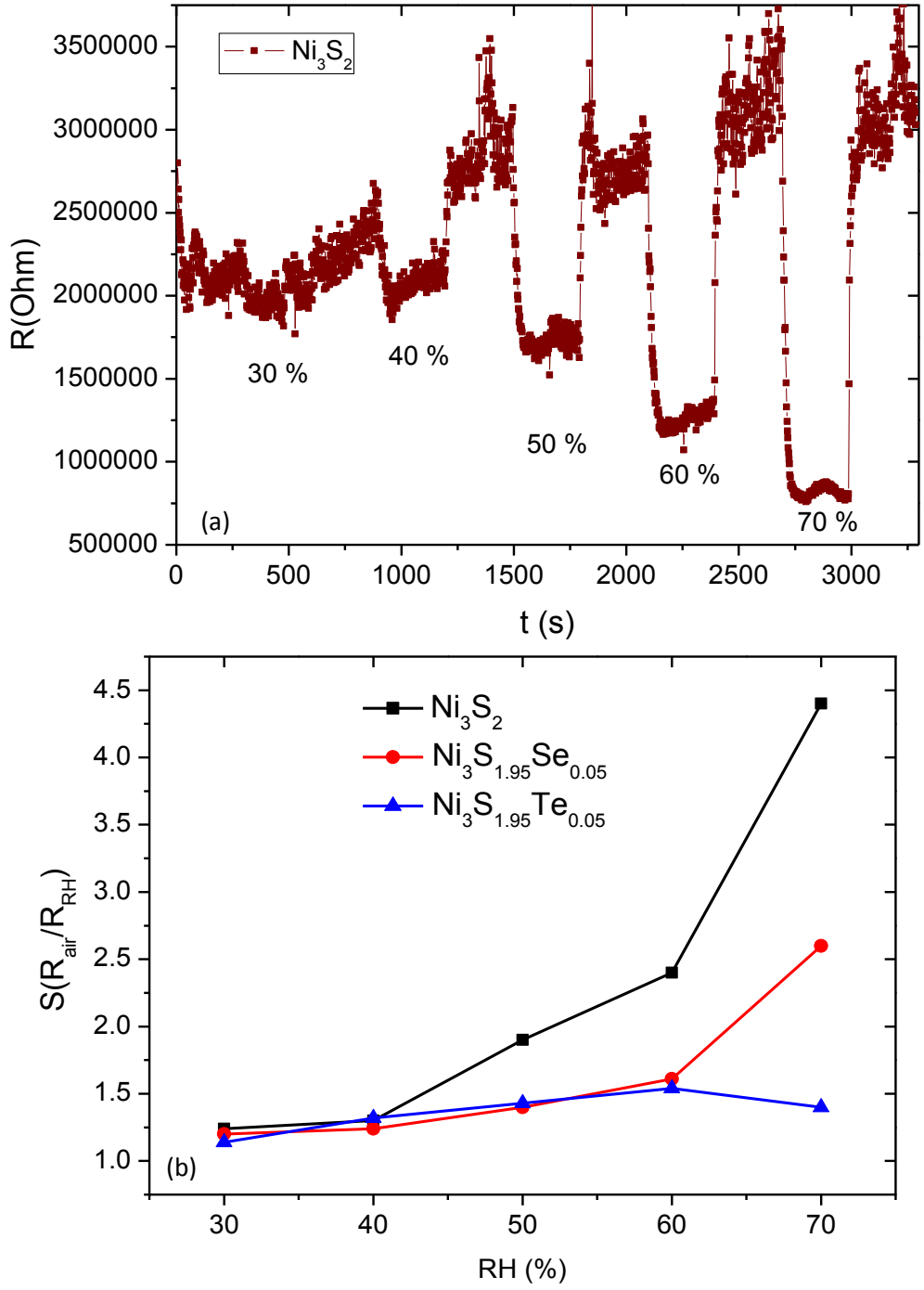


Figure 7.6: (a) RH sensing of the Ni_3S_2-based sensor device and (b) the sensitivity versus RH % plot for the pure, Se doped and Te dopes Ni_3S_2 based sensor devices.

7.4 Conclusions

In summary, rhombohedral Ni_3S_2 phase with layer-based flower-like structures were obtained via a simple, low cost microwave-assisted hydrothermal technique. The sample composition was confirmed by XRD and microscopy analysis. The Ni_3S_2 material was doped with small amounts of Se and Te and the doped elements were confirmed by EDS analysis. A uniform distribution of the dopants within the Ni_3S_2 material was observed using the EDS image mapping technique. The Se doped samples showed new emission properties while Te doped sample showed the enhancement of the Pl properties of Ni_3S_2 sample. The prepared samples showed sensitivity which increased with increased RH percentages.

7.5 Future plans

More RH sensing studies in doped Ni_3S_2 samples are planned in order to see the effect of doping on the RH sensing performance.

7.6 References

[1] Lai, C.H., Huang, K.W., Cheng, J.H., Lee, C.Y., Lee, W.F., Huang, C.T., Hwang, B.J., Chen, L.J., *J. Mater. Chem.* **19** (2009) 7277.

[2] Chi, W.S., Han, J.W., Yang, S., Roh, D.K., Lee, H., Kim, J.H., *Chem. Commun.* **48** (2012) 9501.

[3] Lai, C.H., Lu, M.Y., Chen, L.J., *J. Mater. Chem.* **22** (2012) 19.

[4] Park, S., An, S., Ko, H., Lee, S., Lee, C., *Sensors and Actuators B:* **188** (2013) 1270.

[5] Song, L., Zhang, S., Chen, C., Hu, X., Wei, Q., *Chem. Eng. J.* **171** (2011) 1454.

[6] Nenavathu, B.P., Rao, A.V.R.K., Goyal, A., Kapoor, A., Dutta, R.K., *Appl. Catal. A* **459** (2013) 106.

[7] Jamali-Sheini, F., Yousefi, R., Mahmoudian, M.R., Bakr, N.A., Sa'aedi, A., Huang, N.M., *Ceramics Int.* (2014).

[8] Sun, L., Liu, C., Liao, C., Yan, C., *J. Mater. Chem.* **9** (1999) 1655.

[9] Mhamdi, A., Boukhachem, A., Madani, M., Lachheb, H., Boubaker, K., Amlouk, A., Amlouk, M., *Optik* **124** (2013) 3764.

[10] Simerjeet K.G., Presrton B., Louisa J. H.W., *J Sol-Gel Sci. Technol.* **57** (2011) 68.

[11] Tsai, F.S., Wang, S.J., *Sensors and Actuators B* **193** (2014) 280.

[12] Yadav, B.C., Srivastava, R., Dwivedi, C.D., Pramanik, P., *Sensors and Actuators A* **153** (2009) 137.

[13] Biswas, P., Kundu, S., Banerji, P., Bhunia, S., *Sensors and Actuators B* **178** (2013) 331.

Chapter 8: Conclusions and recommendations

8.0 Preamble

This chapter contains some concluding remarks in view of the work covered in the thesis. Recommendations for future studies are also made.

8.1 General conclusion

NiS_x materials have been obtained via simple chemical routes in the past, however, the application of a microwave thermal technique to fabricate these materials have been seldom used. Further, the application of these materials in new technologies is only emerging. This study explored the microwave synthesis to make some NiS_x materials and investigate their novel applications in sensing. GaN material synthesis by a novel microwave synthesis was also explored as well as its application in sensing.

NiS_2 hierachical structures were obtained from a reaction of $NiCl_2.6H_2O$ and S powder in ethanol solution. The NiS_2 material was obtained when 800 W and 220 ^oC were employed for 60 minutes. The synthesized materials had uniformly distributed morphologies with the average particle size of around 400 nm. The PL analysis of the materials showed a UV and a NIR emission which were attributed to intra-band transitions. A similar observation was observed from HDA capped nanostructures which were also obtained from a similar method, with 600 W microwave power was used and HDA capping agent added to the reactants.

Hexagonal NiS was obtained from a reaction of $Na_2S.9H_2O$ with $NiCl_2.6H_2O$/NiAc in water, by microwave heating at 600 W for 15 minutes. Uniformly distributed nanolayer-based structures were obtained. Annealed α-NiS material was used to prepare a PVA based pressure sensor and ethanol gas sensing device and the material was observed to be sensitive to both applied hydrostatic pressure and ethanol gas. Further, annealing studies were performed on this material from 150 ^oC to 600 ^oC in N_2

atmosphere and it was observed that NiS started to transform to NiO above a 300 ^{o}C annealing temperature. This was accompanied by the increasing crystallinity of NiS up to 300 ^{o}C before the material started to be oxidized. The paramagnetic properties of the annealed samples did not vary much between NiS and NiO phases. The FTIR properties of the samples were observed to change after annealing the samples at 450 ^{o}C and above. The IR transmission of the annealed samples increased due to the presence of NiO. Thermal analysis of the annealed samples showed a reduction in the amount of adsorbed hydroxyl groups as the temperature was increased, in agreement with XRD analysis. The MIT of this material was confirmed by resistance measurements that were recorded while the sample was heating up from liquid N_2 to room temperature. The transition observed was around 260 K, in agreement with literature reported data.

The synthesis of a binary phase (α- and β-) NiS was studied when a NaOH solution was used as a solvent; this is unlike the single α-NiS phase formed when H_2O was used. The formation of the binary phase NiS was promoted by the solubility of the precursors in the solvent, different solubility constants of the α-NiS and β-NiS products, as well as the reaction rate and time. Hexagonal platelets and rod-like nanostructures were obtained which correspond to α-NiS and β-NiS respectively. Nanorod-based flower-like structures were obtained at high NaOH concentration and increased reaction time, which formed from the clustering of rods and particles. Further, a growth mechanism was proposed due to observations made on the morphologies of the previous reactions, using SEM and TEM imaging analysis

UV-blue emitting GaN nanocrystals were synthesized from $GaCl_3$ and Li_3N in benzyl ether, by microwave heating the reactants at 600 W for 10 minutes. XRD analysis of the particles confirmed the hexagonal wurtzite phase of GaN. The hydrostatic pressure sensing ability of GaN/PVA composite based devices was measured for devices fabricated from different concentrations of GaN nanoparticles. A very high sensitivity response of up to 48 times was achieved for 2 mg/ml GaN concentration in 5 ml PVA at 180 kPa applied hydrostatic pressure. VOCs from tomato were also detected by GaN/PVA based device and a high sensitivity was achieved with

relatively low response and recovery times. Elimination of oxygen from the GaN synthesis reaction by microwave proved to be a challenge which generated Ga_2O_3 impurity in the product.

Rhombohedral Ni_3S_2 nano-layer based flower-like structures were also obtained by microwave assisted hydrothermal synthesis using thiourea and $NiCl_2.6H_2O$ precursors in distilled water. The material was further doped with 2.5% Se and Te using a NaO_3Se_2 and TeO_2 as dopant sources. The uniform distribution of the doped elements on Ni_3S_2 was confirmed by EDS electron image mapping, suggesting a uniform nucleation of the dopants with the Ni_3S_2. Further, all the samples showed sensitivity which increased with increased RH percentages.

8.2 Future work and recommendations

The β-NiS phase synthesized was observed to have rod morphologies which could be interesting for possible electronic application studies. The application of NiS_x materials in emerging technologies is still new and needs to be pursued as these materials can easily be obtained and show interesting properties for visible range optical applications. A thorough study of the metal doping on the properties of NiS_x materials is needed in order to evaluate whether the NiS_x material properties could be improved. We were the first group to evaluate these materials for sensing applications and studies on sensor device fabrication for these materials should be further pursued.